CANADIAN THESES

THÈSES CANADIENNES

NOTICE

AVIS

THIS DISSERTATION HAS BEEN MICROFILMED EXACTLY AS RECEIVED

LA THÈSE A ÉTÉ MICROFILMÉE TELLE QUE NOUS L'AVONS REÇUE

Canadä

THE UNIVERSITY OF ALBERTA

SEISMIC DIFFRACTION FROM WEDGES

by

Ⓒ GEE HUNG CHAN

A THESIS

SUBMITTED TO THE FACULTY OF GRADUATE STUDIES AND RESEARCH

IN PARTIAL FULFILMENT OF THE REQUIREMENTS FOR THE DEGREE

OF DOCTOR OF PHILOSOPHY

IN

GEOPHYSICS

DEPARTMENT OF PHYSICS

EDMONTON, ALBERTA

SPRING 1987

THE UNIVERSITY OF ALBERTA

RELEASE FORM

NAME OF AUTHOR   GEE HUNG CHAN

TITLE OF THESIS   SEISMIC DIFFRACTION FROM WEDGES

DEGREE FOR WHICH THESIS WAS PRESENTED   DOCTOR OF PHILOSOPHY

YEAR THIS DEGREE GRANTED   SPRING 1987

Permission is hereby granted to THE UNIVERSITY OF ALBERTA LIBRARY to reproduce single copies of this thesis and to lend or sell such copies for private, scholarly or scientific research purposes only.

The author reserves other publication rights, and neither the thesis nor extensive extracts from it may be printed or otherwise reproduced without the author's written permission.

(SIGNED) .... *Gee Hung Chan* ....

PERMANENT ADDRESS:

.... *4087 Orion Place* .....

.... *Victoria, B.C.* ....

.... *V8N 5K9* ....

DATED .... *6 November* .. 1986

THE UNIVERSITY OF ALBERTA

FACULTY OF GRADUATE STUDIES AND RESEARCH

The undersigned certify that they have read, and
recommend to the Faculty of Graduate Studies and Research,
for acceptance, a thesis entitled SEISMIC DIFFRACTION FROM
WEDGES submitted by Gee-Hong CHAN in partial fulfilment of
the requirements for the degree of Doctor of Philosophy in
Geophysics.

....
Supervisor

....

....

....

Date   October 17, 1986

ABSTRACT

The asymptotic ray theory, or the ray method has been used widely in seismic modelling and interpretation of real seismic records. However, it cannot be used for the investigation of diffracted waves, which appear frequently in a laterally inhomogeneous medium.

The first part of this thesis formulates a general theory to obtain the diffracted response near a shadow boundary. The method uses an integral-transform on the wave equation. A solution is obtained in the form of an infinite sum, after solving a recursive equation by the method of iteration. The elements in the sum are analogous to successive reflection/transmission of ray bundles.

Re-organization of the contour of integration in the transform allows one to separate the geometric and diffracted contributions to the total wave field. Finally, the diffracted field is written to be proportional to the geometric amplitude along the shadow boundary. The coefficient of proportionality is simplified to an analytic form using a high frequency approximation.

Numerical results of a tar sand model are presented. The synthetic seismograms are compared with results obtained by Mikhailenko using an analytic-numerical method.

ACKNOWLEDGEMENTS

TABLE OF CONTENTS

LIST OF ILLUSTRATIONS

CHAPTER 1

INTRODUCTION

Derived in line with geometrical optics (Kline, 1951), the asymptotic ray theory (Babich and Alekseev, 1958; Karal and Keller, 1959; Cerveny, 1972; Hron and Kanasewich, 1971) has been used in the study of wave propagation in inhomogeneous media. Its application in both modelling and interpretation for seismic prospecting has been successful.

However, ART (asymptotic ray theory) is based on energy propagation along non-leaky ray tubes. The result is that it breaks down in the presence of a shadow boundary which forms a discontinuity along the wavefront. To satisfy the physical nature of the continuity of a total wavefront, numerous attempts were made to remedy this situation by the introduction of diffracted waves originated at the edge-like discontinuities of the media. Physically, it is similar to energy diffusion (Fock, 1965; Born & Wolf, 1968) in electromagnetics and optics. Such development in the elastic wave study were by Claerbout, 1976; Trorey, 1977; Hilterman, 1982; Fertig and Muller, 1979. In particular, the case of wave propagation in a wedge-shaped medium has been widely investigated (Hudson, 1963; Bowman and Senior, 1969; Alford, Kelly and Boore, 1974; Zemell, 1975; Pao and Ziegler, 1982;

Sanchez-Sesma, 1985). While a lot of these works concentrated on SH-waves only, consideration on P-SV case has been given by Knopoff(1969), Forristal and Ingram (1971), and Zeigler and Pao (1984).

The present work also tries to seek a solution for the problem of wave diffraction in a wedge-shaped medium. As the theory eventually blends in with the ray method, the diffracted contribution, being proportional to the geometric ray along the shadow boundary, will be established to rectify one of the shortcomings of ART.

CHAPTER 2

EDGE WAVE THEORY IN ACOUSTIC CASE

The simpler case of acoustic plane wave diffraction by a wedge-shaped obstacle is first discussed as a preparation for the more general elastic case.

Let the 2-dimensional space $(r \geq 0, -\pi \leq \theta \leq \pi)$ be divided into two angular regions (Fig. 1a) which are defined by $\theta_1^+ \leq \theta \leq \theta_1^-$, and $\{ \theta_2^+ \leq \theta \leq \pi \} \cup \{ -\pi \leq \theta \leq \theta_2^- \}$, with θ_1^+ and θ_2^- denoting the same boundary, likewise for θ_1^- and θ_2^+. The properties of the medium for each region m (m=1,2) are characterized by the velocity c_m of acoustic wave propagation and its density ρ_m. The goal of the following investigation is to study the behaviour of the resultant wave field upon the interaction between an incident wave with the wedge.

The incident wave is considered to be plane, homogeneous and with wave number κ_k, propagating in the k-th region at an incident angle of $\theta = \theta_k$ (see Fig. 1b). Being assigned to have unit amplitude, it may be represented by

(2.1) $\qquad F_k^o = e^{i \kappa_k r \cos(\theta_k)}$

Figure 1   (a) Model of media.

(b) Incident wave and definition of θ_k.
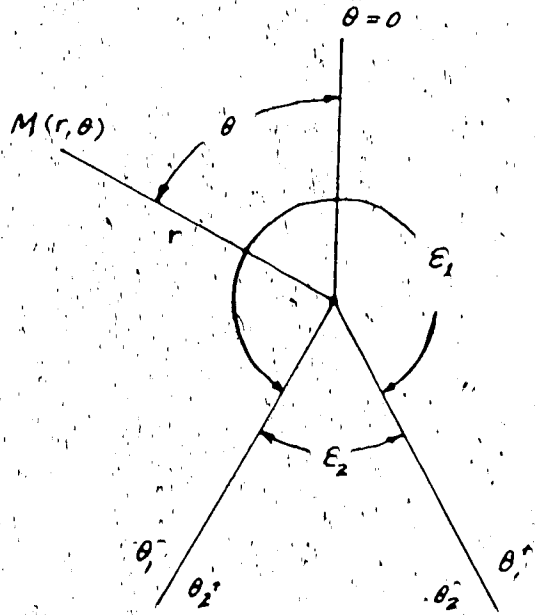
a
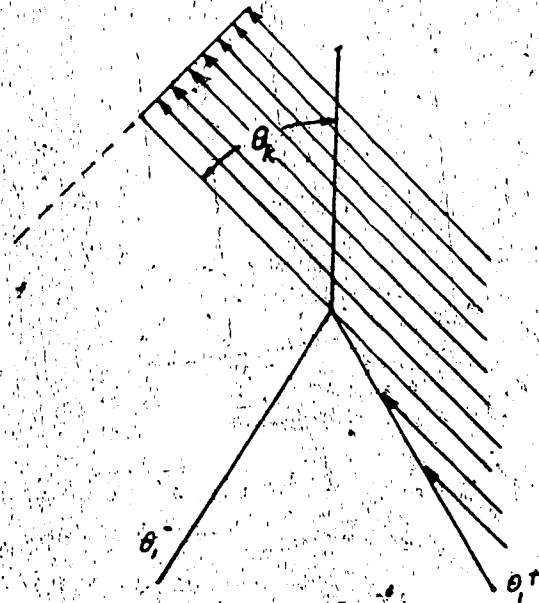
b

with $i^2 = -1$.

Because of the presence of the boundaries, ending at the top of the wedge, the following expression is used to define the illuminated and shadow regions for the incident field.

$$(2.2) \qquad F_k^o = \begin{cases} e^{i\kappa_k r \cos(\theta-\theta_k)} & s_k(\theta-\theta_k) < 0 \\ 0 & s_k(\theta-\theta_k) > 0 \end{cases}$$

where $s_k = \text{sgn}(\theta_k)$.

Without loss of generality, the incident wave is assumed to be propagating initially in region 1, i.e. $k = 1$. Let equation (2.2) describe the acoustic pressure field. The resulting total wave field in the m-th region is denoted by F_m with frequency ω, satisfying the Helmholtz equation

$$(2.3) \qquad (\nabla^2 + k_m^2) F_m = 0,$$

where $\kappa_m = \omega/c_m$.

The boundary conditions are set as the continuities of the pressure field and the normal component of the velocity. This leads to

(2.4a) $(F_1)_{\theta=\theta_1^{\pm}} = (F_2)_{\theta=\theta_2^{\mp}}$,

and

(2.4b) $\frac{1}{\rho_1}[\frac{\partial}{\partial n}F_1]_{\theta=\theta_1^{\pm}} = \frac{1}{\rho_2}[\frac{\partial}{\partial n}F_2]_{\theta=\theta_2^{\mp}}$,

where $\frac{\partial}{\partial n}$ denotes the normal derivative with respective to the boundary.

Now, in the m = 1 region, one can write

(2.5) $F_1 = F_1^o + \bar{F}_1$,

where $\bar{F}_1$ is the additional pressure field generated by the interaction of the incident wave F_1^o with the boundaries. Note that because of i) the discontinuity of F_1^o (Fig. 1b), with respect to the shadow boundary at $\theta = \theta_1$, and ii) the assumed (and physically realizable) continuity of the solution to the Helmholtz equation for the total wave field F_1, then $\bar{F}_1$, the secondary field must also have a discontinuity at $\theta = \theta_1$.

The solution for the total wave field F_m (m = 1,2) will be sought with the aid of an integral transform on the F_m's which appear in a system of two differential equations (2.3)

subject to four boundary conditions pertaining to equations (2.4a) and (2.4b).

2.1 Sommerfeld Integral Transform

We will examine the following pair of integral representations, which according to Sommerfeld (1896) and Malyuzhinetz (1958) can be written as

$$(2.6a) \qquad F(r) = \frac{1}{2\pi i} \int_{\Gamma_0} S(\alpha)\, e^{-i\kappa r \cos\alpha}\, d\alpha,$$

with the path of integration Γ_0 (Fig. 2) and

$$(2.6b) \qquad S(\alpha) = \frac{i\kappa \sin\alpha}{2} \int_0^\infty F(r)\, e^{i\kappa r \cos\alpha}\, dr.$$

The function $F(r)$ here may be considered as a cylindrical wavefront, consisting of plane wave components, propagating in arbitrary emergence angle α, and being governed by the weighting function $S(\alpha)$. Appendix A shows that (2.6a) and (2.6b) are indeed proper transform pair under certain prescribed constraints on F and S.

The representation of F in (2.6a) is useful in that it satisfies the homogeneous Helmholtz equation, in polar

Figure 2   Contours of Γ, Γ_0, Γ_1, Γ_2 and Γ_3.
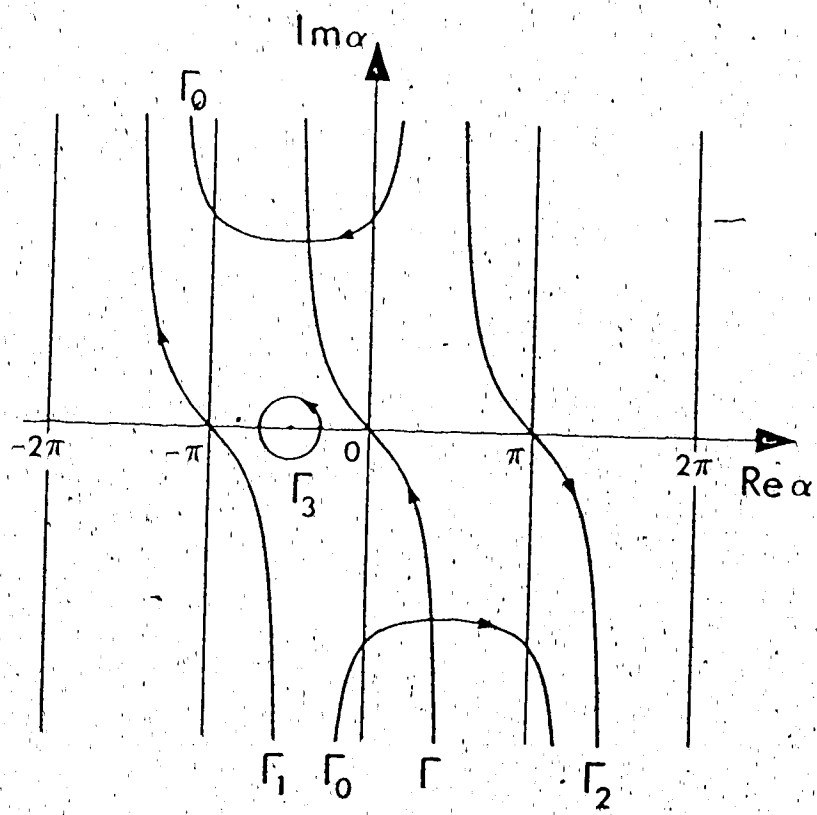
coordinates, with wave number κ. Two important properties arise from (2.6a) and they are

(2.7) $\int_{\Gamma_o} S(\alpha) \, e^{-i\kappa r \cos(\alpha-\theta)} \, d\alpha$

$\equiv \int_{\Gamma_o} S(\alpha + \theta) \, \exp^{-i\kappa r \cos\alpha} \, d\alpha,$

and

(2.8) $\int_{\Gamma_o} S_b(\alpha + \theta) \, e^{-i\kappa_a r \cos\alpha} \, d\alpha$

$\equiv \int_{\Gamma_o} \tau_{ab}(\alpha) \, S_b[\, \phi_{ab} + \theta \,] \, e^{-i\kappa_b r \cos\alpha} \, d\alpha,$

where

(2.8a) $\phi_{ab} = \cos^{-1} [\, (c_a/c_b) \cos\alpha \,]$

(2.8b) $\tau_{ab} = \dfrac{d}{d\alpha} \, \phi_{ab}(\alpha).$

Equation (2.8) gives the freedom in choosing a specific wave number, (i.e. κ_b here) for the transformation kernel. The tie is established through the use of ϕ and τ in (2.8a) and (2.8b), with the former merely the Snell's law relating the angles of emergence ϕ and α at the sectorial boundary, while the latter, a manifestation of the divergence weighing factor.

2.2   Separation of the Wave Field

With substitution by the transforms, the total wave field $F_m(r,\theta)$ (in regions $m=1,2$) may be represented by the following expression

$$(2.9) \qquad F_m(r,\theta) = \frac{1}{2\pi i} \int_{\Gamma_0} S_m \, e^{-i\kappa_m r \cos(\alpha-\theta)} \, d\alpha$$

Recall that in equation (2.5), F_1 is the sum of the incident field F_1^0 and the secondary field $\bar{F}_1$, which is a composition of reflection and/or diffraction responses upon the interaction between F_1^0 and the wedge boundaries. We next proceed to split the functions S_1 into the above mentioned components. This can be accomplished by defining

$$(2.10) \qquad S_1(\alpha) = D_1(\alpha) + \bar{S}_1(\alpha)$$

with

$$(2.10a) \qquad D_1(\alpha) = [\alpha - \theta_1 + s_1\pi]^{-1}.$$

Then

$$(2.11) \qquad F_1 = F_1^0 + \bar{F}_1$$

$$= \frac{1}{2\pi i} \int_{\Gamma_0} D_1(\alpha+\theta) \; e^{-i\kappa_1 r \cos\alpha} \, d\alpha \; +$$

$$+ \frac{1}{2\pi i} \int_{\Gamma_0} S_1(\alpha+\theta) \; e^{-i\kappa_1 r \cos\alpha} \, d\alpha$$

In the first term on the right hand side of (2.11),
$D_1(\alpha+\theta)$ has a simple pole at $\alpha = -\theta + \theta_1 - s_1\pi$. Hence we now
deform Γ_0 in Fig. 2 such that it takes on the sum of Γ_1, Γ_2,
Γ_3, and the connecting segments along the real α axis
between Γ_3 and Γ_1 (or Γ_2). If

(2.12a) $\qquad -\pi < -\theta + \theta_1 - s_1\pi < \pi$

then the pole is inside the contour, and the corresponding
residue provides the field of the incident field (2.2) in
the illuminated region. If

$$-\theta + \theta_1 - s_1\pi < -\pi, \; or.$$

(2.12b)

$$-\theta + \theta_1 - s_1\pi > \pi,$$

implying that

$$s_1 (\theta - \theta_1) > 0: \text{ then the integral for } F_1^0 \text{ results}$$
in zero, agreeing with the corresponding to the pole α being

outside the interval $(-\pi, \pi)$, thereby not being encountered
during the deformation of the original contour of
integration. This clearly corresponds to points $P(r,\theta)$ in
the shadow zone of the first sector.

In view of the fact that the incident field may
interact with either or both of the boundaries as defined by
$\theta = \theta_1^+ = \theta_2^-$ and $\theta = \theta_1^- = \theta_2^+$, two new functions $F_1^{o\pm}(\theta)$ are
introduced to reflect the proper choice of reference
direction with respect to the individual boundaries. They
are

$$(2.13) \qquad F_1^{o\pm}(r,\theta) = \frac{1}{2\pi i} \int_{\Gamma_o} D_1^{\pm}(\alpha)\, e^{-i\kappa_1 r \cos(\alpha - \gamma_1^{\pm})}\, d\alpha$$

where

$$(2.14a) \qquad D_1^{\pm}(\alpha) = (\alpha + a_1^{\pm})^{-1}$$

$$(2.14b) \qquad a_1^{\pm} = \pm(\theta_1^{\pm} - \theta_1 + s_1\pi)$$

$$(2.14c) \qquad \gamma_1^{\pm} = \pm(\theta - \theta_1^{\pm})$$

A short exercise in changing of variables will show
that

$$(2.15) \qquad F_1^o = F_1^{o+} = F_1^{o-}$$

$$= \frac{1}{2} \left(F_1^{o^+} + F_1^{o^-} \right)$$

Hence, equation (2.15) may be interpreted as F_1^o being decomposed into two separate groups of waves, each homing in on the corresponding boundaries. Note that there is a slight resemblence to the treatment of wave propagation in parallel layers in which the waves are separated into up- and down-going categories, with each of them approaching different boundaries of the layer (either top or bottom). In this case when there may be two boundaries 'illuminated' by the incident wave, we can express the total wave field F_1 as either

$$(2.16) \qquad F_1 = F_1^{o^+} + \bar{F}_1,$$

or

$$F_1 = F_1^{o^-} + \bar{F}_1,$$

where $\bar{F}_1$ is the wave field generated by the interaction between the incident field $F_1^{o^\pm}$, related to the appropriate illuminated boundary $\theta_1^\pm$ and the wedge.

2.3 Reformulation of the System of Equations

As far as the functions $D_1^\pm$ are regular as $| \text{Im } \alpha | \to \infty$,

the integrals in $F_1^{o\pm}$ will satisfy the Helmholtz equations, as the order of operation of integration and differentiation can be interchanged.

$$(2.17) \qquad (\nabla^2 + \kappa_1^{\,2}) \; F_1^{o\pm} = 0.$$

Therefore, using the simple rule of superposition of solutions, the unknown function $\bar{F}_1$, must also satisfy the Helmholtz equation as the total field F_1 in (2.16) is assumed to be a solution to the wave equation.

With the absence of the incident field in $m = 2$ region, its total field is simply represented by

$$(2.18) \qquad F_2 = \bar{F}_2$$

Combining (2.11) and (2.18), one can write

$$(2.19) \qquad F_m = \delta_{1m} F_1^{o\pm} + \bar{F}_m, \qquad m = 1,2$$

where δ_{1m} is the Kronecker delta function ($\delta_{11} = 1$, $\delta_{12} = 0$), and the unknown functions $\bar{F}_m$ are the solutions of the Helmholtz equations

$$(2.20) \qquad (\nabla^2 + \kappa_m^{\,2}) \; \bar{F}_m = 0, \qquad m = 1,2$$

Substituting (2.19) into the boundary conditions (2.4) gives

$$(\bar{F}_1 + \bar{F}_1^{\circ \mp})_{\theta = \theta_1^{\pm}} = (\bar{F}_2)_{\theta = \theta_2^{\mp}},$$

(2.21)

$$\frac{1}{\rho_1}[\ \frac{\partial}{\partial n}(\bar{F}_1 + \bar{F}_1^{\circ \mp})]_{\theta = \theta_1^{\pm}} = \frac{1}{\rho_2}\ [\frac{\partial}{\partial n}\bar{F}_2]_{\theta = \theta_2^{\mp}}.$$

2.4   The Secondary Wave

Since the $\bar{F}_m$'s satisfy the Helmholtz equation, they may be written in the form of the Sommerfeld-Malyuzhinetz integral

(2.22) $\bar{F}_m(r,\theta) = \frac{1}{2\pi i} \int_{\Gamma_o} \bar{S}_m(\alpha)\ e^{-i\kappa_m r\ \cos(\alpha - \theta)}\ d\alpha$

To find the $\bar{F}_m$'s, it follows to substitute expressions (2.22) and the incident field representations (2.13) into the boundary conditions (2.21). The expression of the exponents in the Sommerfeld-Malyuzhinetz integrals are reduced to the same form using the same independent variable α, representing rays in the direction of the individual elementary waves in the incident wave field. This is done with the aid of the properties of the transform (2.7) and

(2.8). The following algebraic manipulation will establish a system of functional equations with respect to the sought $\bar{S}_m$'s, which in turn, will be expressed eventually as solutions obtained with the help of an iterative scheme.

Note that the boundary conditions stipulate the evaluation of terms of the different sides of the same boundary which itself has two different formal designations; (e.g. left hand side of eqn. (2.21) at $\theta = \theta_1^-$ pairs up with $\theta = \theta_2^+$ on the right hand side). This inconvenience may be avoided if we decompose the secondary fields in the form of

$$(2.23) \qquad \bar{F}_m = F_m^+ + F_m^-$$

to account for the separate influence of each boundary where the secondary wave originates. Also, using the similar change of variables as applied on the incident field $F_1^{o\pm}$ in (2.13), one can write

$$(2.24) \qquad \bar{F}_m = \frac{1}{2\pi i} \int_{\Gamma_0} \bar{S}_m^\pm(\alpha) \, e^{-i\kappa_m r \cos(\alpha - \gamma_m^\pm)} \, d\alpha$$

where $\gamma_m^\pm = \pm(\theta - \theta_m^\pm)$. This change in variable leads to

$$(2.25) \qquad \bar{F}_m = \pm \frac{1}{2\pi i} \int_{\Gamma_0} \bar{S}_m^\pm(\pm\alpha \mp \theta_m^\pm) \, e^{-i\kappa_m r \cos(\alpha - \theta)} \, d\alpha.$$

Substituting (2.25) into (2.23) and comparing with

equation (2.22) yields

$$(2.26) \qquad \bar{S}_m(\alpha) = \bar{S}_m^+(\alpha + \theta_m^+) - \bar{S}_m^-(-\alpha + \theta_m^-)$$

In this way, the original problem of determining (2.23) leads to the solving of the $\bar{S}_m^\pm$'s, $m = 1,2$. The computation of normal derivative in two of the boundary conditions necessitates a separation of r into a more manageable form presented next.

In a more general case, N sectorial regions $\theta_\nu^+ \leq \theta \leq \theta_\nu^-$, $\nu = 1, 2, 3, \ldots, N$, constitute an inhomogeneous medium with N boundaries. We will introduce for each individual boundary a Cartesian system of coordinates (Fig. 3), in which the coordinate lines in the ν-th region is given by

$$(2.27) \qquad x_\nu = r \cos\gamma_\nu^+ \qquad y_\nu = r \sin\gamma_\nu^+$$

where the same system express a coordinate line in the $(\nu-1)$-th region by

$$x_{\nu-1} = \cos\gamma_{\nu-1}^- \qquad y_{\nu-1} = -r \sin\gamma_{\nu-1}^-.$$

Here the x-axis is along the boundary between the ν-th and the $(\nu-1)$-th sectors, and the y-axis is normal to it,

positively oriented into the ν-th region. We can now write equations (2.13).

(2.28a) $F_1^{o\pm} = \frac{1}{2\pi i} \int_{\Gamma_0} D_1^{\pm}(\alpha)\, e^{i\kappa_1 \eta_1^{\pm}}\, d\alpha$, and

(2.28b) $\bar{F}_\nu^{\pm} = \frac{1}{2\pi i} \int_{\Gamma_0} S_\nu^{\pm}(\alpha)\, e^{i\kappa_\nu \eta_\nu^{\pm}}\, d\alpha$,

where $\eta_\nu^+ = x \cos\alpha + y \sin\alpha$

$\eta_\nu^- = x \cos(\alpha - \epsilon_\nu) - y \sin(\alpha - \epsilon_\nu)$

$\eta_{\nu-1}^+ = x \cos(\alpha - \epsilon_{\nu-1}) + y \sin(\alpha - \epsilon_{\nu-1})$

$\eta_{\nu-1}^- = x \cos\alpha - y \sin\alpha$

with

(2.29) $\epsilon_\nu = \begin{cases} \theta_\nu^- - \theta_\nu^+ \\ \theta_\nu^- - \theta_\nu^+ + 2\pi \end{cases}$ for $\begin{matrix} \theta_\nu^- > \theta_\nu^+ \\ \theta_\nu^- < \theta_\nu^+ \end{matrix}$

and the η's and ϵ''s are as shown in Fig. 3.

Then the boundary conditions (2.21) can be written in a more usual form, that is, the waves which move towards and away from the same boundary are gathered according to the medium in which they propagate:

Figure 3   Transformation between γ's and η's,

in equations 2.27 to 2.29.
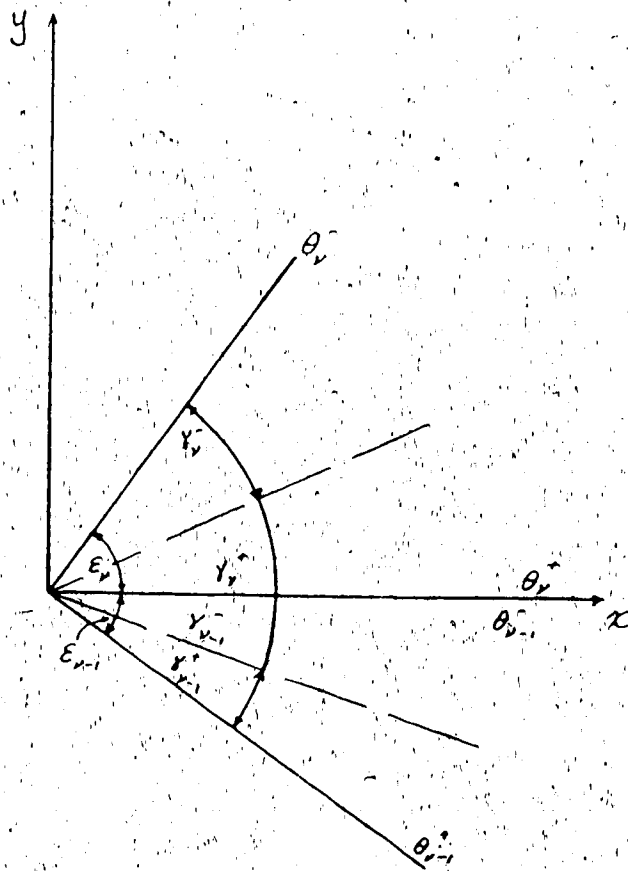
$$(2.30) \quad [a_{q\nu} (F_\nu^+ + F_\nu^- + \delta_{\nu k} F_{\nu 0}^-)]_{\theta = \theta_\nu^+}$$

$$- [a_{q(\nu-1)} (F_{\nu-1}^+ + F_{\nu-1}^- + \delta_{1k} F_{(\nu-1)0}^-)]_{\theta = \theta_{(\nu-1)}^-} = 0$$

where $a_{1\nu} = 1$

$$a_{2\nu} = \frac{1}{\rho_\nu} \frac{\partial}{\partial y}$$

$$q = 1, 2$$

$$\nu = 1, 2$$

$k =$ index of sector in which the incident incident wave exists (in our case, $k = 1$).

Substituting (2.28a) & (2.28b) into (2.30) yields for $q = 1$

$$(2.31a) \quad \int_{\Gamma_0} [S_\nu^+(\alpha) + S_\nu^-(\alpha + \epsilon_\nu) + \delta_{\nu k} D_\nu^-(\alpha + \epsilon_\nu)] \cdot e^{-i\kappa_\nu x \cos\alpha} \, d\alpha$$

$$+ \int_{\Gamma_0} [S_{\nu-1}^+(\alpha + \epsilon_{\nu-1}) + S_{\nu-1}^-(\alpha) + \delta_{(\nu-1)k} D_{\nu-1}^+(\alpha + \epsilon_{\nu-1})] \cdot$$

$$e^{-i\kappa_{\nu-1} x \cos\alpha} \, d\alpha = 0,$$

and for $q = 2$

-(2.31b) $\int_{\Gamma_O} \frac{\sin\alpha}{\omega_\nu} [\ \bar{S}_\nu^+(\alpha) - \bar{S}_\nu^-(\alpha + \epsilon_\nu) - \delta_{\nu k} D_\nu^-(\alpha + \epsilon_\nu)].$

$e^{-i\kappa_\nu x \cos\alpha} d\alpha +$

$+ \int_{\Gamma_O} \frac{\sin\alpha}{\omega_{\nu-1}} [\ \bar{S}_{\nu-1}^+(\alpha + \epsilon_{\nu-1}) - \bar{S}_{\nu-1}^-(\alpha) +$

$+ \delta_{(\nu-1)k} D_{\nu-1}^+(\alpha + \epsilon_{\nu-1})].$

$e^{-i\kappa_{\nu-1} x \cos\alpha} d\alpha = 0$

with $\qquad \omega_\nu = \rho_\nu c_\nu.$

We substitute in the second terms of (2.31 a,b) the variable α by $\psi_{(\nu-1)\nu}(\alpha)$. This relates the direction α of the elementary plane waves in medium ν with the corresponding $\psi_{(\nu-1)\nu}(\alpha)$ angle in the sector $\nu-1$ via Snell's law (2.8). Hence we can write

(2.32) $\qquad \int_{\Gamma_O} A_q(\alpha) e^{-i\kappa_\nu x \cos\alpha} d\alpha = 0$ for $q = 1,2$

where $\qquad A_1(\alpha) = \bar{S}_\nu^+(\alpha) + \bar{S}_\nu^-(\alpha + \epsilon_\nu) + \delta_{\nu k} D_\nu^-(\alpha + \epsilon_\nu) -$

$- \tau_{(\nu-1)\nu}(\alpha) \{\ \bar{S}_{\nu-1}^+ [\psi_{(\nu-1)\nu}(\alpha) + \epsilon_{\nu-1}\ ] +$

$+ \bar{S}_{\nu-1}^- [\ \psi_{(\nu-1)\nu}(\alpha)\ ] +$

$+ \delta_{(\nu-1)k} D_{\nu-1}^+ [\ \psi_{(\nu-1)\nu}(\alpha) + \epsilon_{\nu-1}\ ]\},$

$$A_2(\alpha) = \frac{\sin\alpha}{\omega_\nu} [\bar{S}_\nu^+(\alpha) - \bar{S}_\nu^-(\alpha + \epsilon_\nu) - \delta_{\nu k} D_\nu^-(\alpha + \bar{\epsilon}_\nu)] -$$

$$- \tau_{(\nu-1)\nu}(\alpha) \cdot \{ \sin\psi_{(\nu-1)\nu}(\alpha)/\omega_{\nu-1} \} \cdot$$

$$\cdot \{ \bar{S}_{\nu-1}^+ [\psi_{(\nu-1)\nu}(\alpha) + \epsilon_{\nu-1}] + \bar{S}_{\nu-1}^- [\psi_{(\nu-1)\nu}(\alpha)] +$$

$$+ \delta_{(\nu-1)k} D_{\nu-1}^+ [\psi_{(\nu-1)\nu}(\alpha) + \epsilon_{\nu-1}] \}.$$

The sufficient but not necessary conditions to satisfy identities (2.32) are

$$(2.33a) \qquad A_1(\alpha) \equiv 0 \text{ ,and}$$

$$(2.33b) \qquad A_2(\alpha) \equiv 0,$$

respectively.

Eliminating from (2.33) the functions $\bar{S}_{\nu-1}^- [\psi_{(\nu-1)\nu}(\alpha)]$ and solving for $\bar{S}_\nu^+(\alpha)$ yields

$$(2.34) \qquad \bar{S}_\nu^+(\alpha) = K_{\nu,\nu} [\bar{S}_\nu^-(\alpha + \epsilon_\nu) + \delta_{\nu k} D_\nu^-(\alpha + \epsilon_\nu)] +$$

$$\tau_{(\nu-1)\nu}(\alpha) \cdot K_{(\nu-1)\nu}(\alpha) \cdot$$

$$\cdot \{ \bar{S}_{\nu-1}^+ [\psi_{(\nu-1)\nu}(\alpha) + \epsilon_{\nu-1}] +$$

$$\delta_{(\nu-1)k}\, D^+_{\nu-1}\, [\; \psi_{(\nu-1)\nu}(\alpha) + e_{\nu-1}\;]\; \},$$

where
$$K_{\nu\nu} = \{\; \frac{w_{\nu-1}}{\sin\psi_{(\nu-1)\nu}(\alpha)} - \frac{w_\nu}{\sin\alpha}\}\cdot$$

$$\cdot\{\; \frac{w_{\nu-1}}{\sin\psi_{(\nu-1)\nu}(\alpha)} + \frac{w_\nu}{\sin\alpha}\}^{-1}$$

and
$$K_{(\nu-1)\nu} = 2\, \frac{w_\nu}{\sin\alpha}\{\; \frac{w_{\nu-1}}{\sin\psi_{(\nu-1)\nu}(\alpha)} + \frac{w_\nu}{\sin\alpha}\}^{-1}$$

Repeating the procedure starting at (2.32), but now changing the variable α by $\psi_{\nu(\nu-1)}(\alpha)$, and eliminating S^+_ν which has already been found in (2.34), we write

$$(2.35) \qquad \int_{\Gamma_0} B_q(\alpha)\, e^{-i\kappa_{\nu-1}x\cos\alpha}\, d\alpha = 0 \qquad \text{for } q = 1,2$$

Similarly, we obtain

$$(2.36) \qquad S^-_{\nu-1}(\alpha) = K_{(\nu-1)(\nu-1)}(\alpha)\, [S^+_{\nu-1}(\alpha + \epsilon_{\nu-1}) +$$

$$+ \delta_{(\nu-1)\nu}\, D^+_{\nu-1}\, (\alpha + \epsilon_{\nu-1})] +$$

$$+ \tau_{\nu(\nu-1)}(\alpha)\, K_{\rho(\nu-1)}(\alpha)\,$$

$$\{\; S^-_\nu\, [\; \psi_{\nu(\nu-1)}(\alpha) + \epsilon_\nu\;] +$$

$$+ \delta_{\nu k}\, D^-_\nu\, [\; \psi_{\nu(\nu-1)}(\alpha) + \epsilon_\nu\;]\; \},$$

where
$$K_{(\nu-1)(\nu-1)}(\alpha) = \left[\frac{w_\nu}{\sin\psi_{\nu(\nu-1)}(\alpha)} - \frac{w_{\nu-1}}{\sin\alpha} \right] \cdot$$

$$\cdot \left\{ \frac{w_\nu}{\sin\psi_{\nu(\nu-1)}(\alpha)} + \frac{w_{\nu-1}}{\sin\alpha} \right\}^{-1}$$

and
$$K_{\nu(\nu-1)}(\alpha) = 2\,\frac{w_{\nu-1}}{\sin\alpha} \left\{ \frac{w_\nu}{\sin\psi_{\nu(\nu-1)}(\alpha)} + \frac{w_{\nu-1}}{\sin\alpha} \right\}^{-1}$$

Combining (2.34) and (2.36) yields

$$(2.37) \quad \begin{bmatrix} S_\nu^+(\alpha) \\ \\ S_{\nu-1}^-(\alpha) \end{bmatrix} = \begin{bmatrix} \chi_{\nu\nu} & \chi_{(\nu-1)\nu} \\ \\ \chi_{\nu(\nu-1)} & \chi_{(\nu-1)(\nu-1)} \end{bmatrix} \begin{bmatrix} S_\nu^-(\alpha) + \delta_{\nu k} D_k^-(\alpha) \\ \\ S_{\nu-1}^+(\alpha)\delta_{(\nu-1)k}D_k^+(\alpha) \end{bmatrix}$$

for $\nu = 1,2$, where χ_{uv} denotes the operator, transforming an arbitrary function $f(\alpha)$ according to the following rules

$$(2.38) \quad \chi_{uv}\,f(\alpha) = \tau_{uv}(\alpha)\cdot K_{uv}(\alpha)\cdot f\left[\,\psi_{uv}(\alpha) + \epsilon_\nu\,\right],$$

with
$$K_{uu} = (w_{vu} - w_{uu})\cdot(w_{vu} + w_{uu})^{-1}$$

$$K_{uv} = 2\,w_{uv}\,(w_{uv} + w_{vv})^{-1}\quad\text{for } u \neq v,\text{ and}$$

$$(2.38a) \quad w_{uv} = \rho_u c_u/\sin\psi_{uv}(\alpha)$$

Returning to a two sectorial regions medium with $\mu = 1, 2$, and introducing matrices X, D and T as follows

(2.39)

$$X = \begin{bmatrix} S_1^+(\alpha) \\ S_1^-(\alpha) \\ S_2^+(\alpha) \\ S_2^-(\alpha) \end{bmatrix} \qquad D = \begin{bmatrix} D_1^+(\alpha) \\ D_1^-(\alpha) \\ 0 \\ 0 \end{bmatrix} \qquad T = \begin{bmatrix} 0 & X_{11} & X_{21} & 0 \\ X_{11} & 0 & 0 & X_{21} \\ X_{12} & 0 & 0 & X_{22} \\ 0 & X_{12} & X_{22} & 0 \end{bmatrix}$$

then the system of matrix relation (2.37) can be written in the form of a single operational equation

(2.40) $X = TX + TD$

The elements in X will be obtained by the method of successive approximation employing an iterative scheme described below.

2.5   Method of Successive Iteration

The mathematical formulation of the iterative method permits us to obtain an explicit analytical expression for the approximation of an arbitrary order, which itself, is expressed very conveniently for the physical interpretation of the diffraction field. It will be shown that the final formulae of this method are similar to the ordinary formulae of the method of successive reflection/refraction of

inhomogeneous plane waves in media with plane (non-parallel) boundaries. The distinction is that in the present case, the result of infinite number of reflections/refractions must be required to be integrated along the directions of propagation, as prescribed by the Sommerfeld-Malyuzhinetz integral, in order to account for the choice of geometries -- in our case we expressed the wave field due to the incident wave in polar coordinates (r, θ).

Having clarified some of the connection with mathematical basis for this approach, we will go ahead to present the formal scheme of the method of successive approximation, and the structure of the iterative formula.

Let

$$(2.41) \qquad X^i = TX^{i-1} + TD$$

with $i = 1, 2, 3 \ldots$, and $X^0 = \underline{0}$ where $\underline{0}$ is the null vector. For i large enough, X^i approaches the desired X, and (2.40) is satisfied. We start with $i = 1$ for which

$$(2.42a) \qquad X^1 = TD,$$

and for $i = 2$, (2.41) gives the second approximation

(2.42b) $X^2 = T^2D + TD,$

and so on. Finally we obtained in the limiting form

(2.43) $X = \lim_{N \to \infty} \sum_{i=1}^{N} T^i D$

where

(2.44) $T^i D = T(T^{i-1}D).$

Or, for individual element in X, we can write

(2.45) $S_\nu^\pm = \lim_{N \to \infty} \sum_{i=1}^{N} (T^i D)_\nu^\pm,$ $\nu = 1,2$

where

(2.46) $(T^i D)_1^\pm = \chi_{11} (T^{i-1}D)_1^\mp + \chi_{21} (T^{i-1}D)_2^\pm,$

$(T^i D)_2^\pm = \chi_{12} (T^{i-1}D)_1^\pm + \chi_{22} (T^{i-1}D)_2^\mp,$

$(T^0 D)_1^\mp = D_1^\mp,$ and $(T^0 D)_2^\pm = 0.$

Applying these expressions successively for $i = 1,2,3,..,$ we obtain

$(T^1 D)_1^\pm = \chi_{11} D_1^\mp,$

$$(T^2 D)^{\pm}_1 = X_{11} X_{11} D^{\pm}_1 + X_{21} X_{12} D^{\pm}_1,$$

$$(T^3 D)^{\pm}_1 = X_{11} X_{21} X_{12} D^{\mp}_1 + X_{11} X_{11} X_{11} D^{\mp}_1$$

$$+ X_{21} X_{12} X_{11} D^{\mp}_1 + X_{21} X_{22} X_{12} D^{\mp}_1$$

and

$$(T^1 D)^{\pm}_2 = X_{12} D^{\pm}_1,$$

$$(T^2 D)^{\pm}_2 = X_{12} X_{11} D^{\mp}_1 + X_{22} X_{12} D^{\mp}_1,$$

$$(T^3 D)^{\pm}_2 = X_{12} X_{11} X_{11} D^{\pm}_1 + X_{12} X_{21} X_{12} D^{\pm}_1$$

$$+ X_{22} X_{12} X_{11} D^{\pm}_1 + X_{22} X_{22} X_{12} D^{\pm}_1$$

and so on.

This process can be continued infinitely. However, the structure of the originating expression for arbitrary i can be developed by induction.

Each term in (2.45) can be expressed in the form

$$(2.47) \qquad (T^i D)^{\pm}_{\nu} = \sum_{n(i)=1}^{N(i)} X_{n(i)},$$

where

$$X_{n(i)} = X_{n(i)} D_{n(i)}(\alpha),$$

$$D_{n(i)}(\alpha) = [\alpha + a_{n(i)}]^{-1}$$

$$a_{n(i)} = \begin{cases} a_1^{\pm} \\ a_1^{\mp} \end{cases} \quad \text{for i being} \begin{matrix} \text{even} \\ \text{odd} \end{matrix} \quad , \nu = 1, \text{ and}$$

$$\begin{cases} a_1^{\mp} \\ a_1^{\pm} \end{cases} \quad \text{for i being} \begin{matrix} \text{even} \\ \text{odd} \end{matrix} \quad , \nu = 2$$

$$a_1^{\pm} = \pm(\theta_1^{\pm} - \theta_1 + s_1\pi)$$

also, $n(i) = 1,2 \ldots\ldots, N(i)$ are the number of separate terms, with $N(i) = 2^{i-1}$. The designation $X_{n(i)}$ represents the product of operators as follows

(2.48) $X_{n(i)} = X_{f\nu} \cdot X_{ef} \cdot X_{de} \cdot X_{cd} \cdots\cdots X_{ab} \cdot X_{1a}$

where the succession of this sequence takes on three rules governing the indices:

1.   The indices of any successive pair follows ... $X_{vw} X_{uv}$
     ...

2.   The first index of the last multiplier coincides with the index of the k-th region where the incident wave is given. (in the formulation above, k was taken as 1).

3.   The second index of the first multiplier indicates the ν-th propagating element $(T^i D)_\nu^{\pm}$ of matrix $T^i D$.

     Introducing

$\Omega = -\theta_1 + s_1\pi$, and realizing that

$$-\beta = \pm \theta_1^{\pm},$$

we can write

(2.49) $a_1^{\pm} = -\beta \pm \Omega,$

or

$$a_{n(i)} = -\beta \pm \Omega \quad \text{for } i \text{: even,} \quad \nu = 1$$
$$-\beta \mp \Omega \quad\quad\quad \text{odd} \quad \nu = 1$$
$$-\beta \mp \Omega \quad\quad\quad \text{even} \quad \nu = 2$$
$$-\beta \pm \Omega \quad\quad\quad \text{odd} \quad \nu = 1.$$

Lastly, we designate

(2.50) $a_{n(i)}^{\pm} = -\beta \pm (-1)^{\nu+i+1}\Omega$

$$= -\beta \pm \Omega_{\nu i}$$

where $\Omega_{\nu i} = (-1)^{\nu+i+1}\Omega$

$$= (-1)^{\nu+i}(\theta_1 - s_1\pi)$$

Hence, the operand takes on a compact form of

$$D_{n(i)}^{\pm}(\alpha) = (\alpha + a_{n(i)}^{\pm})^{-1}.$$

Each term in (2.47) can be written in a form reflecting the result of the multi-application of operators as shown in (2.48). For this, we introduce

(2.51a) $\qquad U_{uv}(\alpha) = \tau_{uv}(\alpha) \cdot K_{uv}(\alpha)$

(2.51b) $\qquad f_{uv}(\alpha) = \phi_{uv}(\alpha) + \epsilon_\mu$

(2.51c) $\qquad \alpha_{kv}(\alpha) = f_{ku}(f_{uv}(f_{un} \ldots \ldots f_{wm}(f_{m\nu}(\alpha))) \ldots))$

where functions $\tau_{uw}(\alpha)$, $\phi_{uw}(\alpha)$ are defined in (2.8), and the coefficients of reflection-refraction $K_{uv}(\alpha)$ in (2.38a). Then the result of the operation (2.38) can be written in the form

(2.52) $\qquad x_{uv}f(\alpha) = U_{uv}(\alpha)f(f_{uv}(\alpha)).$

Using this expression, we can find successively

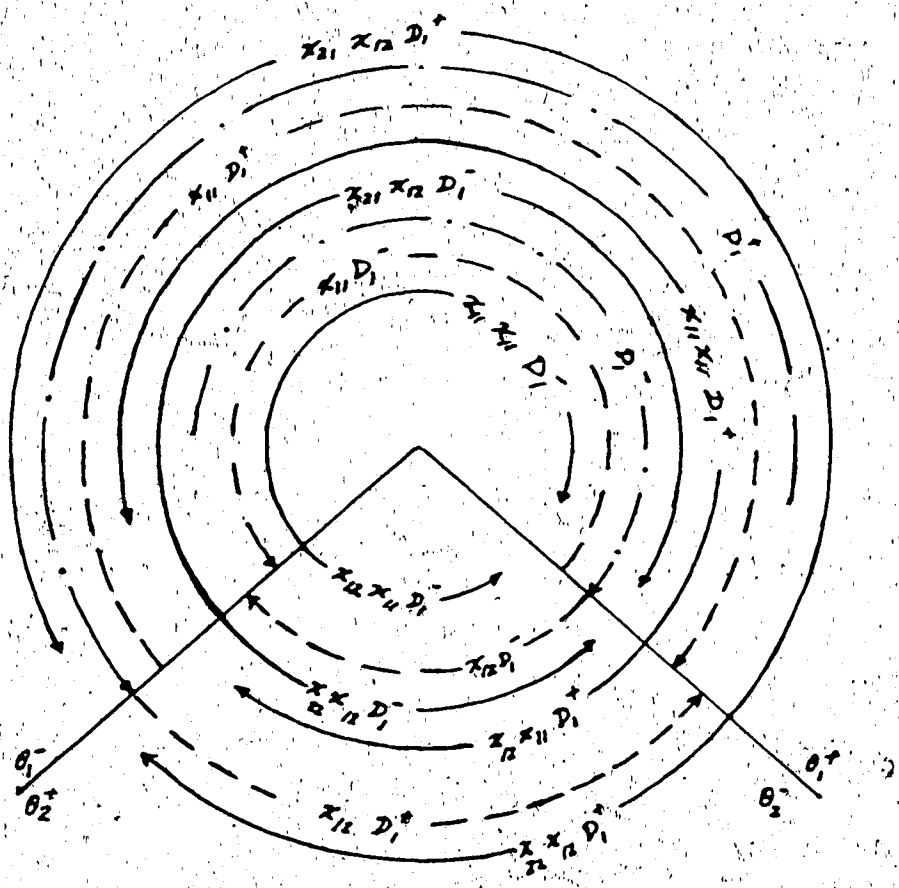$$x_{1a}D_{n(i)} = U_{1a}(\alpha) D_{n(i)}(f_{1a}(\alpha)),$$

$$x_{ab}x_{1a}D_{n(i)} = U_{ab}(\alpha)U_{1a}(f_{ab}(\alpha)) D_{n(i)}(f_{1a}(\alpha))(f_{ab}(\alpha))),$$

and finally

$$(2.53) \quad X_{n(i)} = U_{f\nu}(\alpha)U_{ef}(f_{f\nu}(\alpha))U_{de}(f_{ef}(f_{f\nu}(\alpha)) \cdot$$

$$U_{cd}(f_{de}(f_{ef}(f_{f\nu}(\alpha)))) \ldots$$

$$U_{1a}(f_{ab} \ldots f_{cd}(f_{de}(f_{ef}(f_{f\nu}(\alpha)))) \ldots) \cdot$$

$$d_{n(i)}(f_{1a}(f_{ab} \ldots f_{cd}(f_{de}(f_{ef}(f_{f\nu}(\alpha)))) \ldots)).$$

$$= U_{f\nu}(\alpha)U_{ef}(\alpha_{f\nu}U_{de}(\alpha_{e\nu}U_{cd}(\alpha_{d\nu}) \ldots$$

$$\ldots U_{1a}(\alpha_{a\nu}D_{n(i)}(\alpha_{1\nu}).$$

The ensemble of terms of $X_{n(i)}$ in the sum of (2.47) for any i can be arranged with aid of a graph, similar to a radial scheme, applied for the enumeration of waves originated from stratified media. An example of such a graph, arranging the elements of the sum for i = 1 and i = 2 are shown in Fig. 4. Here, each are of the circumference in the region with index ν is shown to correspond to one of the terms of (2.47) for the same value ν. The axis, in counter-clockwise direction, correspond to the elements of the sum $(T^i D)_\nu^+$, and those in clockwise direction, elements of the sum $(T^i D)_\nu^-$.

Figure 4   Arrangement of terms of $X_{n(i)}$ in

   equation 2.53.

$x_{21}\, x_{12}\, D_1^+$

$x_{11}\, D_1^+$

$x_{21}\, x_{12}\, D_1^-$

$x_{11}\, D_1^-$

D_1^+

$x_{21}\, x_{11}\, D_1^-$

D_1^-

$x_{11}\, x_{11}\, D_1^+$

$x_{12}\, x_{11}\, D_1^-$

$x_{12}\, D_1^-$

$x_{11}\, x_{12}\, D_1^-$

$x_{12}\, x_{11}\, D_1^+$

θ_1^-

θ_2^+

$x_{12}\, D_1^+$

$x_{12}\, x_{12}\, D_1^+$

θ_1^+

θ_2^-

CHAPTER 3

SHADOW BOUNDARY AND THE DIFFRACTED WAVE

For future calculation and physical analysis, it will
be convenient to introduce the idea of generalized wave, in
analogy with the corresponding notion for wave propagation
treatment in stratified media described by Wiggins and
Helmberger (1974).

Within the context of this investigation, a generalized
wave will be such as described by a Sommerfeld integral of
the type in equations (2.25) or (2.28a,b), satisfying the
general form of the Helmholtz equation (2.20). Each of the
functions $D_1^\pm(\alpha)$, or $S_\nu^\pm(\alpha)$ will be composed of a unique
sequence of χ_{uv}, which would require the computation of a
unique product of reflection-transmission coefficients.

In particular the term $F_1^{\circ\pm}$ in formula (2.28a)
corresponds to a primary generalized wave, which from now on
will be designated as $F_{n(o)}$. After a change of variable ($\alpha \to$
$\alpha + \gamma_R^\pm$), equation (2.25) becomes

$$(3.1) \qquad F_{n(o)} = \frac{1}{2\pi i} \int_{\Gamma_0} (\alpha + \theta - \theta_1 + s_1\pi)^{-1} e^{-i\kappa_{n(o)} r \cos\alpha} d\alpha.$$

The composition of $F_{n(o)}$ may be examined by first

deforming the path of integration Γ_0. It will be represented by the sum of Γ_i ($i=1,2,3$) as shown in Fig. 2. Substituting for the variable α by $\alpha \mp \pi$ (-ve for Γ_1 and +ve for Γ_2), and reversing the direction for Γ_2, one may obtain

(3.2) $\qquad F_{n(o)} = F_{n(o)}^{\circ} + F_{n(o)}^{d}$,

with $\qquad F_{n(o)}^{d} = F_{n(o)}^{*}(\psi - \lambda^{-}) - F_{n(o)}^{*}(\psi - \lambda^{+})$

and $\qquad F_{n(o)}^{*} = \frac{1}{2\pi} \int_{\Gamma_0} \frac{1}{(\alpha+\psi)} e^{-i\kappa_1 r \cos\alpha} d\alpha$,

$$\psi = \theta - \theta_1,$$

$$\lambda^{\pm} = \left. \right) s_1 \pi,$$

and Γ is as shown in Fig. 2. The term $F_{n(o)}^{\circ}$ is the residue at the pole of $\alpha = -\psi - s_1\pi$. The next section will discuss the mathematical manifestation of $F_{n(o)}^{*}(\psi)$ followed by the far field determination.

3.1 Discontinuity

Substituting in $F_{n(o)}^{*}(\psi)$ the variable α by $-\alpha$, and the parameter ψ by $-\psi$, one obtains

(3.3) $\quad F^*_{n(o)}(-\psi) = -F^*_{n(o)}(\psi)$,

in so far as $F^*_{n(o)} \neq 0$, the oddness in (3.3) requires that $F^*_{n(o)}$ undergoes a discontinuity at $\phi = 0$.

For the calculation of the above discontinuity, we place the contour Γ along the imaginary axis, going around the origin with a semi-circle of small radius R, such that for $\psi \to 0$, it does not intersect the poles at $\alpha = \psi - s_1\pi$. The two paths Γ^- & Γ^+ (Fig. 5) are shown to represent Γ. The distinction is determined by the placement of the pole, which in turn, signifies the illuminated and shadow regions, by $\psi > 0$ and $\psi < 0$ correspondingly, or vice versa.
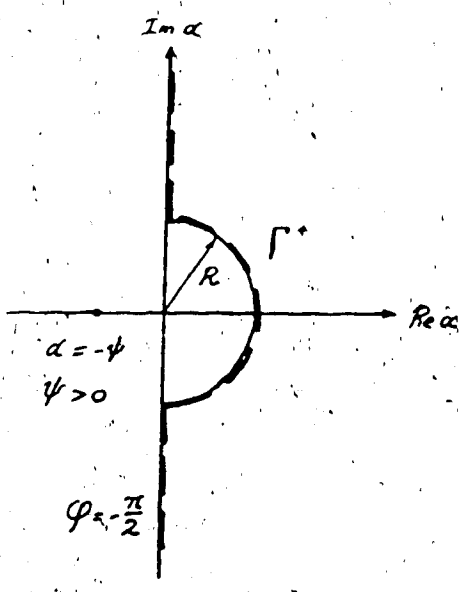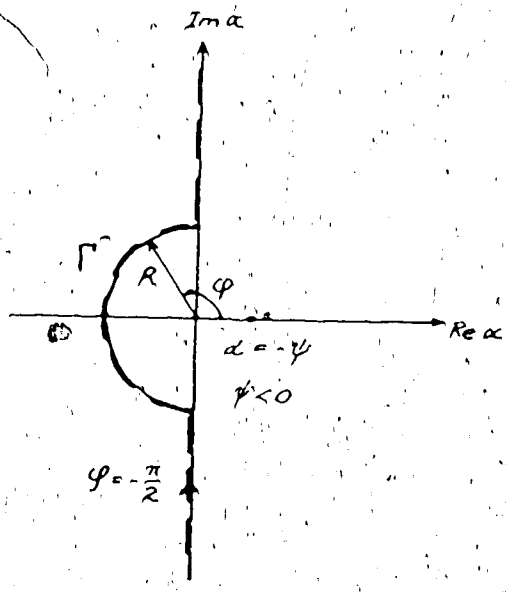
For $\psi \to \pm 0$, the integral in equation (3.1) along Γ^- or Γ^+ has the same magnitude, and quantitatively, the discontinuity of $F^*_{n(o)}$ at the origin ($\psi = 0$) is described by the contribution along the semi-circle. Let

(3.4) $\quad \alpha = R \cdot e^{i\phi}$,

then

Figure 5   Contours of integration Γ^+ and Γ^-.

Γ^-

R

φ

$\operatorname{Im}\alpha$

$\operatorname{Re}\alpha$

$\alpha = -\psi$

$\psi < 0$

$\varphi = -\dfrac{\pi}{2}$

a

$\operatorname{Im}\alpha$

R

Γ^+

$\operatorname{Re}\alpha$

$\alpha = -\psi$

$\psi > 0$

$\varphi = -\dfrac{\pi}{2}$

(3.5) $\underset{\psi \to 0}{\text{Lim}} \; F^*_{n(o)}(\psi)$

$$= \frac{R}{2\pi} \underset{\psi \to \pm 0}{\text{Lim}} \int_{\Gamma_{\pm}} (Re^{i\phi} + \psi)^{-1} e^{i\kappa_1 r \cos\alpha(\phi) + i\phi} \, d\phi,$$

For $R \to 0$, $\alpha(\phi)$ in the exponent goes to zero. Then

(3.6) $\underset{\psi \to \pm 0}{\text{Lim}} \; F^*_{n(o)}(\psi) = \frac{1}{2\pi} e^{i\kappa_1 r} \cdot \int_{\Gamma_{\pm}} d\phi$

(3.7) $\qquad\qquad = (\text{sgn } \psi) \cdot \frac{1}{2} e^{i\kappa_1 r}$

Hence, it is shown here mathematically that the change in magnitude of the discontinuity across the shadow boundary. Result of equation (3.7) will be used subsequently in the determination of the diffracted field.

3.2   Sum of Discontinuous Functions

The magnitude of the discontinuity, from the terms of $F^*_{n(o)}(\psi-\lambda^-)$ and $-F^*_{n(o)}(\psi-\lambda^+)$ at the point $\psi = \lambda^{\pm}$, are such that their sum in equation (3.2) will become a continuous function of ψ, provided that

$$(3.8) \qquad F_{n(o)}^{*}(\psi) = \begin{cases} F_1^o & \lambda^+ \le \psi \le \lambda^- \\ & \text{for} \\ 0 & \psi < \lambda^+, \; \lambda^- < \psi \end{cases}$$

Thus, each term in (3.2) is a discontinuous function of coordinate ψ, and all sums are continuous functions of ψ.

One may rewrite (3.2) into the following form:

$$(3.9) \qquad F_{n(o)} = \begin{cases} \widetilde{F}_{n(o)}(\psi-\lambda^-) + \widetilde{F}_{n(o)}(\psi-\lambda^+) & \psi < \lambda^+ \\ -\widetilde{F}_{n(o)}(\psi-\lambda^-) + \widetilde{F}_{n(o)}(\psi-\lambda^+) + F_1^o(\psi) & \lambda^+ \le \psi \le \lambda^- \\ \widetilde{F}_{n(o)}(\psi-\lambda^-) + \widetilde{F}_{n(o)}(\psi-\lambda^+) & \lambda^- < \psi \end{cases}$$

where

$$(3.10) \qquad \widetilde{F}_{n(o)}(x) = F_{n(o)}^{*}(|x|),$$

while

$$(3.11) \qquad F_{n(o)}^{d} = \eta^- \widetilde{F}_{n(o)}(\psi-\lambda^-) - \eta^+ \widetilde{F}_{n(o)}(\psi-\lambda^+)$$

$$(3.12) \qquad \eta^{\pm} = \text{sgn}(\psi-\lambda^{\pm})$$

3.3   Riemann Surface

A substitution of equations in (3.9) back in the form of $F_{n(o)}^{*}(\psi)$ as in equation (3.5) reveals that the variable ψ may take on the whole interval of $-\infty \leq \psi \leq \infty$. Therefore, (3.9) defines the function $F_{n(o)}(r,\theta)$ on an infinite Riemann surface $0 \leq r \leq \infty$, $-\infty \leq \psi \leq \infty$, as shown in Fig. 6. The following description gives a dissection as far as the regions of applicability are concerned.

(i) Region I: $\theta < \theta_1 + \lambda^+$

(3.13) $F_{n(o)} = -\tilde{F}_{n(o)}(\theta-\theta_1-\lambda^-) + F_{n(o)}(\theta-\theta_1-\lambda^+)$

(ii) Region II: $\theta_1 + \lambda^+ \leq \theta \leq \theta_1 + \lambda^-$

(3.14) $F_{n(o)} = -\tilde{F}_{n(o)}(\theta-\theta_1-\lambda^-) - \tilde{F}_{n(o)}(\theta-\theta_1-\lambda^+) +$

$+ F_1^o(\theta-\theta_1)$

(iii) Region III: $\theta < \theta_1 + \lambda^-$

(3.15) $F_{n(o)} = -\tilde{F}_{n(o)}(\theta-\theta_1-\lambda^-) - \tilde{F}_{n(o)}(\theta-\theta_1-\lambda^+)$

In the above matching, $F_{n(o)}$ becomes continuous on the whole Riemann surface $-\infty \leq \theta \leq \infty$.
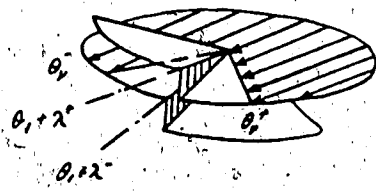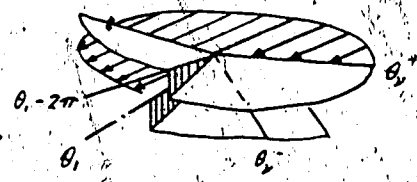
Figure 6   Riemann surfaces.
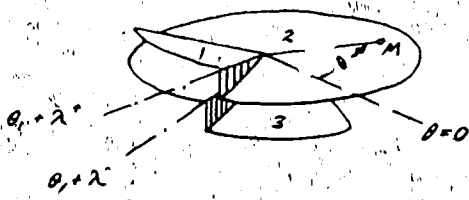
a
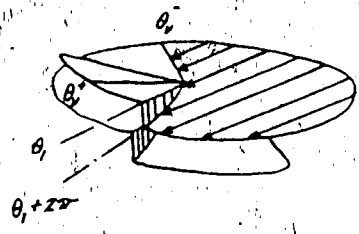
b

c

d

In so far as the solution of the diffraction problem is
concerned, we are only interested in the Euclidean space of
$-\pi \le \theta \le \pi$. Each wedged sector $\theta_\nu^+ \le \theta \le \theta_\nu^-$ belongs to only
part of the Riemann surface. This will be termed the
"physical" part, while the regions $\theta < \theta_\nu^+$ and $\theta_\nu^- < \theta$ the
"mathematical" part, of the Riemann surface. With each
particular problem, we obtain the solution for diffraction
in the "physical" Euclidean space. However, certain
particular solution would lend itself its definition with
aid of the "mathematical" part too (e.g. leaky mode).

3.4 Branch Regions

This section examines the disposition of the regions as
defined in (3.9), upon variations in the direction of the
incident wave and the position of the boundary of the
"physical" part of the Riemann surface. Fig. 7 shows the
mapping of the different regions defined for $F_{n(o)}$ in the
usual Euclidean space. Once again, the $\theta_\nu^\pm$ are designations
for the wedge interfaces. For the incident wave existing in
a particular ν-th sectorial wedge, the direction of its
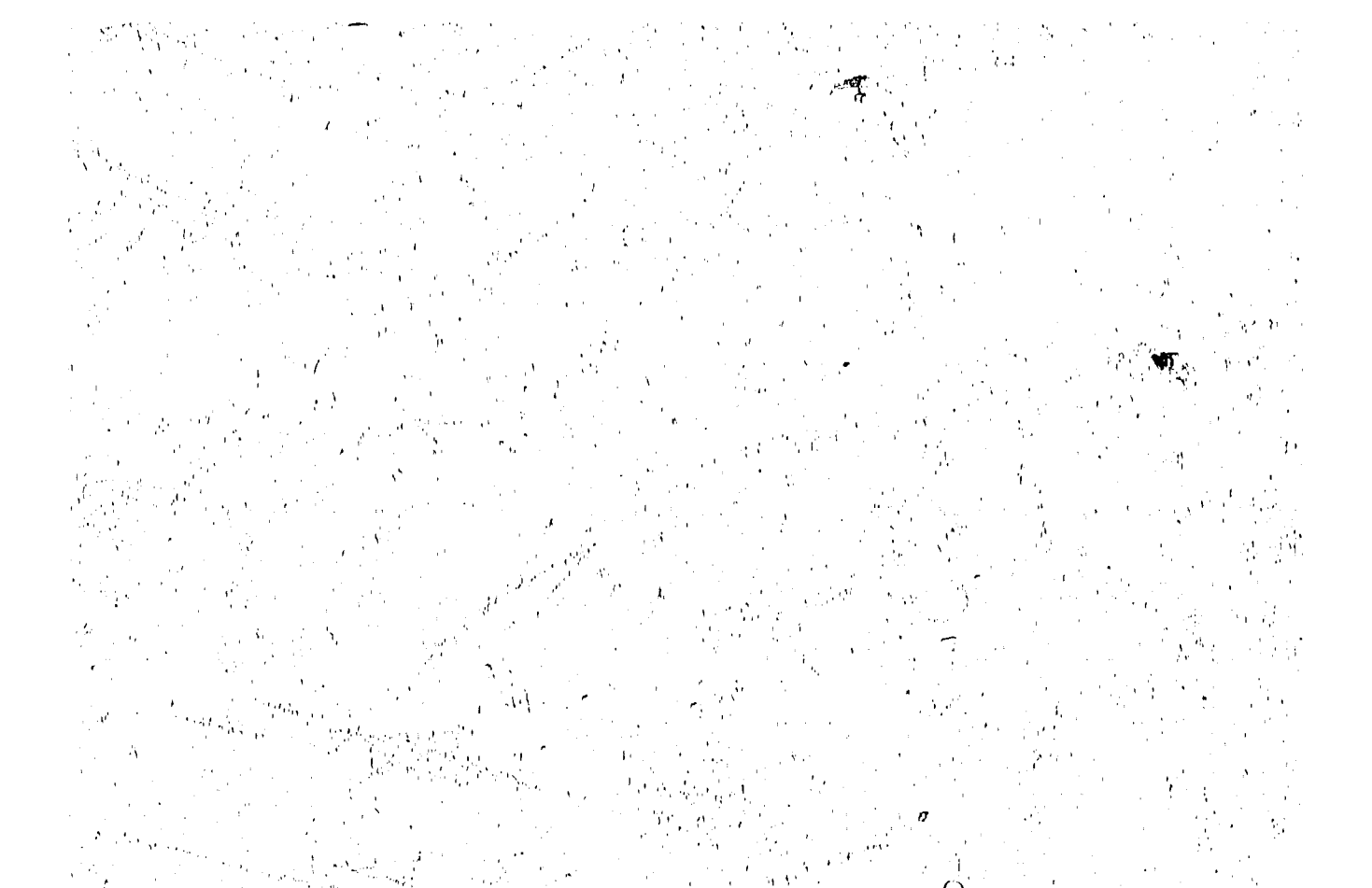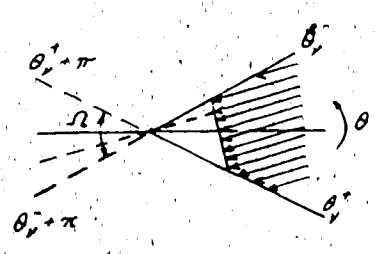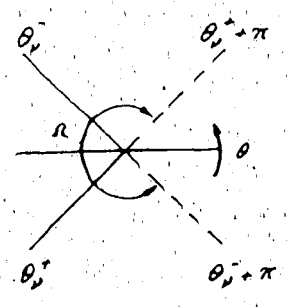propagation (case a,b in Fig. 6) may be restricted by the
following inequality

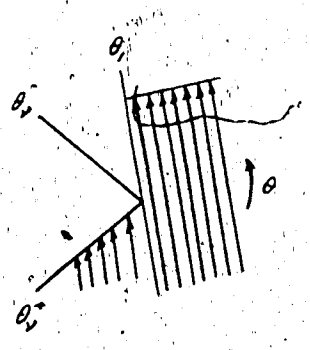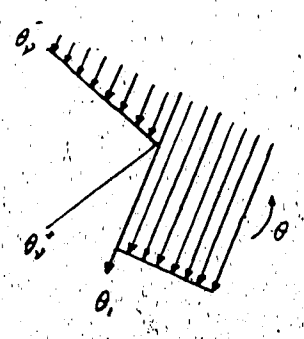Figrue 7 Regions of the defined plane incident
wave in Euclidean space.

a

b

c

d

$$(3.16) \qquad \theta_\nu^+ + \pi < \theta_1 < \theta_\nu^- + \pi.$$

The case of an incident wave propagating parallels to an interface is neglected here.

On the Riemann surface, the region illuminated by the incident wave F_1^0 is defined by the inequality

$$(3.17) \qquad \theta_1 + \lambda^+ \leq \theta \leq \theta_1 + \lambda^-$$

where $\lambda^\pm = -s_1 \pi \mp \pi$.

The rays $\theta = \theta_1 + \lambda^\pm$ are the boundaries of the geometrical shadows for the incident wave. Hence the "physical" space belongs to only part of the region defined by equation (3.17).

Let $\theta_\nu^- - \theta_\nu^+ < \pi$. From (3.17), it follows that the incident wave illuminates the whole wedged sector of $\theta_\nu^+ \leq \theta \leq \theta_\nu^-$ (Fig. 6 a,b). It is clear that there is no boundary shadow in this physical Euclidean space. What follows is a choice in designating the position of the illuminated region with respect to the direction of the propagation of the incident wave, i.e. a choice of s_1 in the original definition for $F_{n(0)}$.

Case I. Illuminated region: $\theta < \theta_1$

$$s_1 = +1,$$

$$\lambda^+ = -2\pi, \qquad \lambda^- = 0,$$

$$(3.18) \qquad \lambda^+ \leq \theta - \theta_1 \leq \lambda^-$$

Case II. Illuminated region: $\theta > \theta_1$

$$s_1 = -1$$

$$\lambda^+ = 0, \qquad \lambda^- = 2\pi,$$

$$(3.19) \qquad \lambda^+ \leq \theta - \theta_1 \leq \lambda^-$$

In both cases, the region for ψ (i.e. $\theta - \theta_1$) is the same, and agrees with the region as defined in (3.9b). Thus, for $\theta_\nu^- - \theta_\nu^+ < \pi$ i.e. incident wave exists in a wedge with an acute sectorial angle, $F_{n(o)}$ in $\theta_\nu^+ \leq \theta \leq \theta_\nu^-$ can always be represented by the sum of three discontinuous fields, one of which is the incident wave.

Now, in the case of $\theta_\nu^- - \theta_\nu^+ > \pi$, we write

a) $\qquad \theta_\nu^+ + \pi \leq \theta_1 \leq \theta_\nu^-,$

b) $\theta_\nu^- \leq \theta_1 + 2\pi,$

c) $\theta_\nu^+ + 2\pi \leq \theta_1 \leq \theta_\nu^- + \pi,$

and consider each situation separately.

The inequality in (a) is depicted in Figs. 6(d) and 7(c). According to geometrical optics, the illumination is in the region $\theta < \theta_1$. Hence

$s_1 = 1,$

$\lambda^+ = -2\pi, \quad \lambda^- = 0,$ and

$\theta - \theta_1 \leq \lambda^-$ in the region of illumination

$\theta - \theta_1 > \lambda^-$ in region of shadow

$\theta = \theta_1 + \lambda^- = \theta_1$ is shadow boundary of incident wave

$\theta = \theta_1 - 2\pi$ is an imaginary shadow boundary for the incident wave.

The last item exists only on the Riemann surface. At the boundary $\theta = \theta_1$, the function $\widetilde{F}_{n(o)}(\psi - \lambda^-)$ experiences a

discontinuity compensating for the discontinuity of the incident wave field. The presence of each discontinuity is reflected in the change of the sign of function $\tilde{F}_{n(o)}$ $(\psi-\lambda^-)$ in expression (8.9). The function $\tilde{F}_{n(o)}$ $(\psi-\lambda^+)$ is continuous in all regions $\theta_\nu^+ \leq \theta$, $\theta \leq \theta_\mu^-$, and it undergoes a discontinuity in the "mathematical" space at the imaginary shadow boundary $\theta = \theta_1 - 2\pi$. The case of situation (c) can be treated similarly.

Situation (b) is analogous to the considered case $\theta_\nu^- - \theta_\nu^+ < \pi$. The function $F_{n(o)}$ is represented by a superposition of three fields, each of which is continuous in the whole region of $\theta_\nu^+ \leq \theta$, $\theta \leq \theta_\nu^-$. One of these fields is the incident field. The two remaining ones represent the discontinuities in the "mathematical" space across the fictitious shadow boundaries.

3.5   Diffraction of Waves

It is clear that the term $F_{n(o)}^d$ in equation (3.2) is used to smooth the discontinuous plane waves across the geometrical shadow boundary, and describes the diffraction of waves diverging from the angular point of the wedge. It should be noted that a term representing the contribution of

.the integral along the real axis (surface waves) will not be included in the present investigation.

From the development in section 3.2, the expression interested becomes $F_{n(o)}^*$ of equation (3.2).

$$(3.20) \qquad F_{n(o)}^*(\psi) = \frac{1}{2\pi i} \int_\Gamma (\alpha + \psi)^{-1} e^{i\kappa_1 r \cos\alpha} \, d\alpha.$$

For large value of the parameter $\kappa_1 r$, i.e. for the far field, the first two non-zero terms are taken as an approximation in the exponent. Therefore, with

$$(3.21) \qquad \cos\alpha \simeq 1 - \frac{1}{2}\alpha^2$$

one obtains

$$(3.22) \qquad F_{n(o)}^*(\psi) = W\, e^{i\kappa_1 r} \{1 + 0\, [\frac{1}{\kappa_1 r}]\}$$

where

$$(3.23) \qquad W = \frac{1}{2\pi i} \int_\Gamma e^{-i\kappa_1 r \alpha^2/2} \cdot (\alpha + \psi)^{-1} \, d\alpha, \qquad \psi \geq 0$$

A well known special function may be used to represent (3.23) through the following manipulation. The path of integration Γ^* (Fig. 5) is mapped into a complex t-plane using the transformation $\alpha = -i\psi\sqrt{t}$. The resulting path is Γ_t

as shown in Fig. 8. Note that

(i)   there is a branch cut on the t-plane along

Re $t \geq 0$, and

(ii)   Re $\sqrt{t} > 0$, if arg $(t) = 0$.

With this transformation, equation (3.23) becomes

$$(3.24) \quad W = -\frac{1}{4\pi} \int_{\Gamma_t} e^{-zt} \left(\sqrt{t} - it \right)^{-1} dt,$$

where $z = -\frac{1}{2} i \kappa_1 r \psi^2$

The contribution from the arc around the origin tends to zero as the radius goes to zero. Hence

$$(3.25) \quad W = -\frac{1}{4\pi} \left\{ \int_0^\infty e^{-zt} \left(-\sqrt{t} - it \right)^{-1} dt - \right.$$

$$\left. \int_0^\infty e^{-zt} \left(-\sqrt{t} - it \right)^{-1} dt \right\}$$

$$(3.26) \quad W = \frac{1}{2\pi} \int_0^\infty e^{-zt} \left[\sqrt{t}(1 + t) \right]^{-1} dt$$

The right hand side of equation (3.26) represents the degenerate form of a hypergeometric function. One acceptable form of representation is

Figure 8   Contour of integration Γ_t in equation 3.24.

Figure 9   Functon $W(w)$ with $\mathrm{Im}(w)=0$.
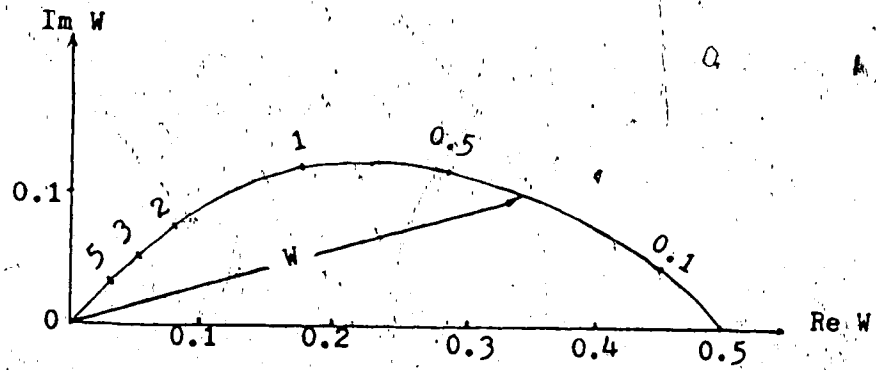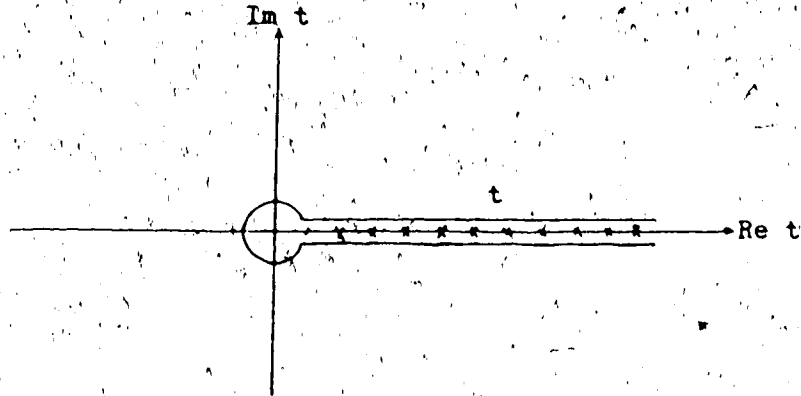
$$(3.27) \qquad W = \frac{1}{2\sqrt{\pi}} \; \Psi \; (\; \tfrac{1}{2} \; ; \; \tfrac{1}{2} \; ; \; z)$$

$$= \frac{1}{2\sqrt{\pi}} \; \Psi \; (\; \tfrac{1}{2} \; ; \; \tfrac{1}{2} \; ; \; \tfrac{1}{2} i \pi w^2)$$

where $\qquad w = (2iz/\pi)^{\frac{1}{2}}$

$$= |\psi| \; (\kappa_1 r/\pi)^{\frac{1}{2}}.$$

For numerical calculation, equation (3.27) may be represented by the more convenient Fresnel integrals, Lebedev (1972) as follows:

$$(3.28) \qquad W = e^z/\sqrt{z} \; \{ \; \frac{1}{\sqrt{2}} - \frac{1}{\sqrt{i}} \; [\; C(iz) + iS(iz)] \; \}$$

where $\qquad S(z) = \sqrt{2/\pi} \int_0^\infty \sin(t^2) \; dt$

and $\qquad C(z) = \sqrt{2/\pi} \int_0^\infty \cos(t^2) \; dt$

The variation of W as a function of w $[= |\psi| (\kappa_1 r/\pi)^{\frac{1}{2}}]$ is shown in Fig. 9.

Hence, for $\kappa_1 r \gg 1$, the function $F^*_{n(o)}(\psi)$ may be described by

$$F^*_{n(o)}(\psi) = W(w) e^{i\kappa_1 r}.$$

Recall from section 3.1, $F_{n(o)}^*$ takes on the sign of the value ψ (i.e. $\theta-\theta_1$). But, in equation (3.10), $\widetilde{F}_{n(o)}(x)$ is introduced as an even function of such parameter. Hence, equation (3.11) becomes

(3.29) $\qquad F_{n(o)}^d = \eta^-\widetilde{F}_{n(o)}(\psi-\lambda^-) - \eta^+\widetilde{F}_{n(o)}(\psi-\lambda^+)$

with $\qquad F_{n(o)} = W(w)\, e^{i\kappa_1 r}$

and $\qquad w = |\psi|(\kappa_1 r/\pi)^{1/2}$.

With the diffracted signal being proportional to the the corresponding geometrical signal along the shadow boundary, we can write.

(3.40) $\qquad w = |\psi|\ \{\ 2r_1 r_0\ /\ (r_0 + r_1)\ \}^{1/2}$.

where r_0 is the radius of curvature of wave front from source point to the point of diffraction, and r_1 is the radius of curvature of the diffracted wave front. The constraint for high frequency approximation restricts the use of the above formula at distance at which

(3.41) $\qquad \kappa_1 r_1 \gg \dfrac{\pi(r_0 + r_1)}{3r_0}$.

CHAPTER 4

NUMERICAL RESULTS

4.1   Introduction

The following numerical calculation for wave
propagation in laterally inhomogeneous media uses Equation
3.22 in section 3.5 in conjunction with asymptotic ray
theory. Whereas the latter provides the wave field of the
geometric arrivals, it suffers a discontinuity because of
the shadow boundary. The edge wave theory gives the
necessary smoothing diffraction component, and incorporates
the result in Chapter 3 as well as the kinematic properties
provided by the ray method. Note that the acoustic
formulation can be used in the SH case by replacing the
displacement field by the presssure field.

The first model to be discussed is a box-type media,
devised for prediction of seismic response for a tar-sand
structure under study by a major oil company. It was also
used in testing the algorithm of an analytical-numerical
method (combination of finite difference and finite Hankel
transform) by Alekseev and Mikhailenko (1980), and
Mikhailenko (1984). The dimension and elastic wave
velocities for different sections of this model are as shown

in Fig. 10. It basically consists of three parallel layers

having increasing velocity with depth. A nonconformity in

the middle layer (termed the box), delineated by rectangle

ABCD and denoted as IIa, has a lower velocity than the upper

layer I. The densities of all three layers and the box are

chosen to be equal. All distances are by convention measured

in the unit which equals one wavelength of waves propagating

in layer I, at the principal frequency ω_0 of the source. We

will denote this artificial unit by w. Time is measure in

terms of the period of the source pulse.

The synthetic seismograms for this model as produced by

programs based on the Alekseev-Mikhailenko method (or AMM in

short) are displayed in Fig. 11. Two immediate features are

the change in polarization of the first arrival, and the

prominence of some later arrivals. In using the method by

which the total wave field is immediately calculated, it

does not provide much physical insight as to the influence

of each separate feature of the structure to the total

response. The major goal of our application is to identify

the significance of the individual diffracted arrivals

originated at the corners A, B, C and D, and their

associated waves.

Figure 10 The hot tar model.

N.B. rectangle ABCD forms the box, or IIa region
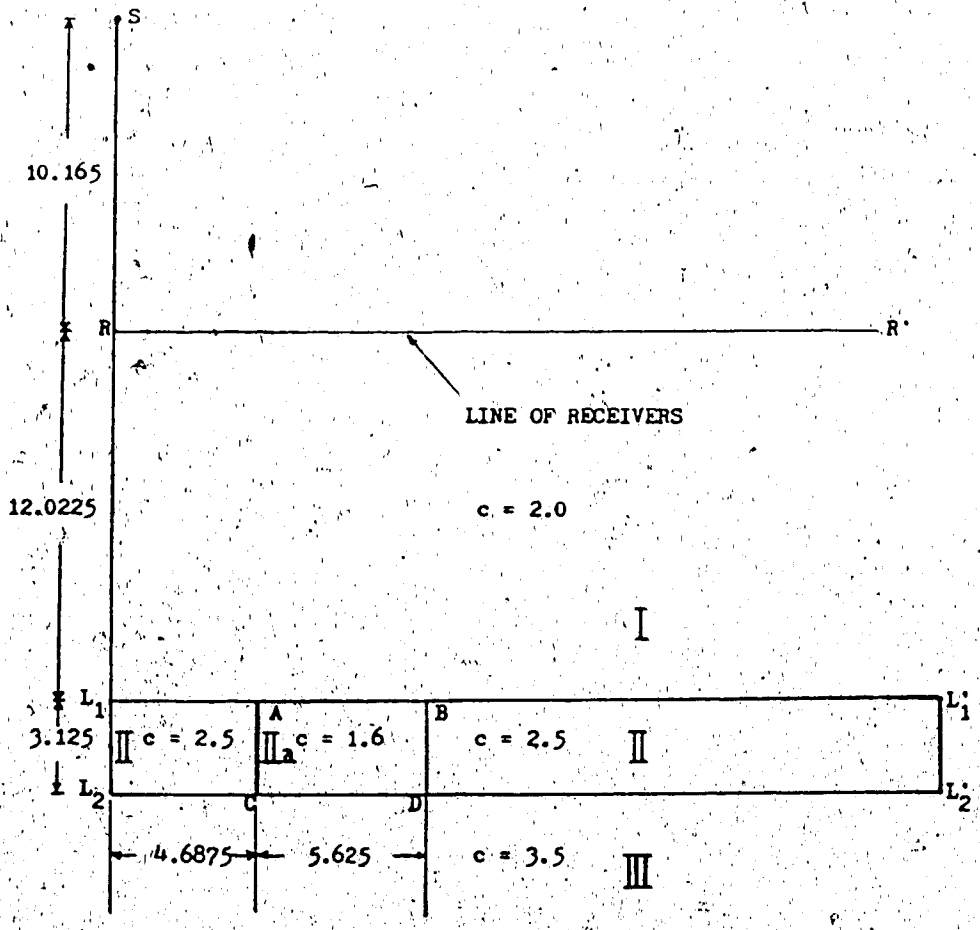
Figure 11 Synthetic seismograms for the hot tar model
based on the Alekseev-Mikhailenko method (AMM).

0.000 WL
0.400 WL
0.800 WL
1.200 WL
1.600 WL
2.000 WL
2.400 WL
2.800 WL
3.200 WL
3.600 WL
4.000 WL
4.400 WL
4.800 WL
5.200 WL
5.600 WL
6.000 WL
6.400 WL
6.800 WL
7.200 WL
7.600 WL
8.000 WL
8.400 WL
8.800 WL
9.200 WL
9.600 WL
10.000 WL
10.400 WL
10.800 WL
11.200 WL
11.600 WL
12.000 WL
12.400 WL
12.800 WL
13.200 WL
13.600 WL
14.000 WL
14.400 WL
14.800 WL
15.200 WL
15.600 WL
16.000 WL
16.400 WL
16.800 WL
17.200 WL
17.600 WL
18.000 WL
18.400 WL
18.800 WL
19.200 WL
19.600 WL
20.000 WL
20.400 WL
20.800 WL
21.200 WL
21.600 WL
22.000 WL
22.400 WL
22.800 WL
23.200 WL
23.600 WL
24.000 WL
24.400 WL
24.800 WL
25.200 WL

5.00   10.00   15.00   20.00

TIME IN PERIODS

4.2   Computation Scheme

We will use a point source, radiating an exponentially decaying sinusoidal pulse employed in Hron and Kanasewich (1971):

$$f_0(t) = \sin(\omega_0 t) \cdot \exp \left(- \{ \frac{\omega_0 t}{\gamma} \}^2 \right).$$

Choosing $\omega_0 = 2\pi$ and $\gamma = 4$, we have

$$f_0(t) = \sin(2\pi t) \cdot \exp \left(- \{ \frac{\pi t}{2} \}^2 \right).$$

To work in the frequency domain, we will perform a fast Fourier transform on $f_0(t)$ and obtain numerically or analytically its spectrum

$$S_0(\omega) = \mathcal{F}\{ f_0(t) \}.$$

Next, we will compute the following kinematic and dynamic properties of each diffracted ray:

- τ : arrival time
- θ : incident angle
- θ_i : subsequent angles of reflection or transmission along the ray
- r_0 : the radius of curvature of the wave front from source at the point of diffraction.

- r_1 : increment of radius of curvature of the wave front from the point of diffraction to receiver.

- ψ : angle between r_1 and shadow boundary.

With the aid of elastic properties of each section of the medium, we may proceed to compute three major quantities:

(a) The geometrical spreading G using θ, θ_i, r_0, r_1 and the geometric dimensions of the medium, evaluated according to asymptotic ray theory (Cerveny and Ravindra, 1971)

(b) The product of reflection-transmission coefficients K using θ, θ_i, and c_i.

(c) W(w) as a function of angular frequency ω, r_0, r_1, and ψ, see section 3.4.

The last item (c) is the all important relationship between the amplitude of the diffracted wave field at any point and that of the geometric ray along the corresponding shadow boundary.

Finally, we will multiply $S_0(\omega)$ with G·K·W(w), with aid of the eikonal τ. This will give us the response in the

frequency domain. The inverse Fourier transform will provide the response in time domain.

4.3 Grouping of Rays

It was mentioned in section 4.1 that one of the goals in the present application of the diffraction formulae in the ray theory is to interpret the different contributions of different regions of the media. Hence, in dealing with the large number of rays which are always required when using the ray theory, we need a consistant classification of them. But, in view of the moderate complexity of the present model (or any other reasonably complicated models), there seems to be no universal rule to achieve such task.

In the following presentation of the numerical results, the general guidelines for grouping the rays are that the higher the group number, the larger the number of segments in each ray; and/or the more complex the nature of the ray (e.g. doubly diffracted) will be. The seismograms for each group of rays will be assigned a unique identifying number for the individual contribution due to interfaces between the layers, or a particular origin of the diffracted signals. This code also recognizes the rays of the same

arrival time branch.

In general, the discussion of each group will progress in three stages. First, the ray diagrams for such event will be presented using a ray tracing scheme for the specific geometry and elastic properties of the media.

Second, a polar plot of the modulus of the radiation characteristics for each diffracted contribution will be shown, assisted by a sketch of the corresponding shadow boundary. Obviously, for geometric rays, this step will be omitted.

Finally, the corresponding synthetic seismograms will be shown in their elementary form which consists of the discussed wavelets. The ordinary body wave contributions will be added on to the diffracted ones within the same group. Eventually, the groups will be assembled sequentially to form the final simulated response - the synthetic seismograms.

4.4   Group I -- consisting of rays with up to 2 ray segments and are related to the rays reflected from the plane interface L_1L_1.

Fig. 12 shows the ray paths of the geometric reflection in group I. The synthetic seismograms for this event, labelled 1, are shown in Fig. 13. The discontinuities, or rather a reverse in polarities, as observed at receivers near the distance of 7.0 w and 16.0 w are due to the opposite velocity contrast between 'layer I - layer II' and 'layer I layer IIa', i.e. the box. The general diminishing amplitude is a combined effect of geometrical divergence and the gradual change in the reflection coefficients.

Fig. 14 shows the ray paths of the associated diffracted arrivals, generated by the reflected rays in Fig. 12. Fig. 15 reveals that for corner A, there are two shadow boundaries, sharing the same geometrical line. Each interface produces a different bundle of diffracted rays that provides a diffracted contribution in connection with the corresponding discontinued reflector. That is, in Fig. 15b, the geometric reflection off the segment L_1A . terminates at A (see Fig. 10). Then the last ray is depicted by the dashed line, separating the illuminated zone on its left and the shadow zone on its right. While in Fig. 15d, the geometric reflection off the segment AB (the top of the box) terminates at A. This time, the last ray separates the illuminated zone on its right and the shadow zone on its left. Obviously, both shadow boundaries are represented by the same line. Similar treatment is given to corner B in

Figure 12 Ray diagram for group I reflection

(from the first interface L,L_1)
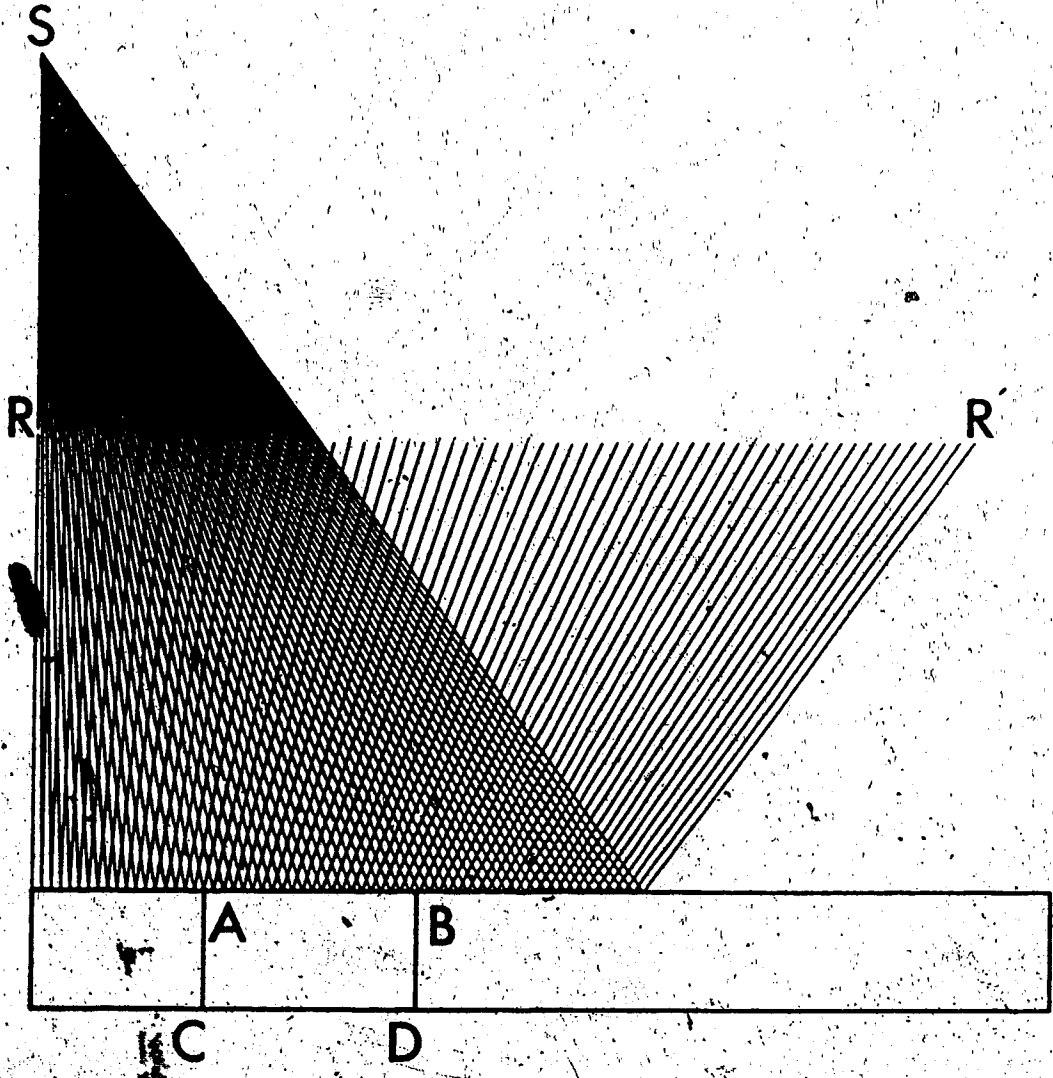
Figure 13 Synthetic seismograms for group I reflecton.

DISTANCE (WAVELENGTHS)

TIME (PERIODS)
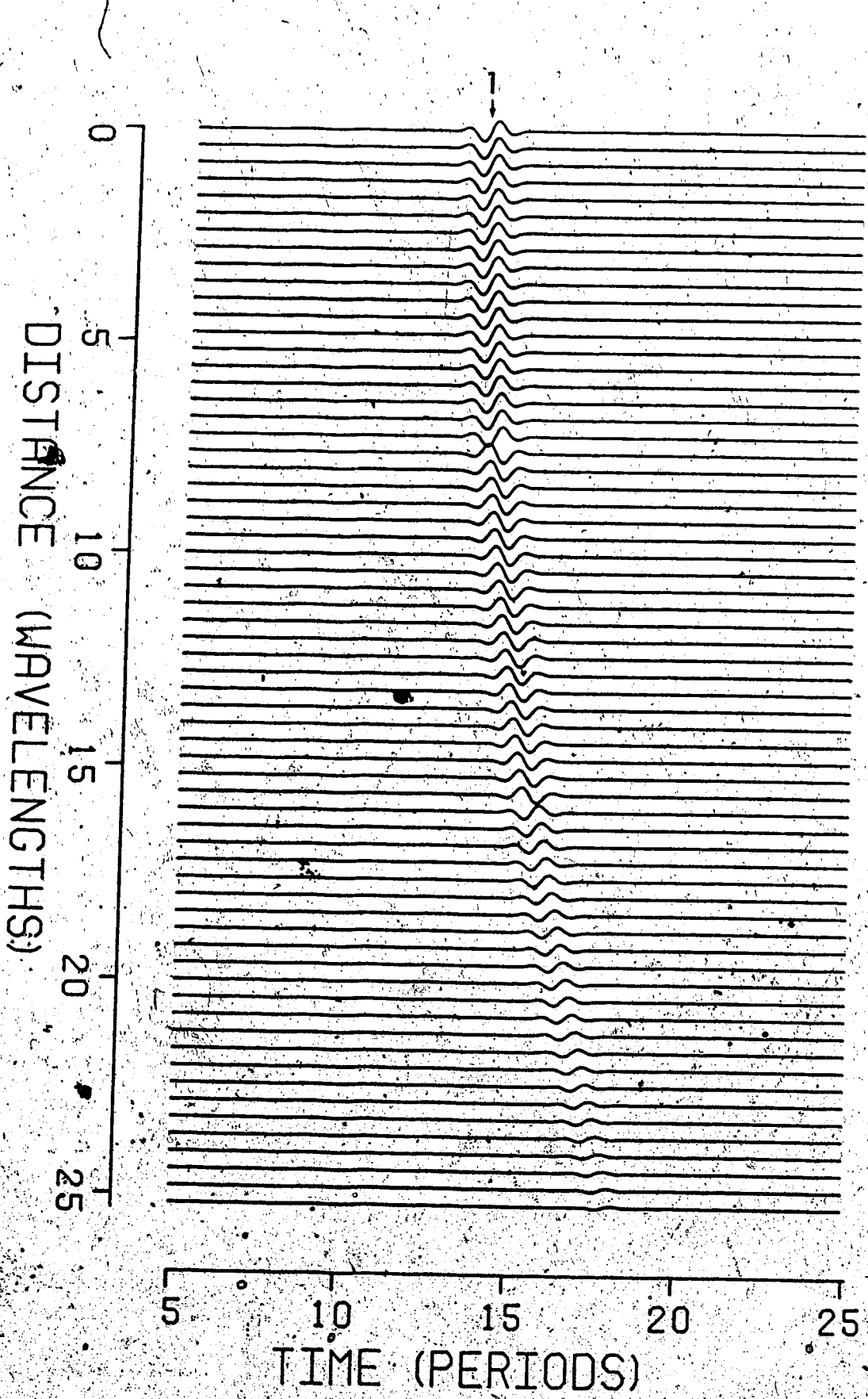
Figure 14 Ray diagram for group I diffractions

associated with the reflected rays in Fig. 12.

N.B. there are two arrivals per receiver

originating either at A or B corner.
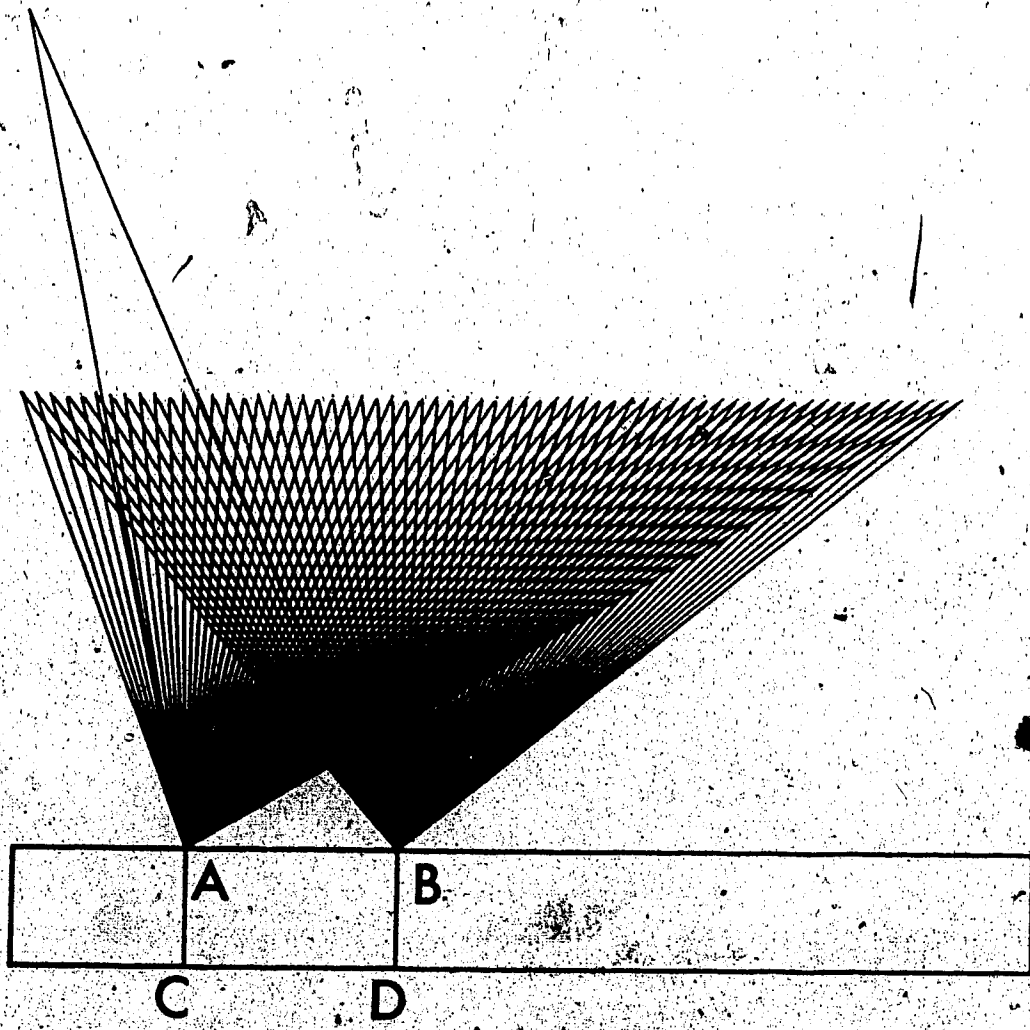
Figure 15 (a)Radiation characteristics for
diffracted rays of group I, approaching
corner A from the left - see Fig. 15b.
(c)Radiation characteristics for
diffracted rays of group I, approaching
corner A from the right - see Fig. 15d.

100%

100%
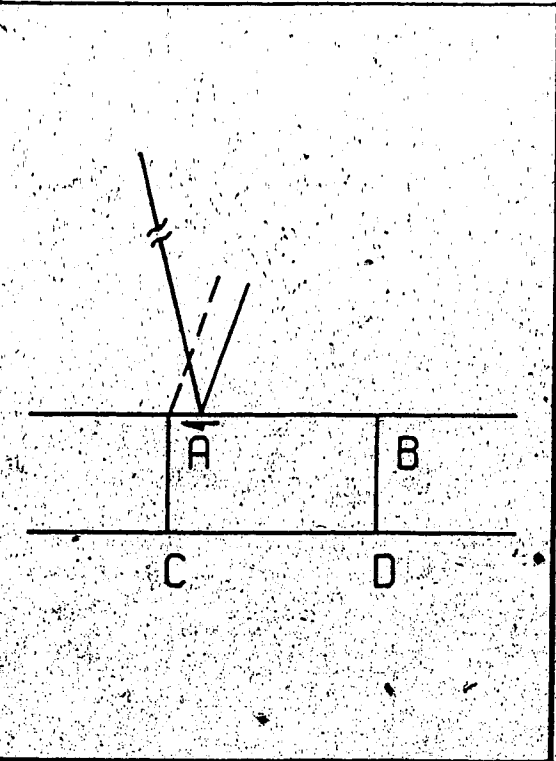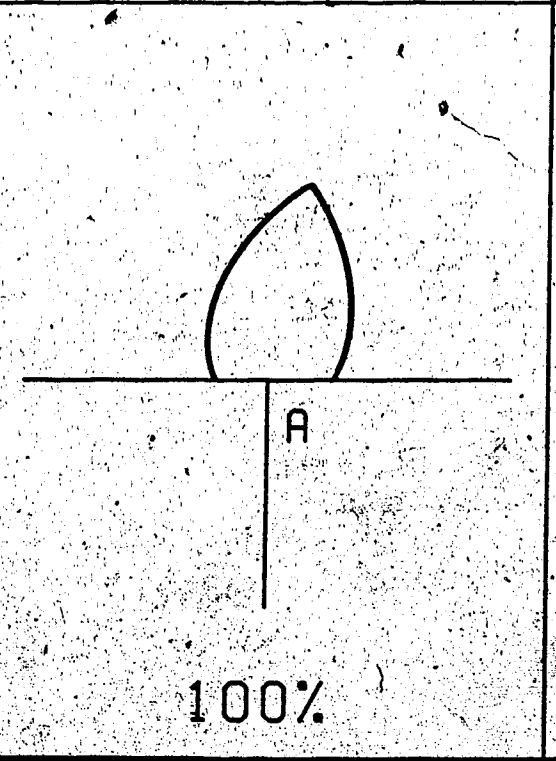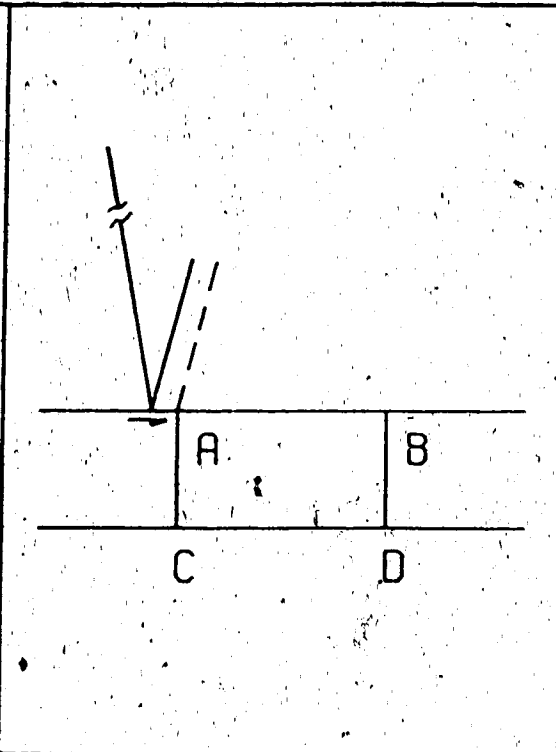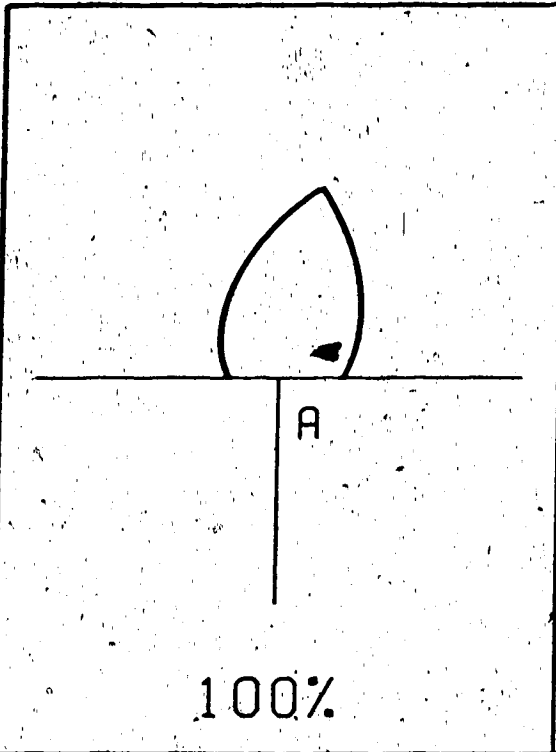
Fig. 16.

Before going into the discussion of the corresponding synthetic seismograms, it should be noted that the percentages as shown in Figs. 15a,b and Figs. 16a,b are for preliminary inspection on the relative strength of each radiation characteristic. The value at the cusp of Fig. 15a is taken as the standard unit. Each radiation characteristic chart has been magnified (or diminished) by multiplying the original value with the percentage shown.

Fig. 17 shows the synthetic seismograms for the diffracted arrivals. Labels 2 and 3 are used to indicate the contributions from corner A and B, respectively. While 3 shows very small amplitude. The changes of polarity indicate the locations where the shadow boundaries intersect the receiver line. Here, it is at distances of 7.2 w (corner A) and 16.0 w (corner B). Note that the signals at receivers between 7.2 w and 16.0 w are of similar phase. In fact, there are 4 wavelets here : a first pair of diffractions depicted in Figs. 15b,d (code 2) and a second pair depicted in Figs. 16s. 16b,d. The two contributions in each pair are out of phase by π. The reflection coefficients for the rays along the two shadow boundaries originated at, say corner A, have opposite signs. In addition, the diffracted contribution carries a positive/negative sign for being on
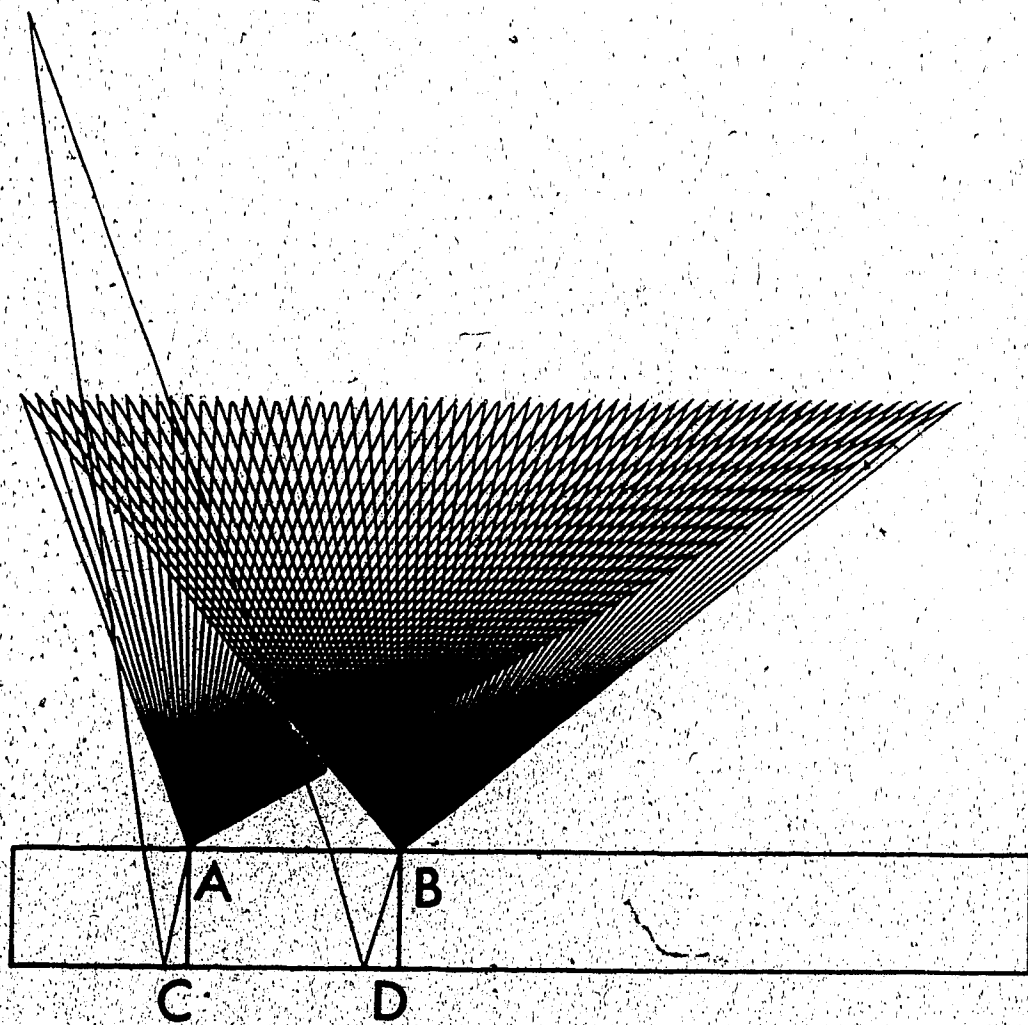
Figure 16   (a) Radiation characteristics for
            diffracted rays of group I, approaching
            corner B from the left - see Fig. 16b.
            (c) Radiation characteristics for
            diffracted rays of group I, approaching
   corner B from the right - see Fig. 16d.
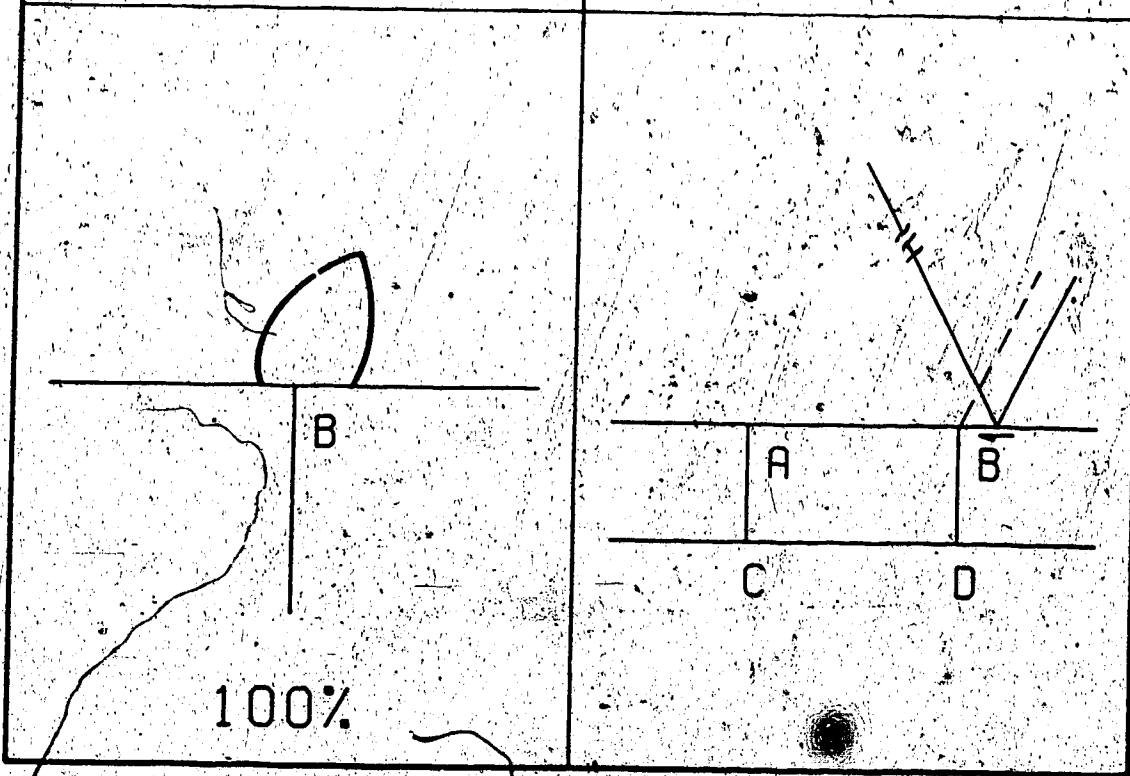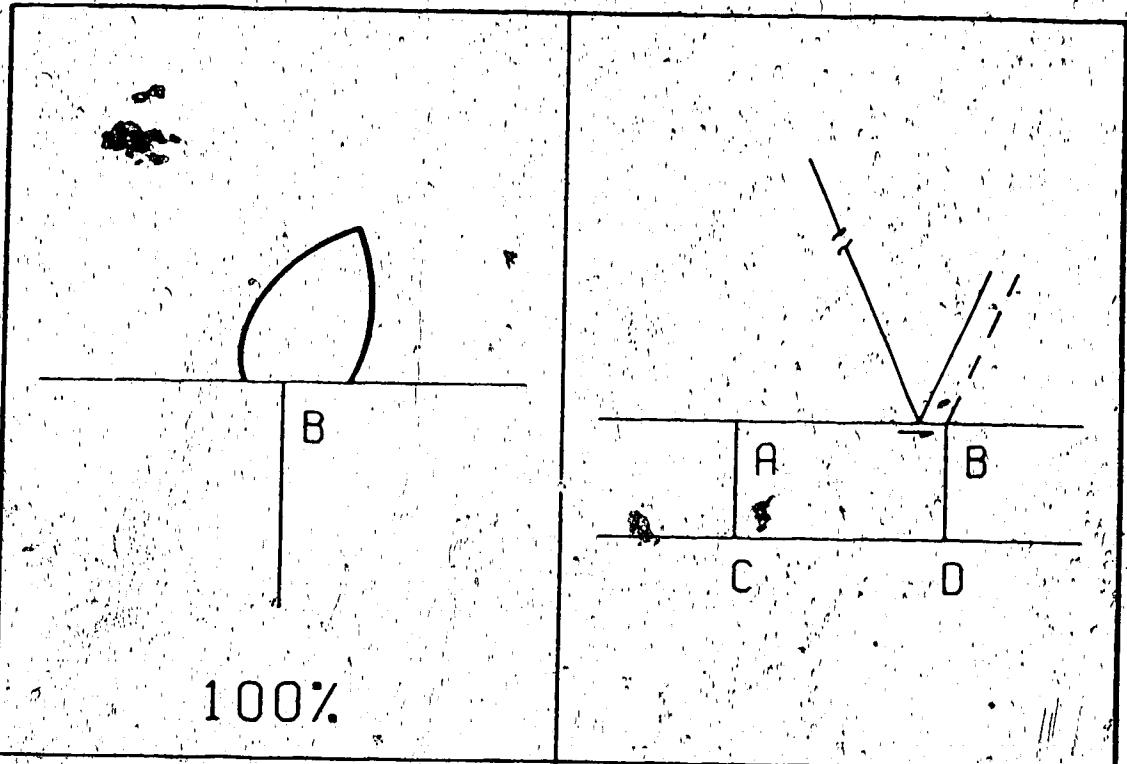
Figure 17 Synthetic seismograms for group I
diffraction
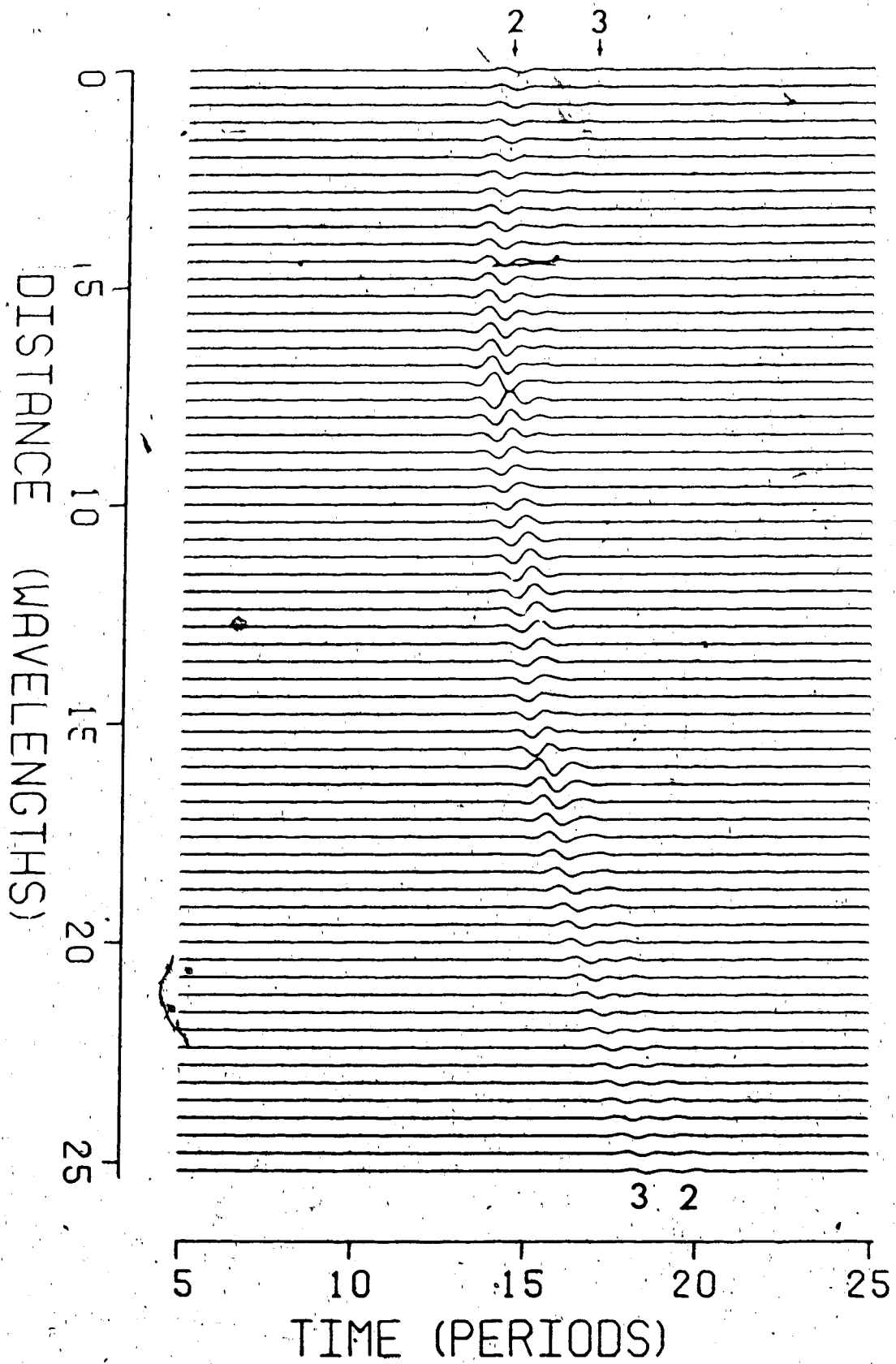
the shadow/illuminated side of the shadow boundary. This results a corresponding change in the polarity.

The amplitude for each contribution decreases rapidly away from the shadow boundary. The smaller amplitudes of the diffracted arrivals originating at corner B of the box (see signals labelled 3) are due to larger geometrical spreading of the reflected waves incident at B and smaller values of the reflection coefficient due to the larger angles of incidence.

In Fig. 18 the synthetic seismograms for rays coded 1, 2 and 3 are added to give the partial contribution of group I rays. Compared with Fig. 13, which gives only the geometric arrivals, the result in Fig. 18 shows that the diffracted arrival eliminates the amplitude discontinuities, an undesired breakdown in the asymptotic ray theory.

4.5   Group II -- consisting of rays with up to 4 ray segments and related to rays once reflected from the second boundary $L_2^{*}L_2^{'}$

Fig. 19 shows the ray paths of the geometric rays in

Figure 18 Synthetic seismograms for
          contributions 1, 2 and 3 in group I.
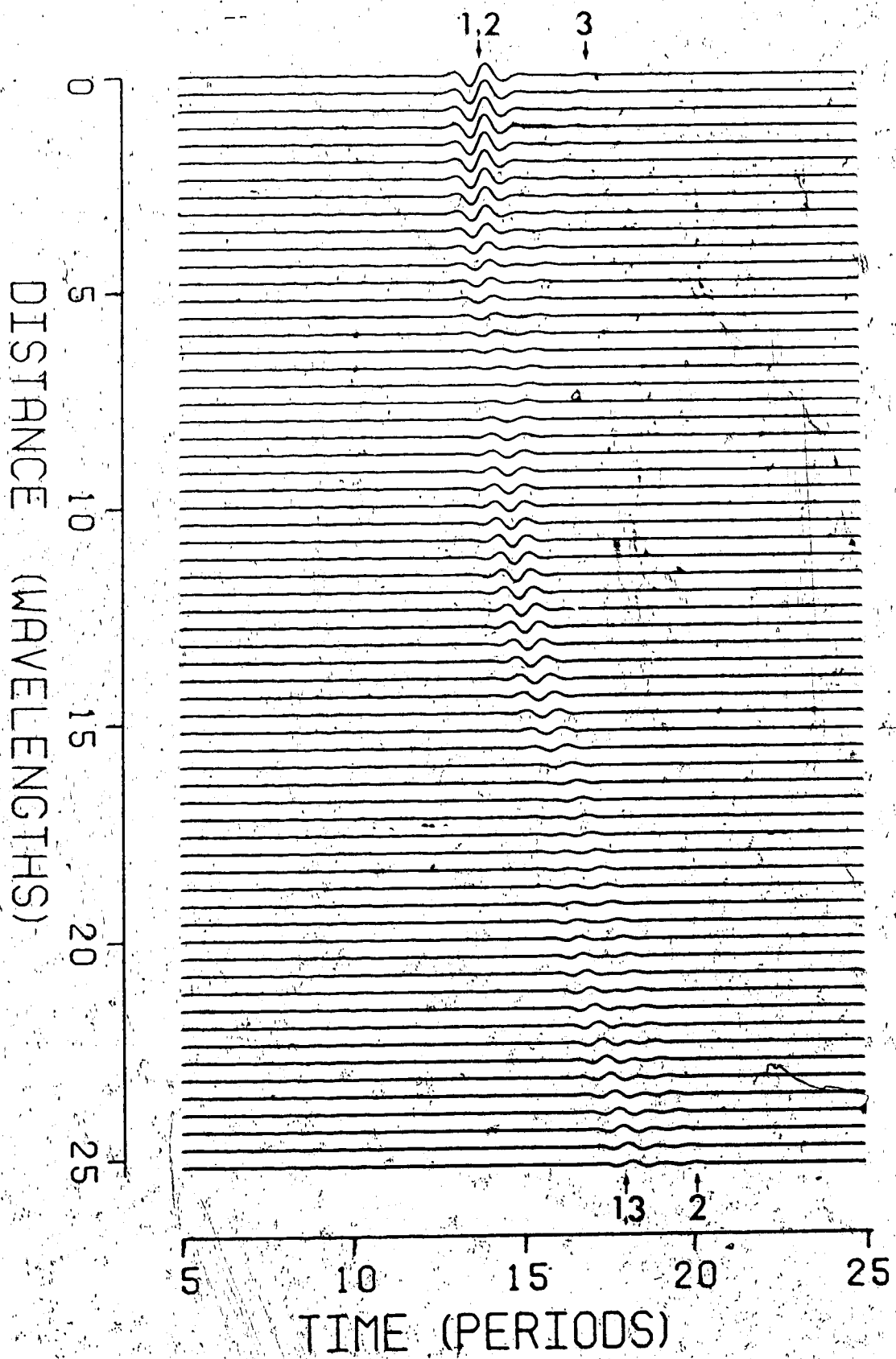
group II. There are 4 segments in a ray. The ray bundles clearly show the locations of the shadow boundaries. In the case of the second bundle which impinges on part of the boundary AB, there are two such boundaries. A closer examination reveals that the diffractions associated with these two boundaries are quite different in both history and pattern. This will be dealt with later.

Fig. 20 shows the synthetic seismograms for the three geometric arrivals mentioned above. Since each bundle of rays belongs to a different time branch on an arrival chart, it is assigned a specific identifying number. The polarities of all signals are the same, except towards the end of rays 6. The reversal is due to the change in phase of the reflection coefficient upon reflection from the CD boundary.

Fig. 21 shows one type of diffraction associated with the geometric ray bundles 4, 5 and 6. Figs. 22b,d may explain more clearly the establishment of the shadow boundaries which are in layer I. The relative amplitudes of the radiation characteristics suggest the effect from corner B would dominate. This is just opposite to the group I diffractions, where diffractions from B were weaker than those from A. Fig. 23 gives the synthetic seismograms for this type of diffracted rays, with codes 7 and 8 denoting contributions from corners A and B, respectively.

Figure 19 Ray diagram for geometric rays in group II

Each ray is transmitted into layer II

(or IIa, the box),b reflected off the second

boundary L_2L_2', and finally transmitted back into

layer I.
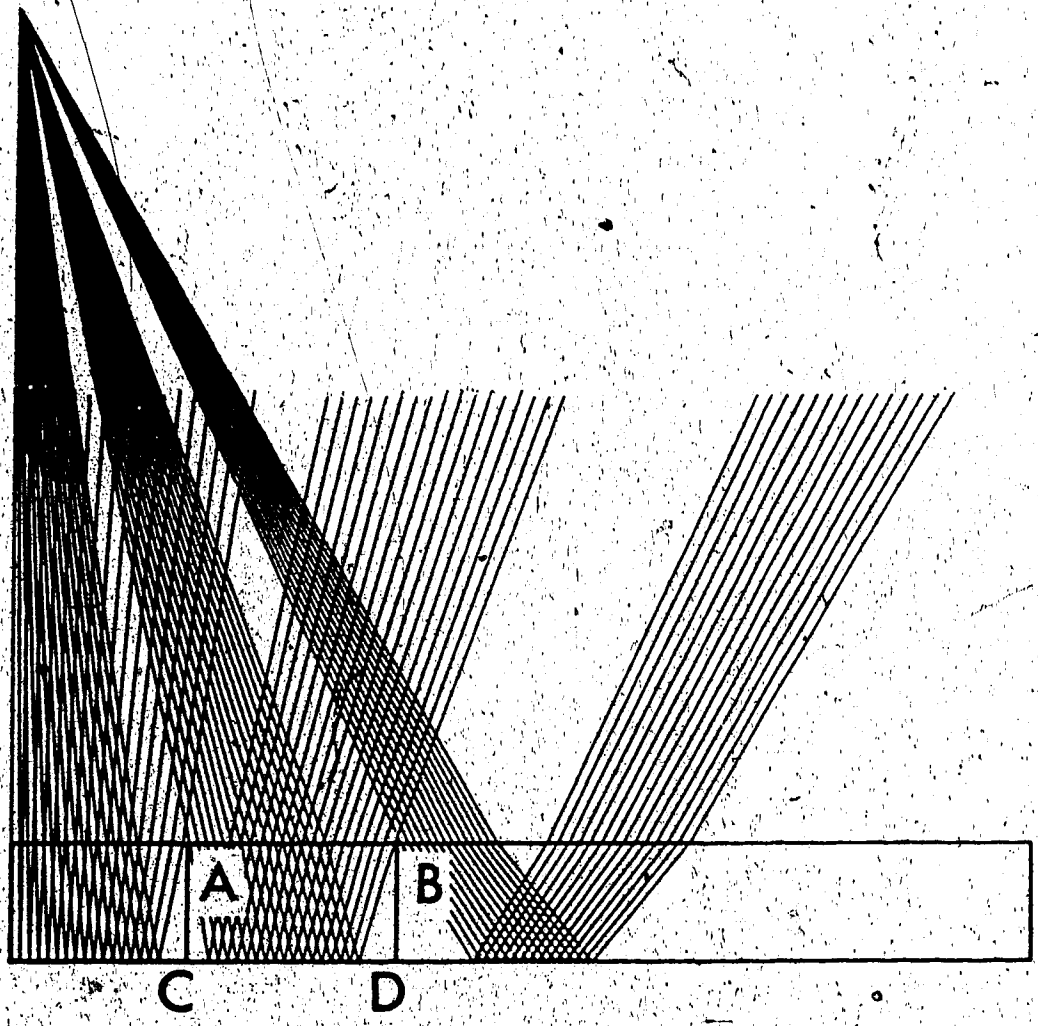
Figure 20 Synthetic seismograms for geometric rays in

group II.

The contributions of three separate bundles

of rays are easily identified.
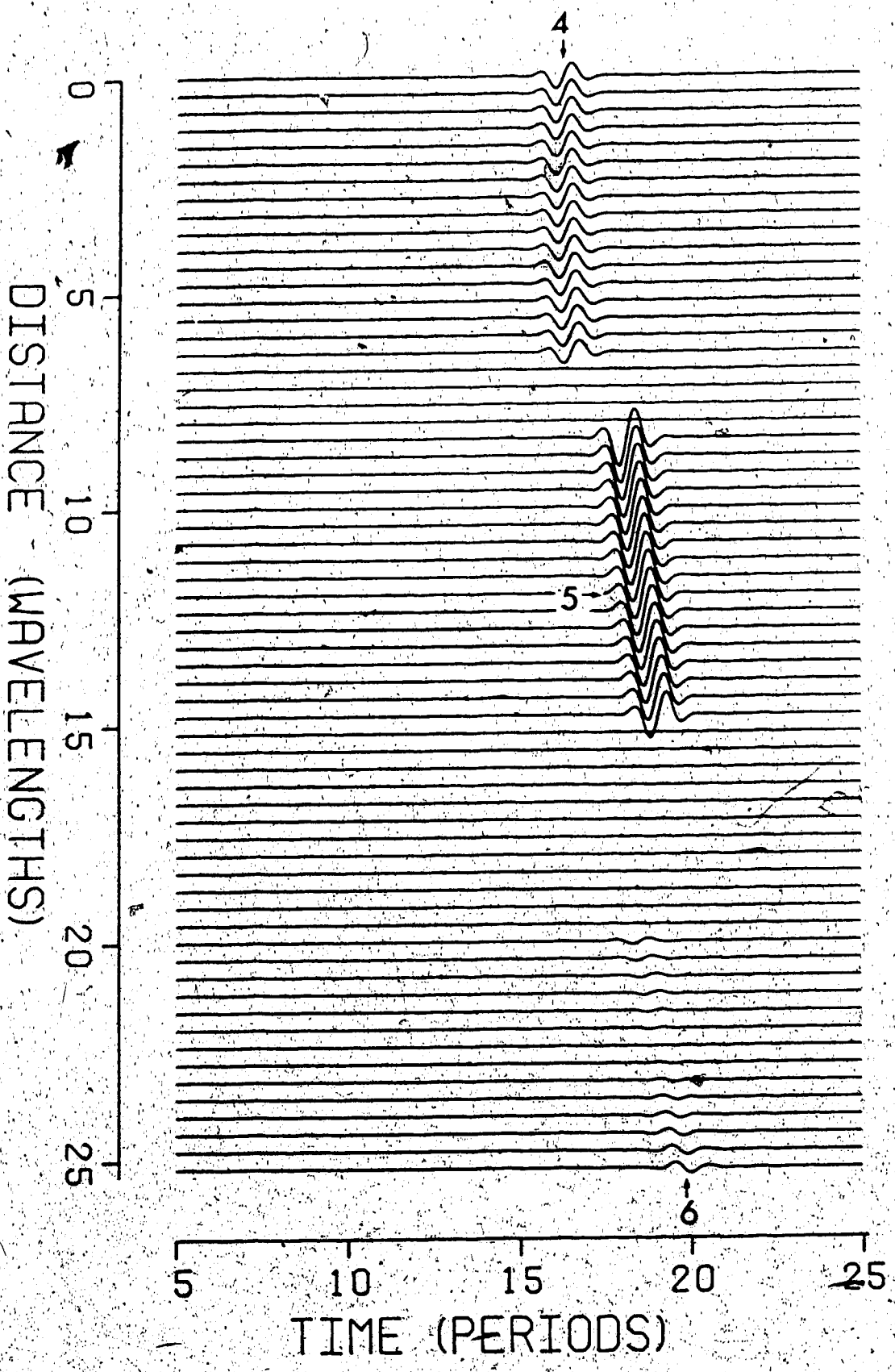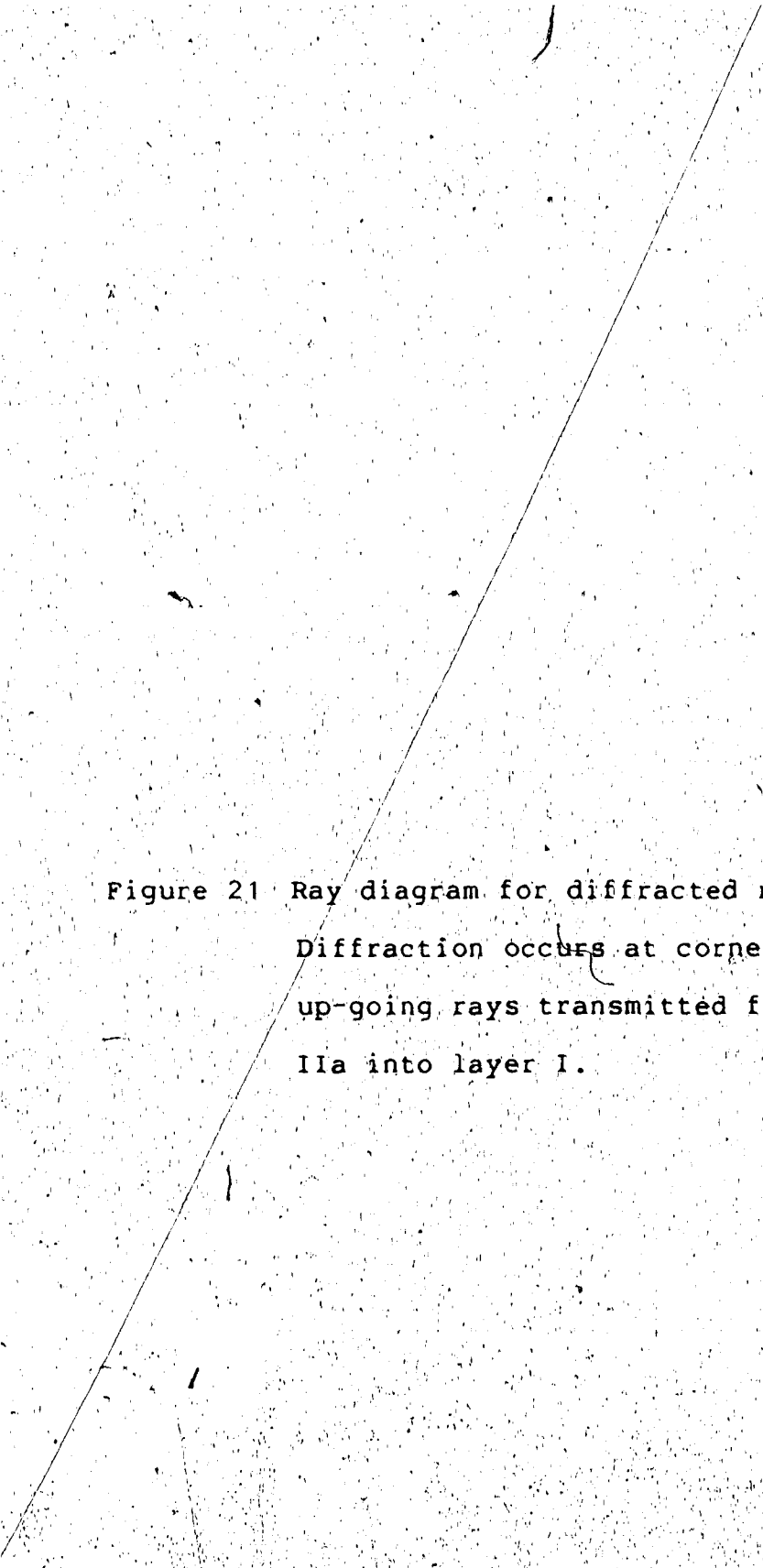
Figure 21 Ray diagram for diffracted rays in group II
Diffraction occurs at corner A and B for
up-going rays transmitted from layer II or
IIa into layer I.

Figure 22 (a) Radiation characteristics for

group II diffracted rays, approaching

corner A from the left - see Fig. 22b.

(c) Radiation characteristics for

group II diffracted rays, approaching

corner B from the left - see Fig. 22d.

50%

50%
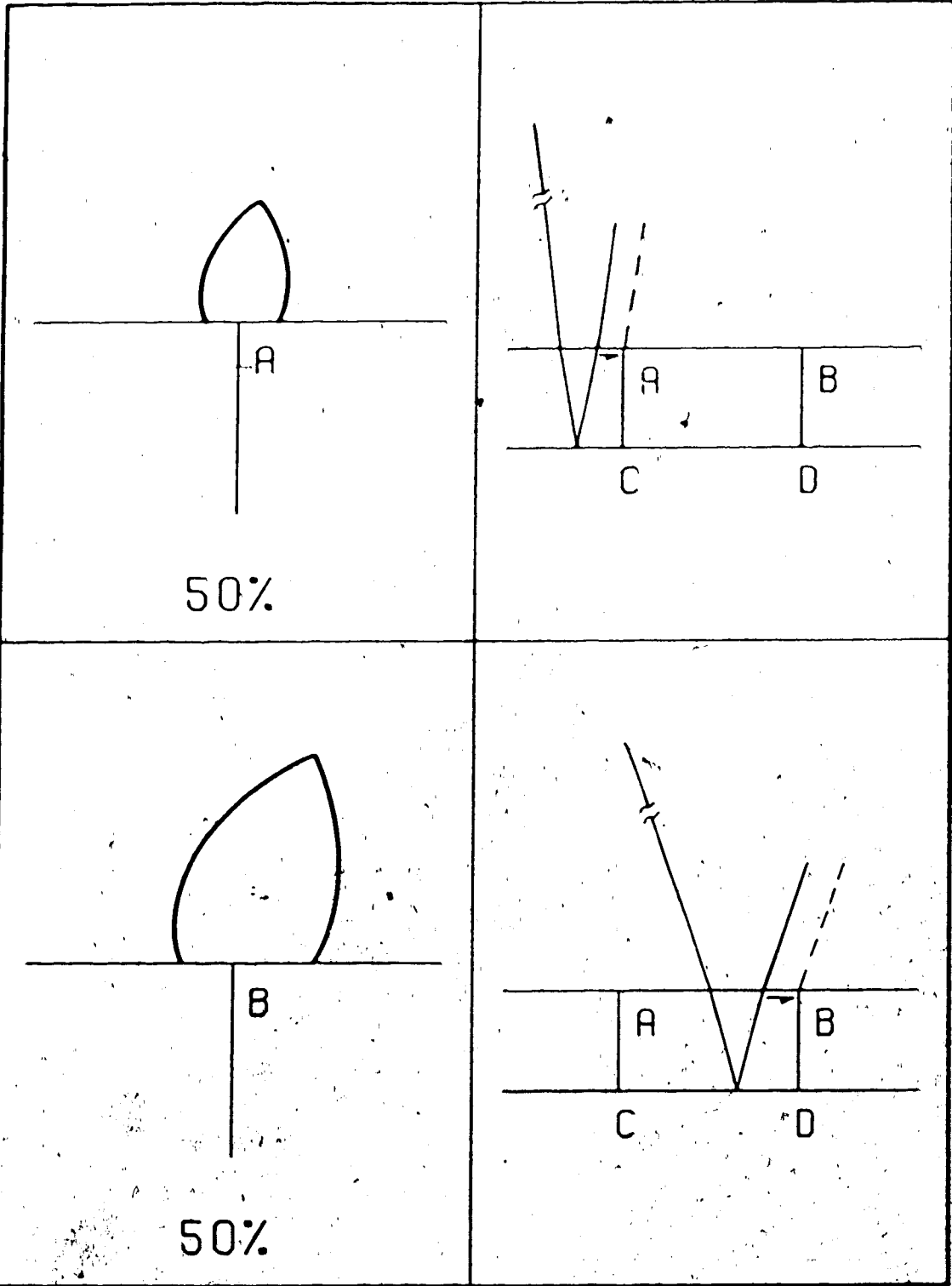
Figure 23 Synthetic seismograms for the diffracted

rays in group II:

- branch 7 corresponds to rays

in Fig. 21b, (diffracted from A)

-, branch 8 corresponds to rays

in Fig. 21d, (diffracted from B)
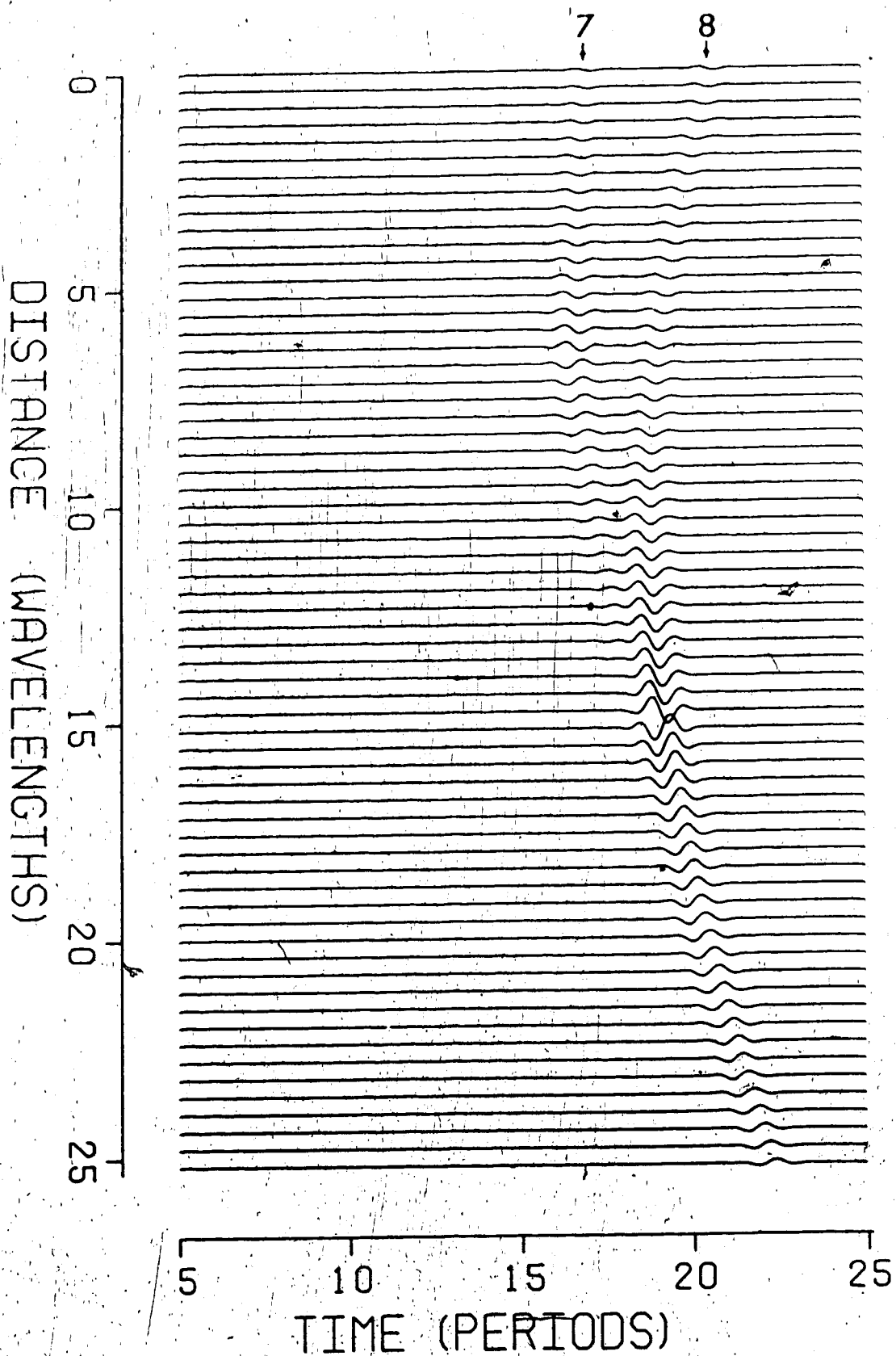
Fig. 24 shows a second type of diffraction associated
with geometric rays in group II. Notice that these
diffracted ray bundles have discontinuities. Diffraction
occurs at corners A and B with the shadow boundaries in
regions IIa and II. These diffracted rays then undergo a
reflection at the boundary L_2L_2' before being transmitted
back into layer I. Figs. 25a,c show the corresponding
radiation characteristics in the lower right corner at the
corners. Fig. 26 shows the synthetic seismograms of these
diffracted signals.

Both the 9 and 10 contributions suffer discontinuity at
the receivers directly above corners A and B respectively.
This is remedied by introducing a third type of diffracted
signal as depicted in Fig. 27. This bundle of rays takes on
the following ray path:

- the first diffraction occurs at say corner A,
  similar to any ray coded 9,
- the second segment is along AC,
- then each ray reflects upwards along CA, and
  suffers a second diffraction at corner A.

This is possible by applying the theory of analytic
continuation, with use of the Sokohtski-Plemelj formula,
Markushevich (1962). The corresponding synthetic seismograms

Figure 24 Ray diagram for the first batch of

diffracted rays in group II.

Diffraction occurs at Junctions A an B

for down-going rays transmitted from layer I

into layer II or IIa (the box).
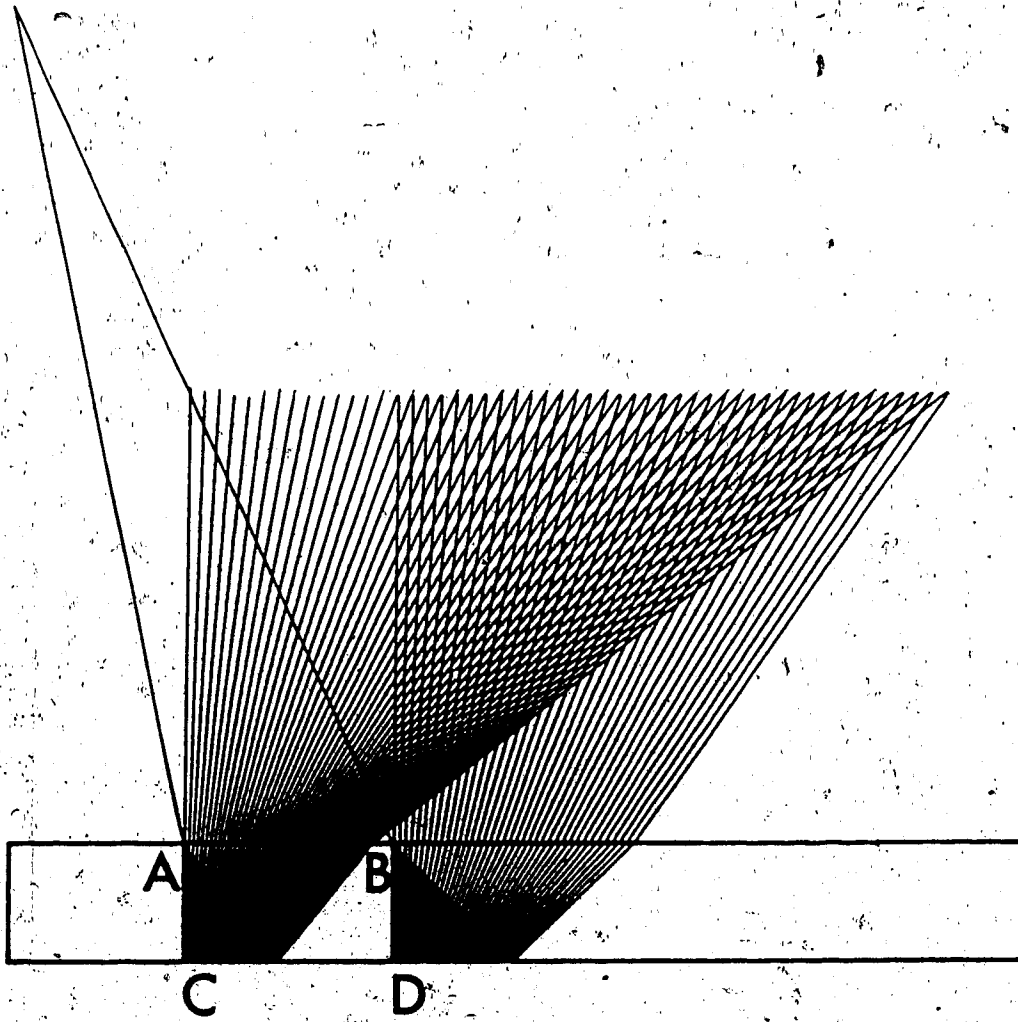
Figure 25 (a) Radiation characteristics for the second

batch of diffracted rays of group II.

The ray bundle approaches corner A from the

left, see Fig. 25b.

(c) Radiation characteristics for the second

batch of diffracted rays of group II.

The ray bundle approaches corner B from the

left - see Fig. 25d.

10%

10%
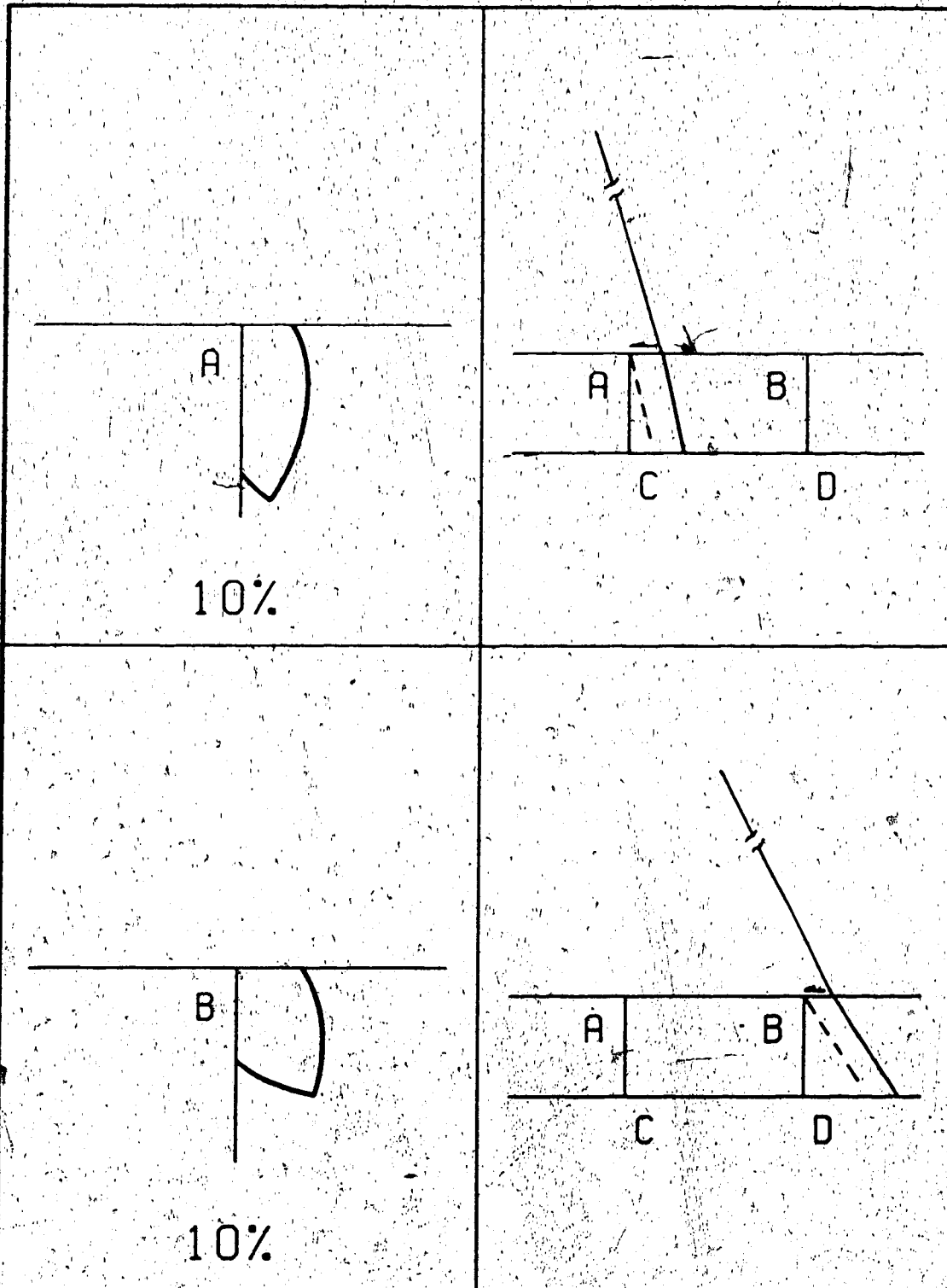
Figure 26 Synthetic seismograms for diffracted rays
of group II - see Fig. 24 for ray diagram.
Contribution 9 and 10 are diffracted at
corners A and B, respectively.
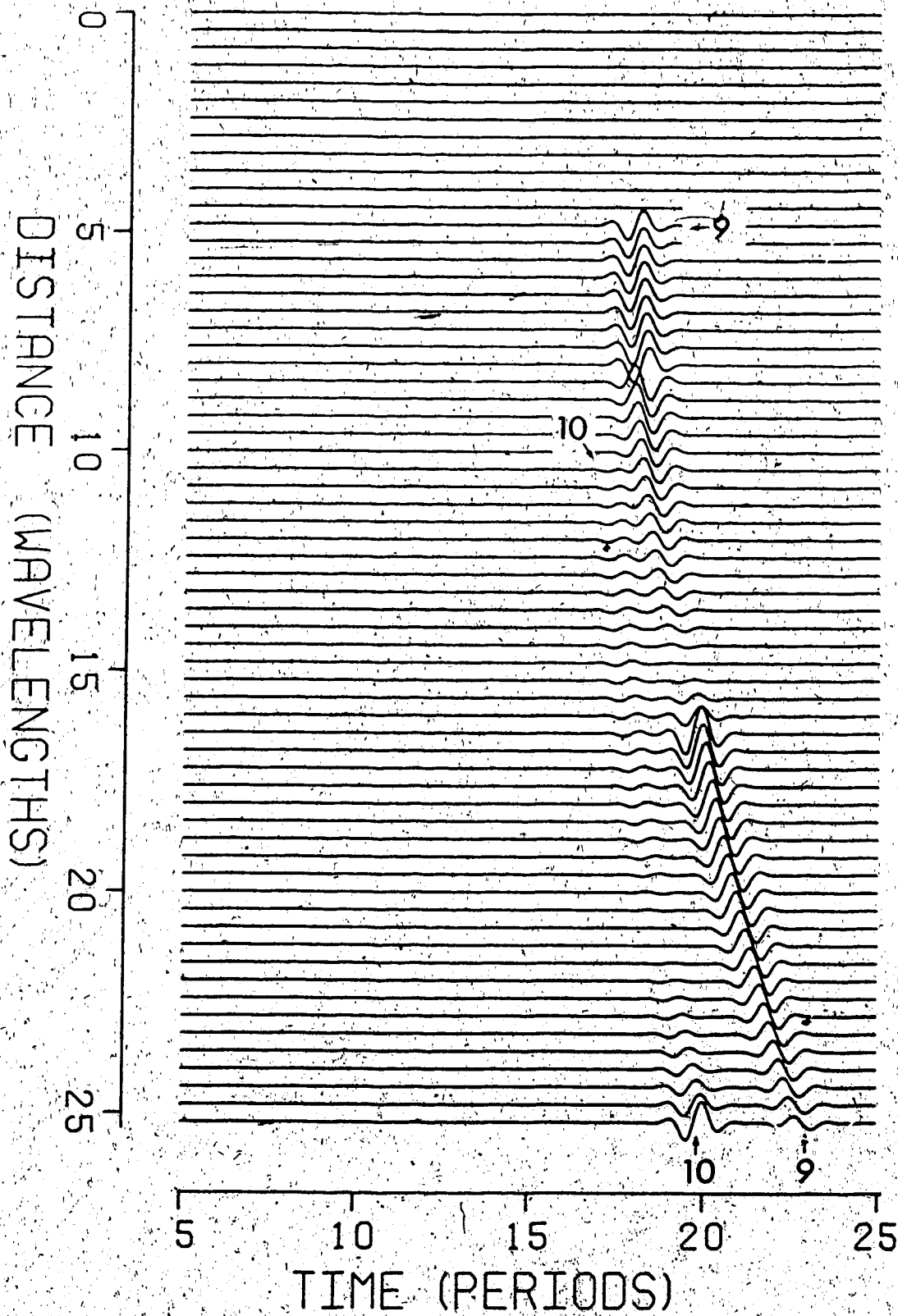
Figure 27 Ray diagram for diffracted contribution
supplemental to those in Fig. 24.
Diffraction occurs at junctions A (or B).
The ray path continues along the line AC
(or BD), before being reflected along CA
(or DB). Then it suffers a second diffraction
at corner A (or B), and upon transmission,
back into layer I.
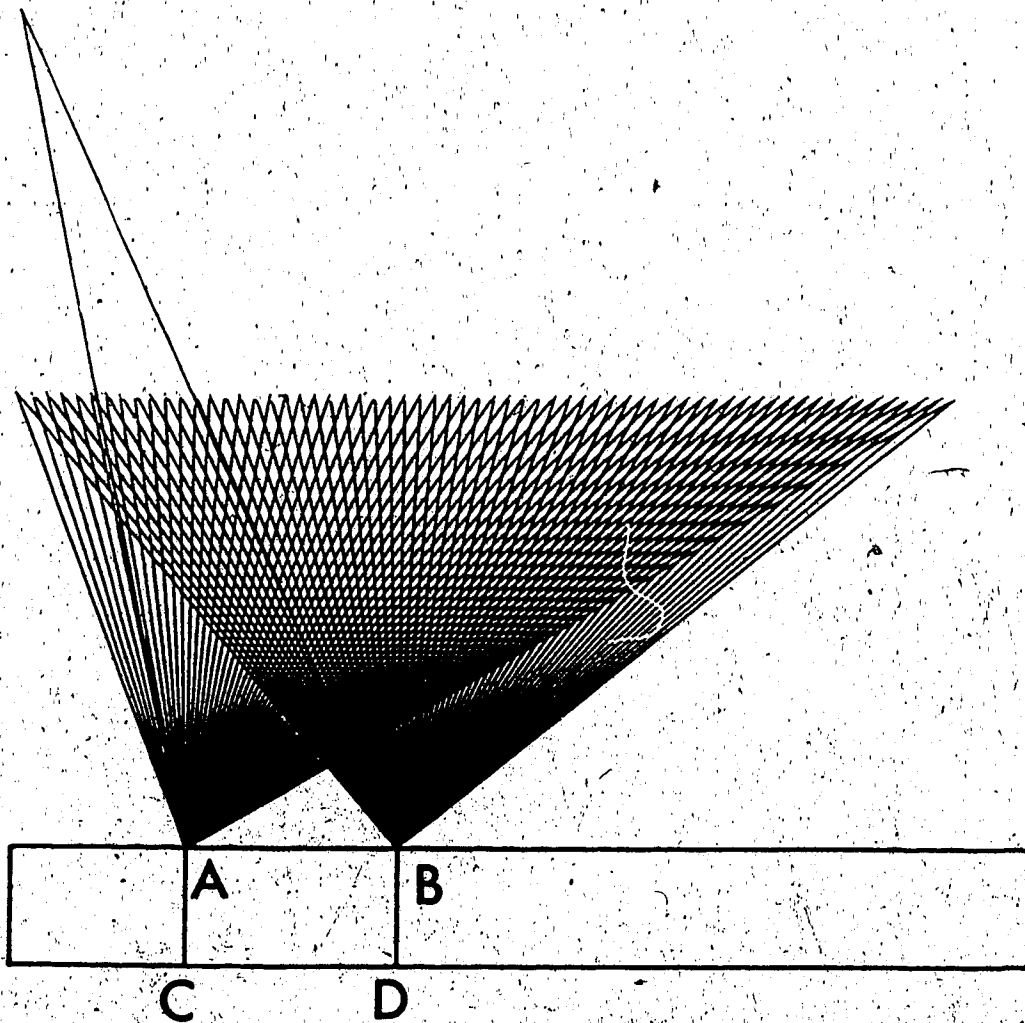
are shown in Fig. 28, code 11 (related to corner A) and 12 (related to corner B). Contribution 12 is comparatively small, and its position will be neglected in the future.

Now, all the diffracted contributions code 7 to 12 are added to give Fig. 29. Note that the code and arrow (e.g. 9) are used as the identification of the particular type of signals, and do not necessary indicate the onset of the wavelet in general.

The total contribution from all the rays in group II is shown in Fig. 30. The diffraction at corner A into the box is seen to dominate this group. Upon re-examination of the geometrical contributions 4, 5 and 6, the comparison demonstrates the obvious shortcoming of the basic ray theory.

4.6   Group III -- consisting of rays with 5 ray segments, reflected from the second interface L_2L_2' and one of the two vertical sides of the box, i.e. AC or BD

Fig. 31 shows the 5-segmented ray paths of the geometric arrivals in group III. There are two shadow

Figure 28 Synthetic seismograms for a twice diffracted

contribution as described in Fig. 27:

- contribution 11 from corner A

- contribution 12 from corner B.

DISTANCE (WAVELENGTHS)

TIME (PERIODS)
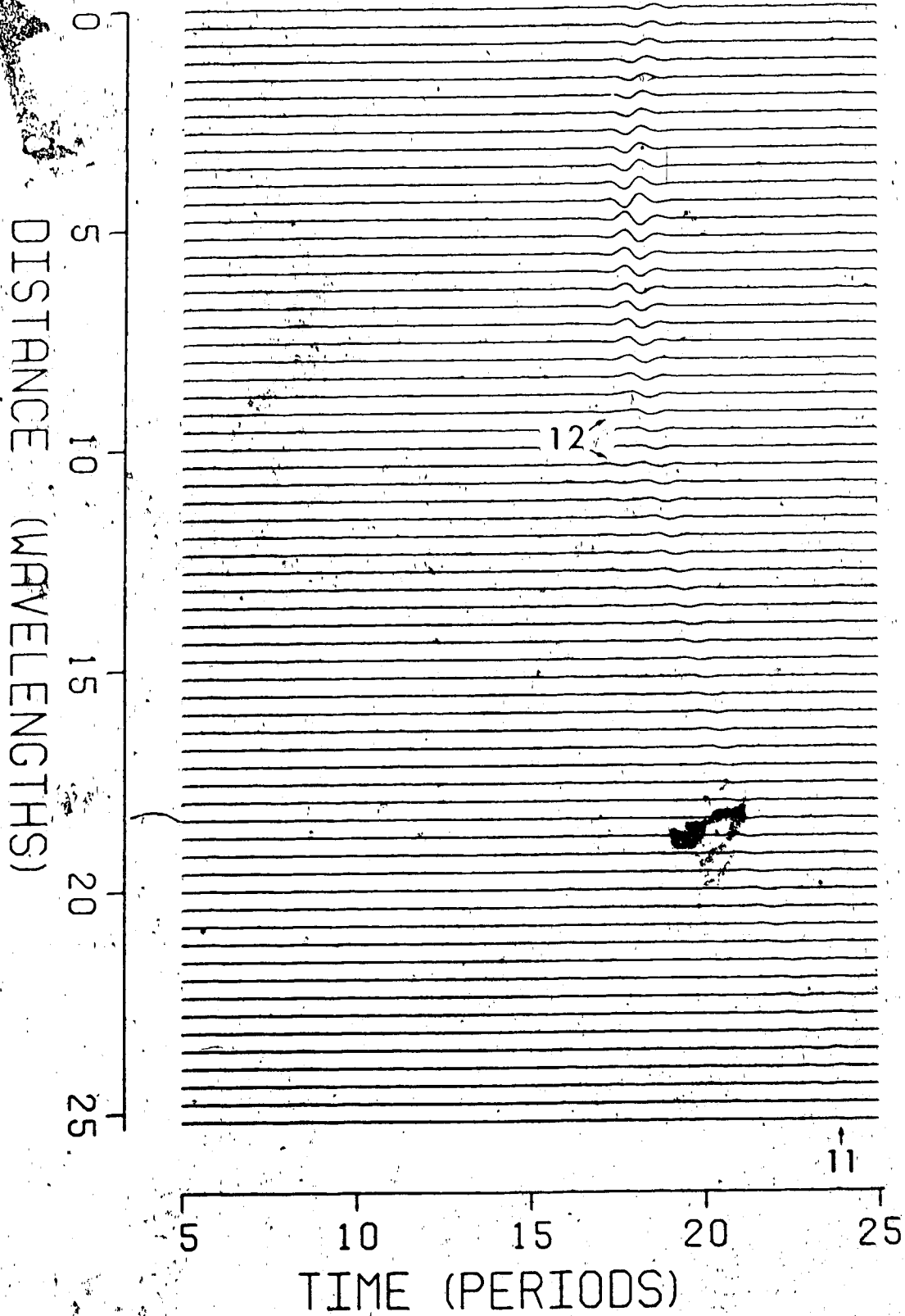
Figure 29 Sum of contributions 7-12.

(all diffracted rays of group II)
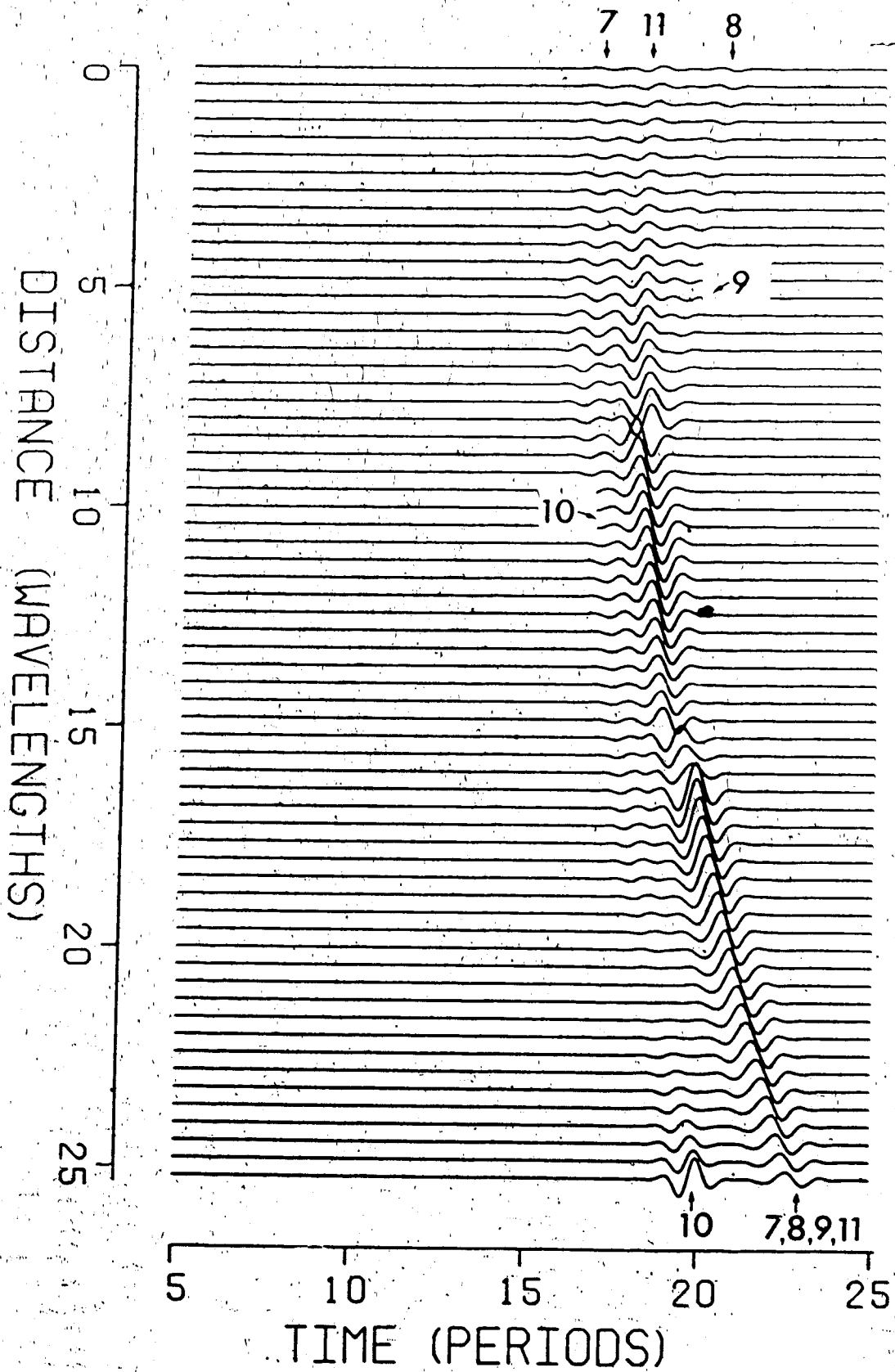
Figure 30 Sum of contributions pertaining to
all rays (geometrical and diffracted)
in group II.
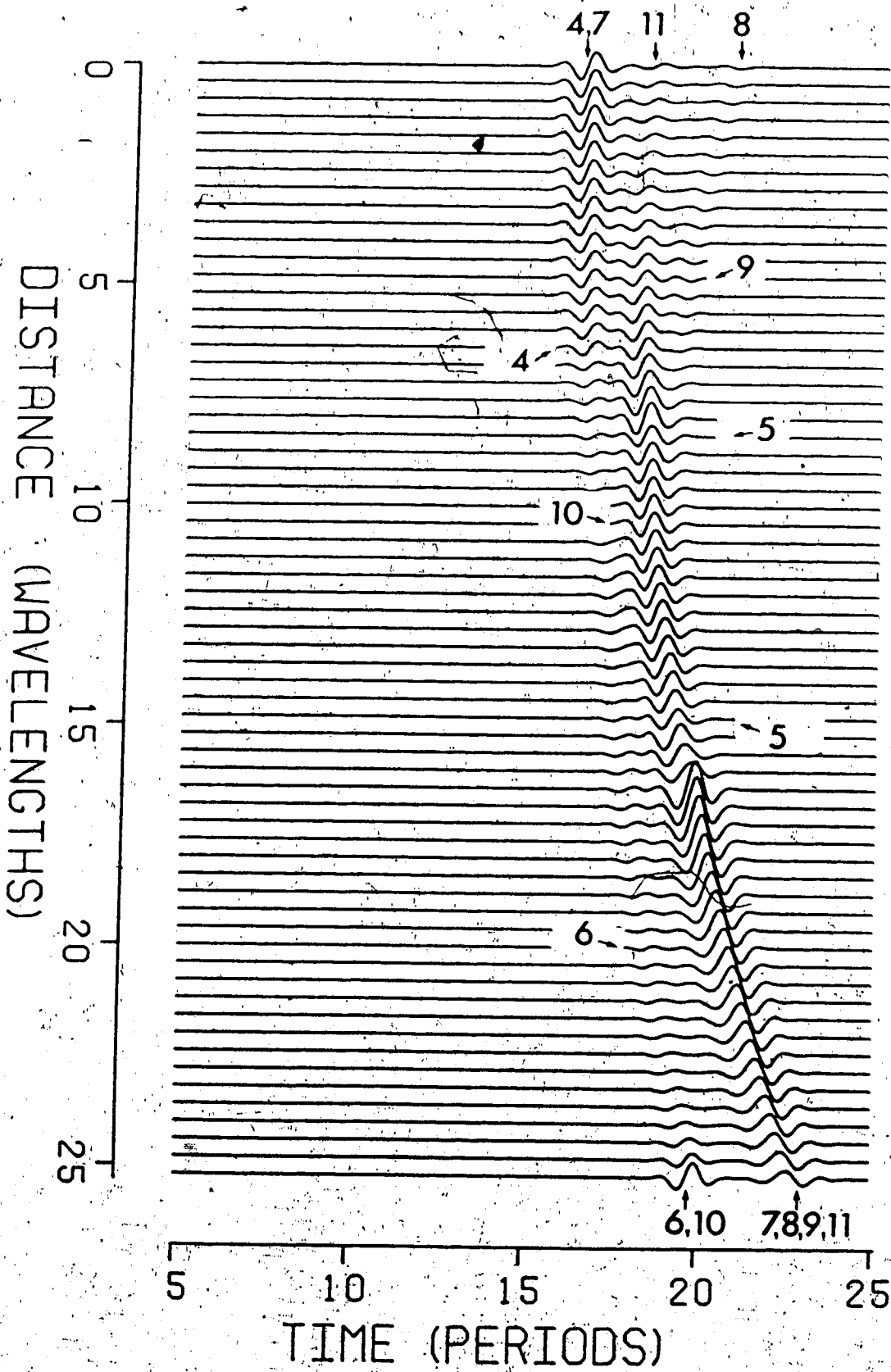
boundaries associated with each bundle, similar to one case
discussed in section 4.5 (rays from group II). The
corresponding synthetic seismograms are shown in Fig. 32.
Fig. 33 shows a closely related 5-segmented ray paths
geometric arrivals, differing from the previous two only in
the reversed reflection sequence. These ray bundles are
classified group III. The corresponding synthetic
seismograms are shown in Fig. 34. Upon the addition of
Figs. 32 and 34, we obtained the total contributions due to
geometric rays in group III. The appearance of continuity of
13 and 15 (and that of 14 and 16) suggests some merits of
this grouping.

Figs. 36b,d show the shadow boundaries and the approach
of the last geometric rays towards them. The dominating
radiation characteristic modulus due to corner B in Fig. 36c
explains the importance of contribution 18 as shown in
Fig. 37. Figs. 38b,d show the shadow boundaries for the
second part of the geometrical rays in group III. Again the
corresponding radiation characteristics shows a larger
contribution from corner B, labelled 20 in Fig. 39. Note
that similar to contributions 9 and 10 in group II, each of
19 and 20 needs a supplemental contribution of twice
diffracted rays to avoid a discontinuity of its own. These
are labelled 21 and 22 in Fig. 40.
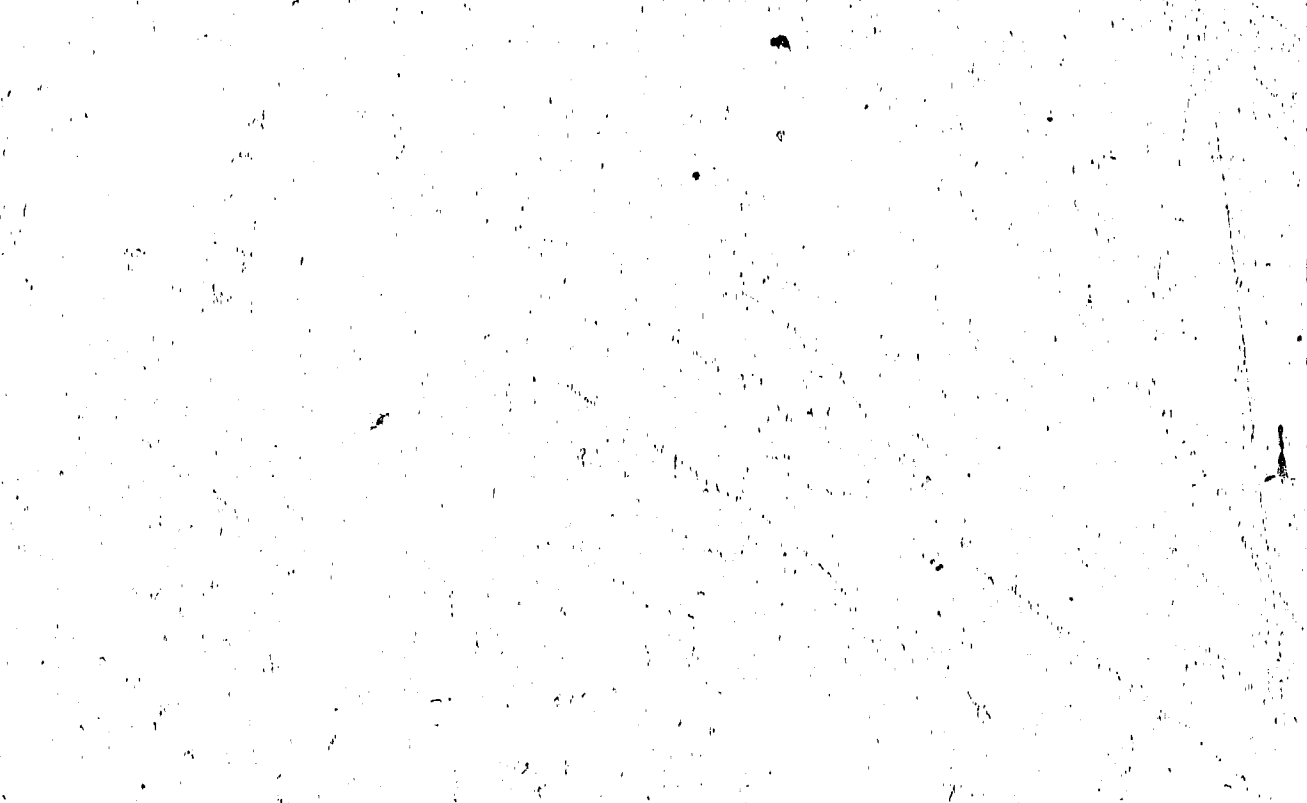
Figure 31 Ray diagram for the first part of

geometrical rays in group III

A ray will travel from the source, transmits

into layer II (or IIa the box), reflects from

the interface L_2L_2', travels upwards, reflects

to the left at AC (or BD), before being

finally transmitted back into layer I.
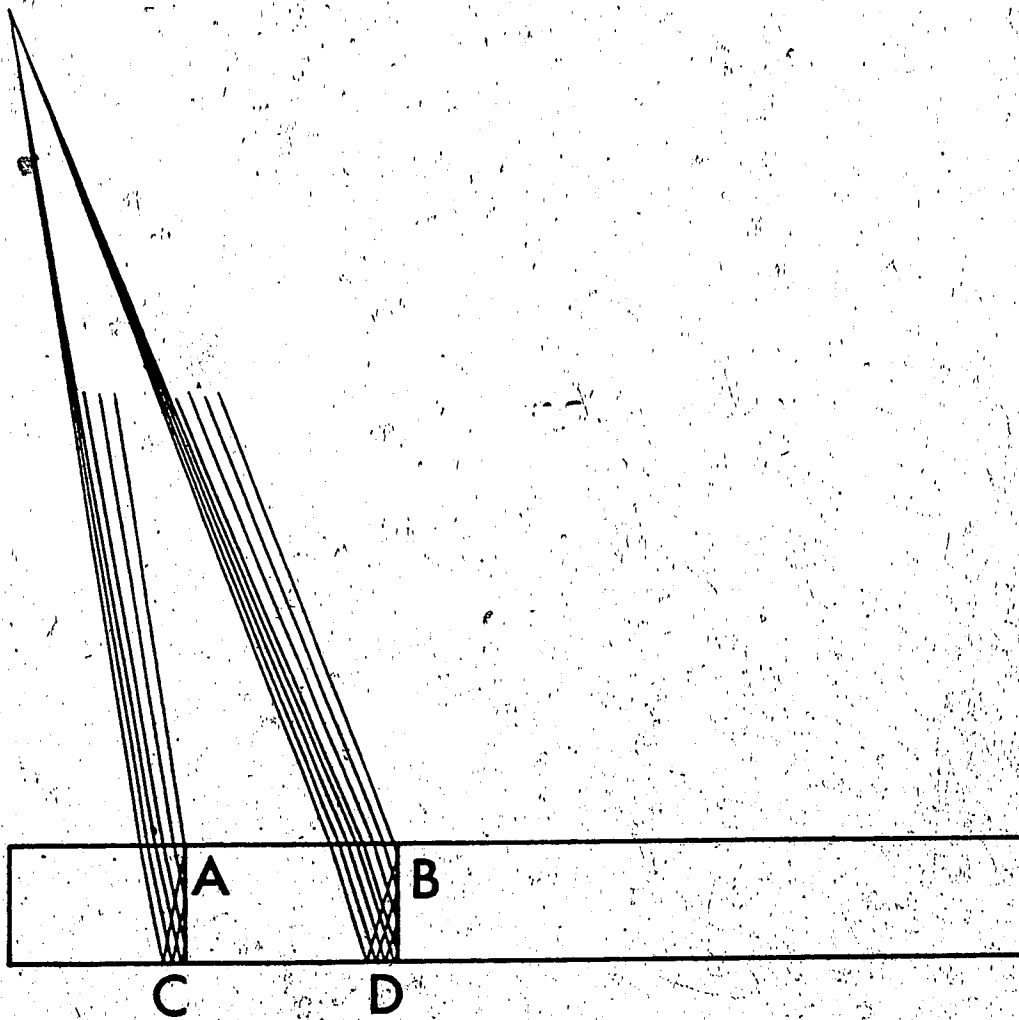
Figure 32   Synthetic seismograms for the first

part of geometric rays in group III

see Fig. 31.

The contributions 13 and 14 correspond to the

second primaries reflected from the vertical

sides of the box AC, and BD, respectively.
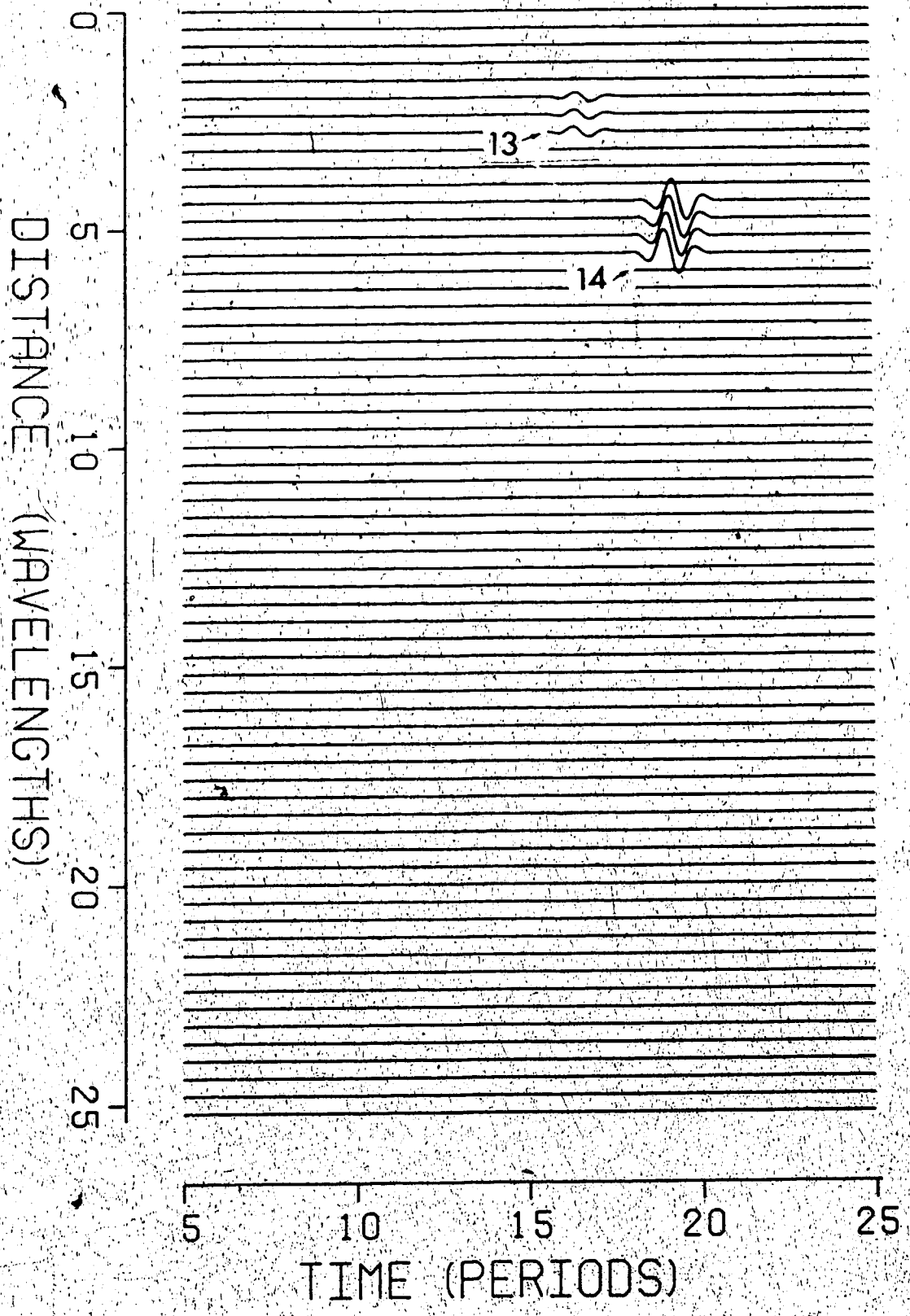
Figure 33 Ray diagram for the second part of
geometrical rays in group III
The rays will travel from the source, transmit
into layer II (or IIa, the box), reflect from
the interface AC (or BD), travel downwards
and reflect at boundary $L_2 L_2'$, before
travelling upwards and transmitting back into
layer I.
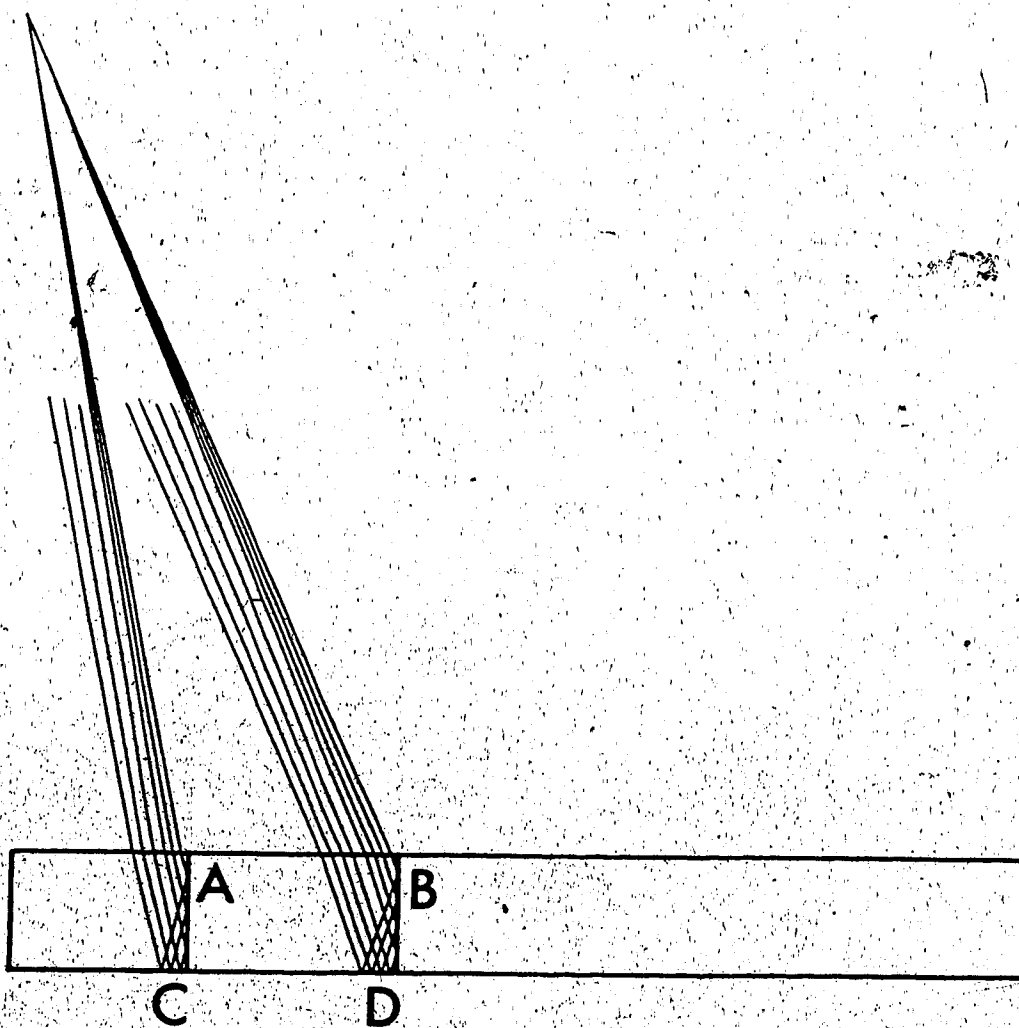
Figure 34 Synthetic seismograms for the second

part of geometric rays in group III

see Fig. 33.

Contributions 15 and 16 are due to the first

and second bundles of rays in Fig. 33

reflected from the vertical side of the box

AC and BD, respectively.

DISTANCE (WAVELENGTHS)

TIME (PERIODS)
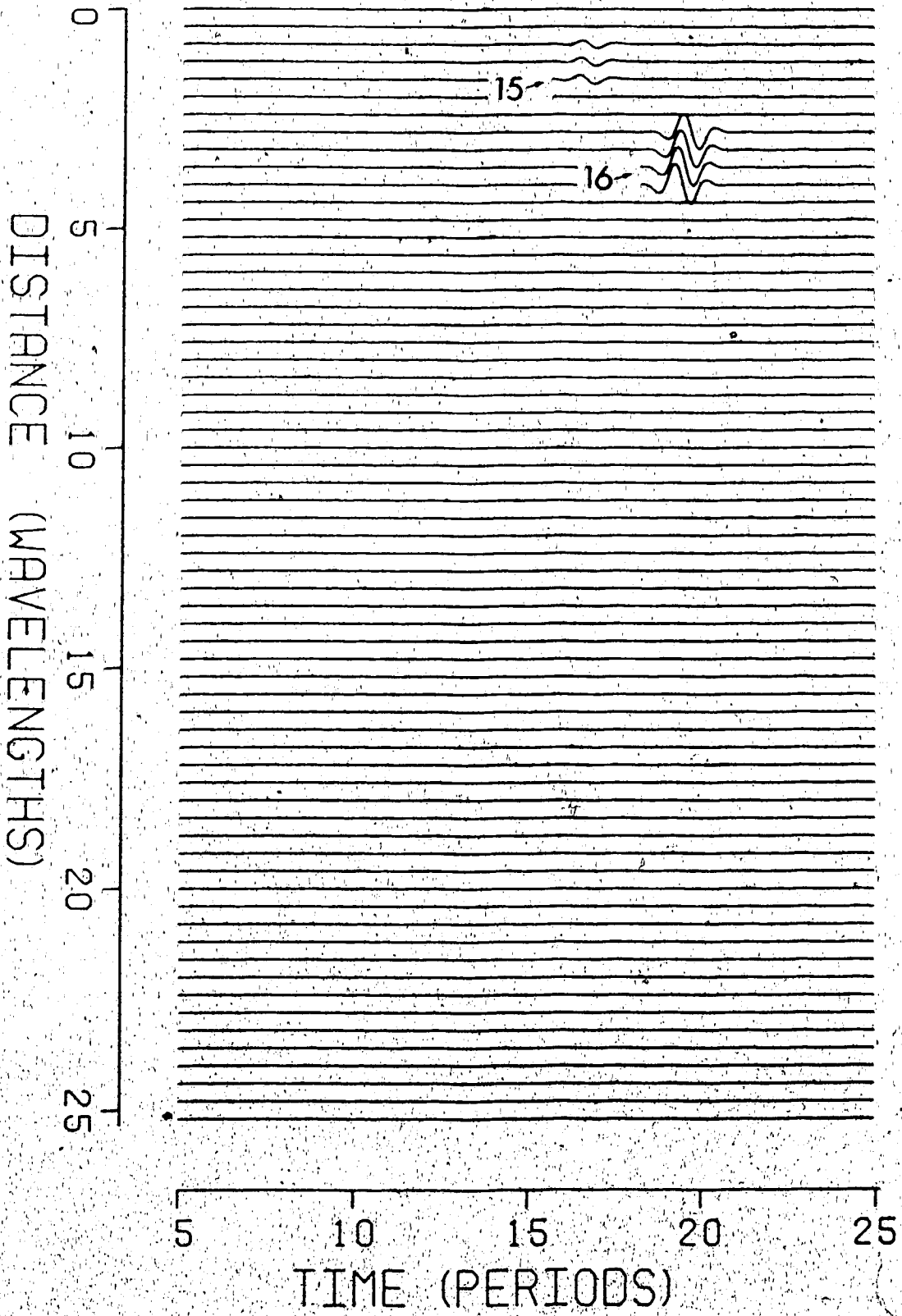
Figure 35   Sum of contributions 13-16.

Synthetic seismograms due to all four bundles

of geometrical rays in group III.

N.B. Contributions 13 in Fig. 32 and 15 in

Fig. 34 represent the same travel branch of

rays reflected from the vertical side AC of

the box, even though it is due to 2 different

bundles of rays with reverse reflection

sequences.

The same is true for contributions 14 and 16

due to the rays reflected from BD.
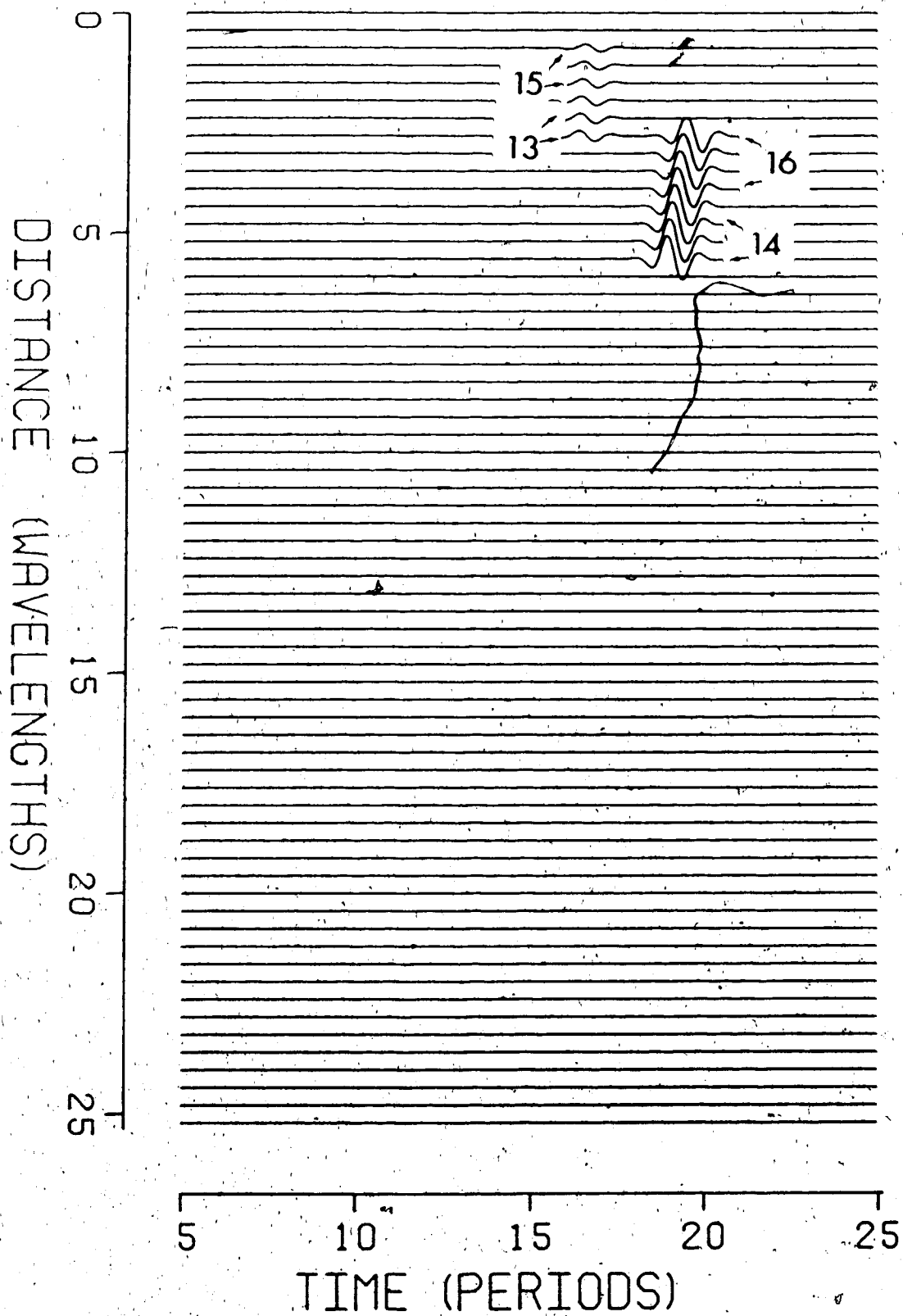
Figure 36 (a) Radiation characteristics for the
diffracted rays due to the first bundle of the
first part of geometric rays in group III
(b) shows the corresponding shadow boundary
due to corner A.
(c) Radiation characteristics for the
diffracted rays due to the second bundle of the
first part of geometric rays in group III
(d) shows the corresponding shadow boundary
due to corner B.

50%

50%
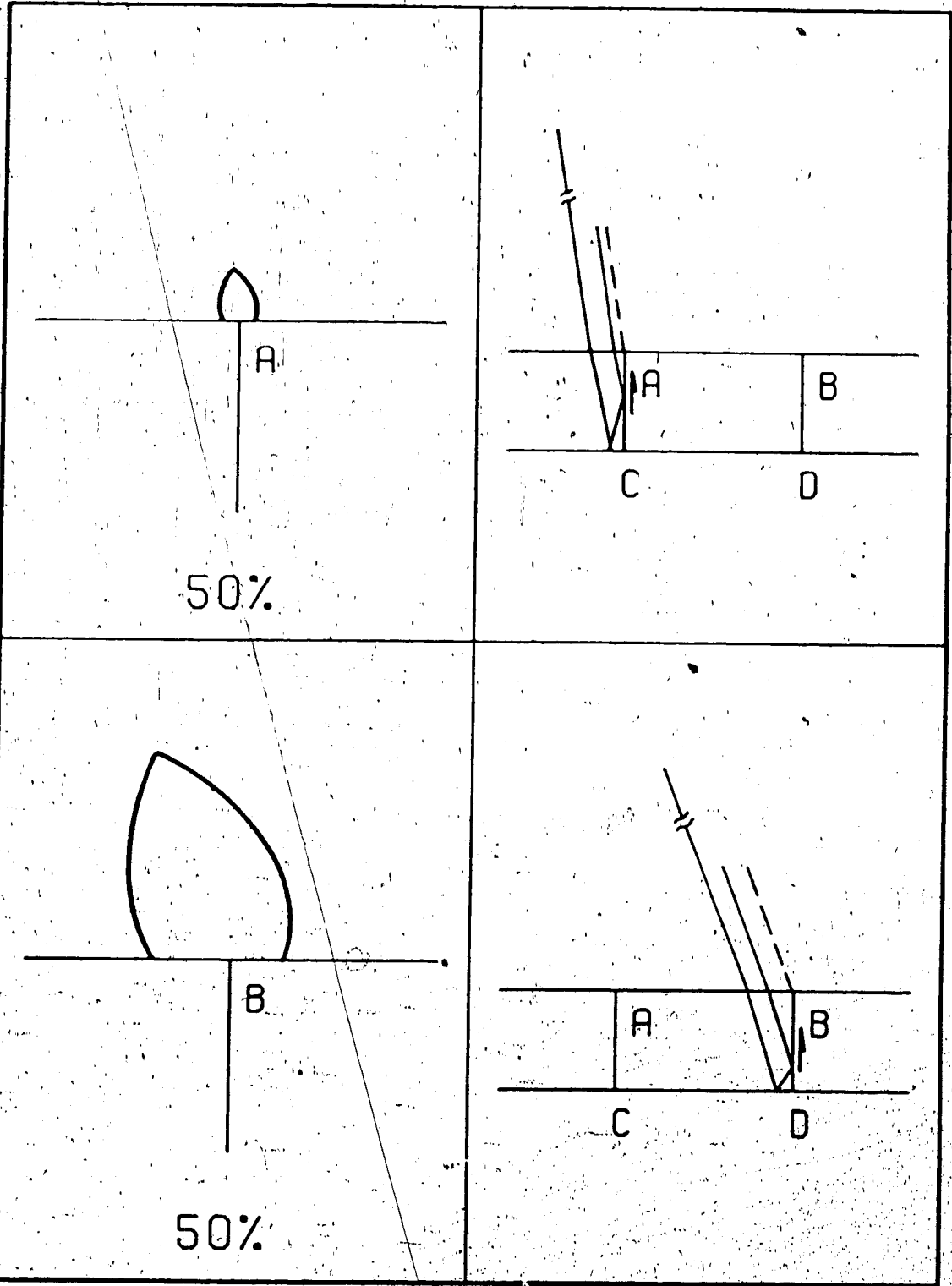
Figure 37 Synthetic seismograms corresponding

to diffracted arrivals in Fig. 36:

contribution 17 is due to corner A, while

contribution 18 is due to corner B.
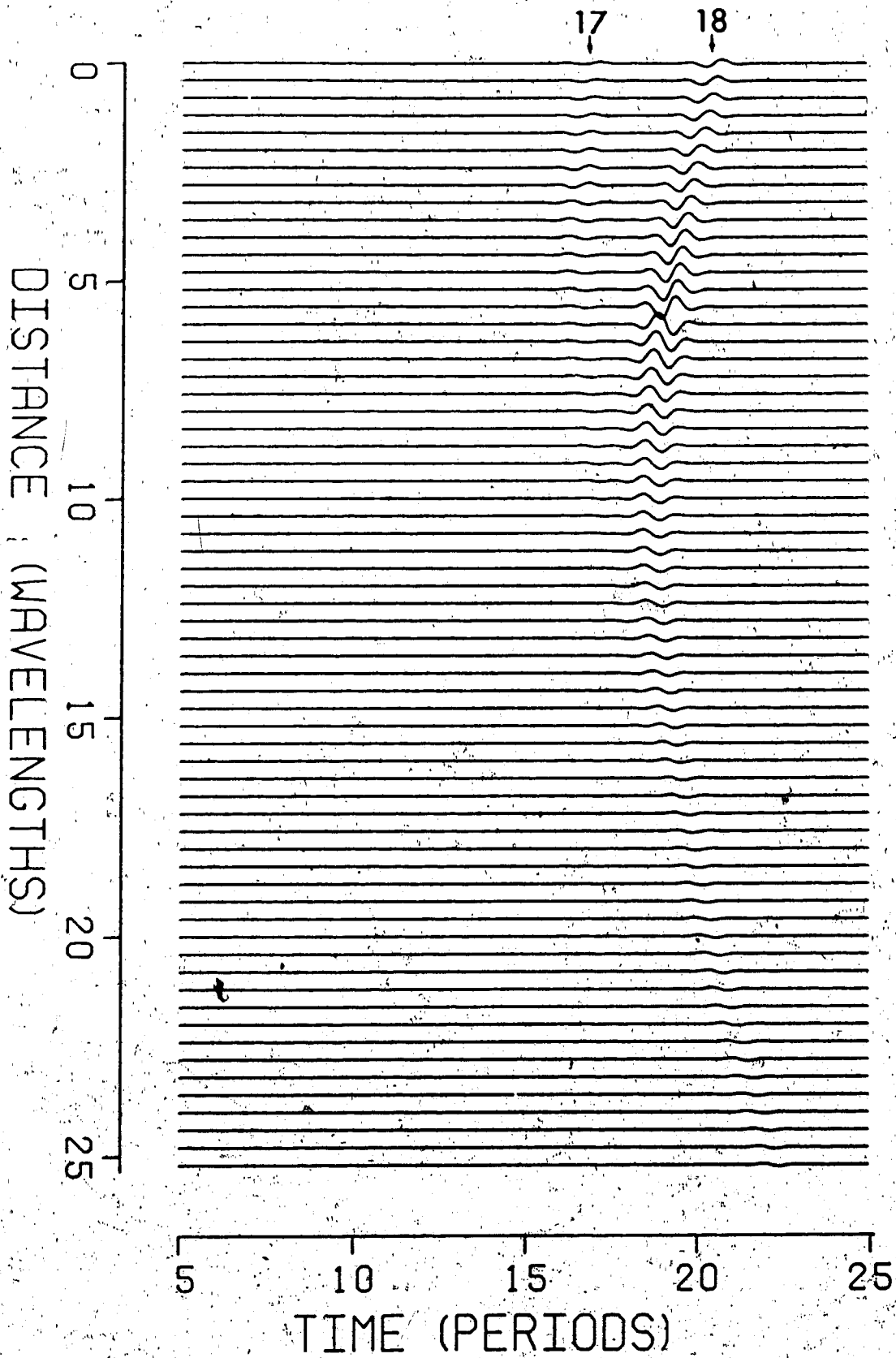
Figure 38 (a) Radiation characteristics for the

diffracted rays due to the first bundle of the

second part of geometric rays in group III

(b) shows the corresponding shadow boundary

due to corner A.

(c) Radiation characteristics for the

diffracted rays due to the second bundle of the

second part of geometric rays in gruop III

(d) shows the corresponding shadow boundary

due to corner B.

50%

50%

Figure 39 Synthetic seismograms corresponding

   to diffracted arrivals in Fig. 38:

   contribution 19 is due to corner A, while

   contribution 20 is due to corner B.

DISTANCE (WAVELENGTHS)

TIME (PERIODS)
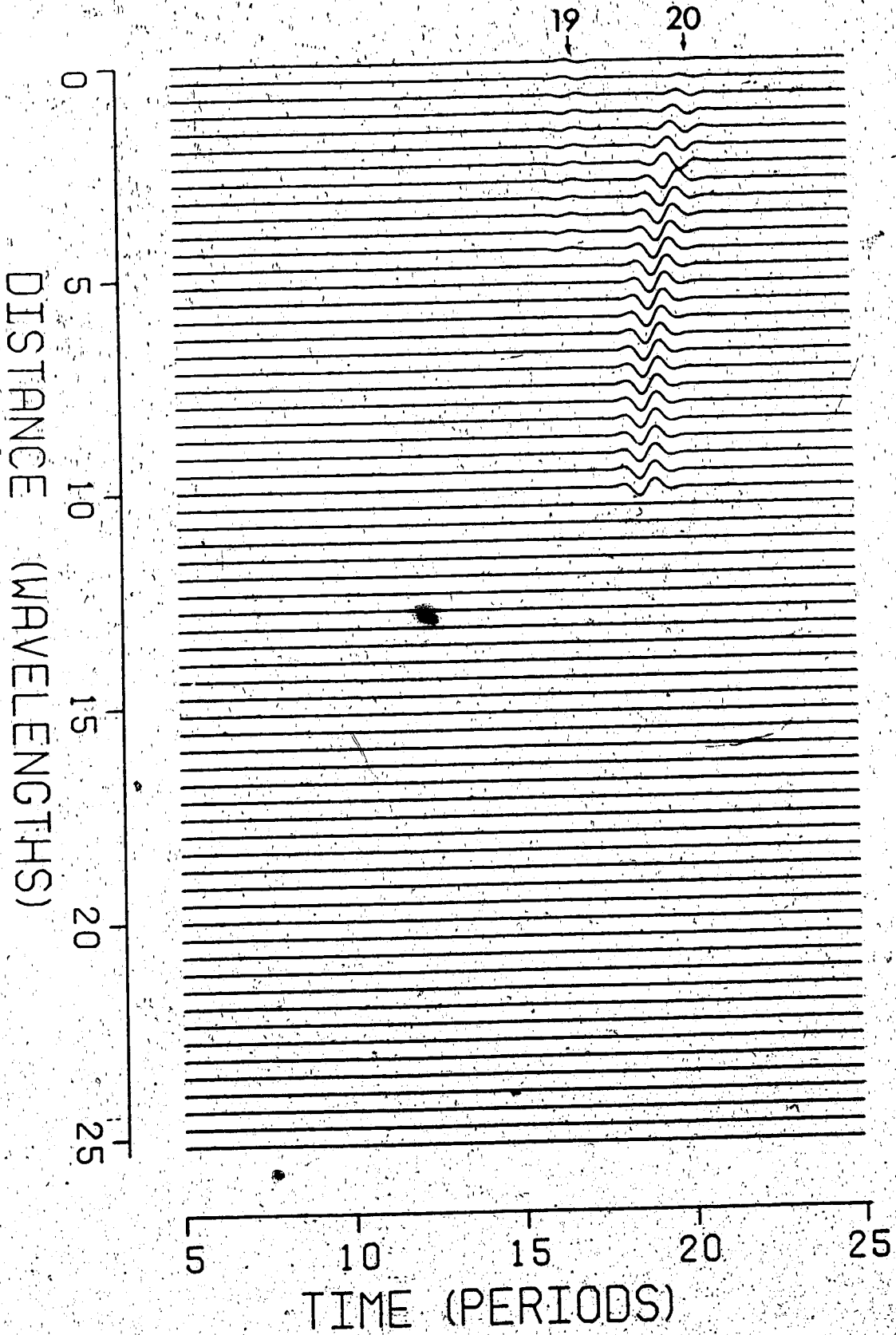
The total diffracted contributions 17 - 22 are shown in Fig. 41. Adding this to the synthetic seismograms of the geometric arrivals gives the total wave field of group III, where corner B (Fig. 35) is given the credit of major response.

4.7   Group IV -- consisting of rays with 6 segments, once reflected from the bottom of the box and crossed both of its vertical sides.

Fig. 43 shows the geometric rays of group IV. It is relatively small bundle of 6-segmented rays traversing through 4 different zones. It turns out that only two receivers pick up this type of event, coded 23 in Fig. 44. Nevertheless, the strength of this arrival necessitates its inclusion into our ray synthetic seismograms.

The diffracted signals in this group are more involved. Figs. 45 and 46 show the first two types, with the corresponding radiation characteristics and shadow boundaries shown in Fig. 47. The respective synthetic seismograms coded 24 and 25 are shown in Figs. 48 and 49. Notice that event 25 has two abrupt terminations indicating the presence of

Figure 40 Synthetic seismograms supplemental

to diffracted arrivals in Fig. 38,

corresponding to twice diffracted rays

A/B (contribution 21/22)
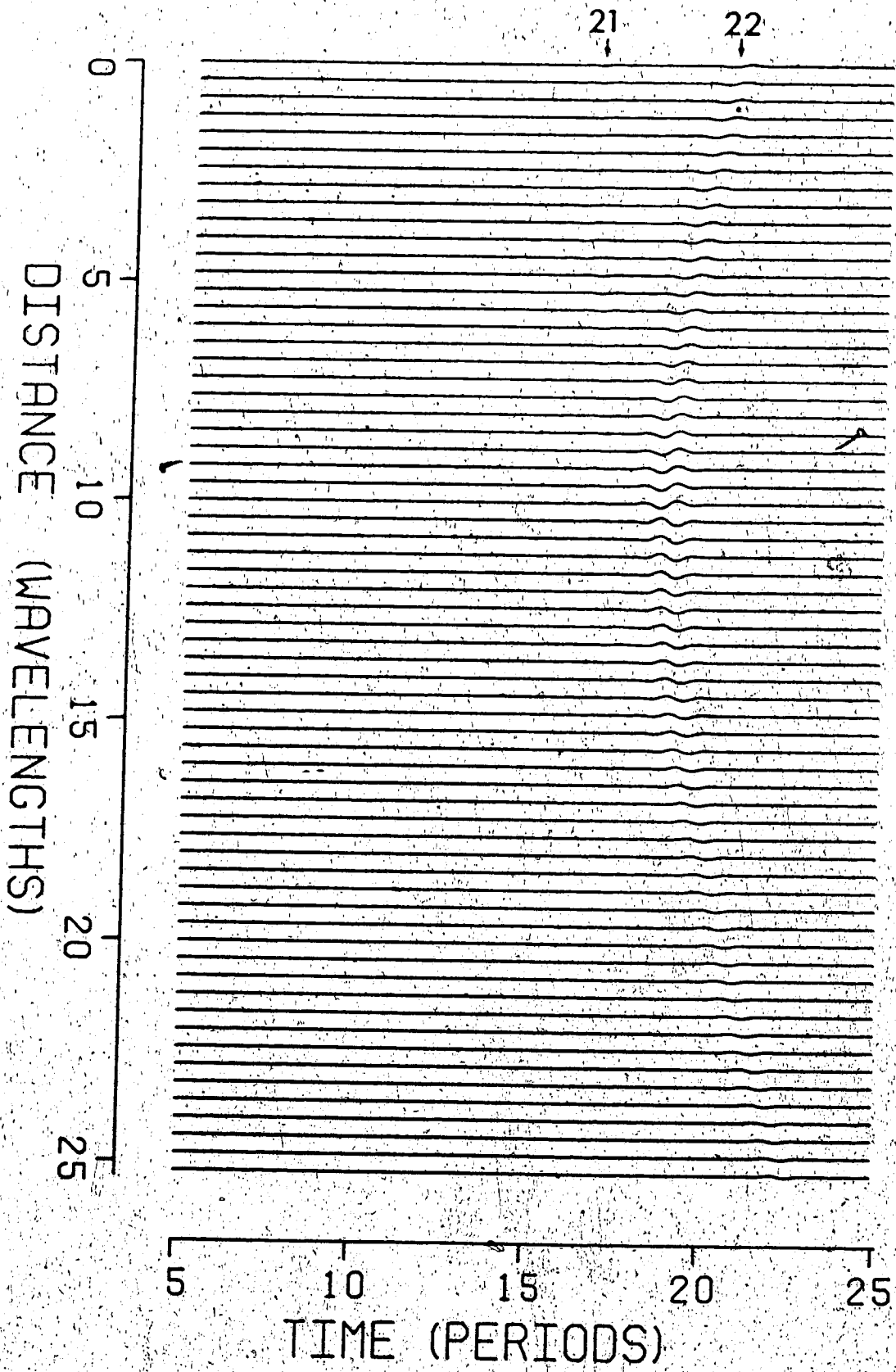
Figure 41 Sum of diffraction contributions in
group III (17-22).
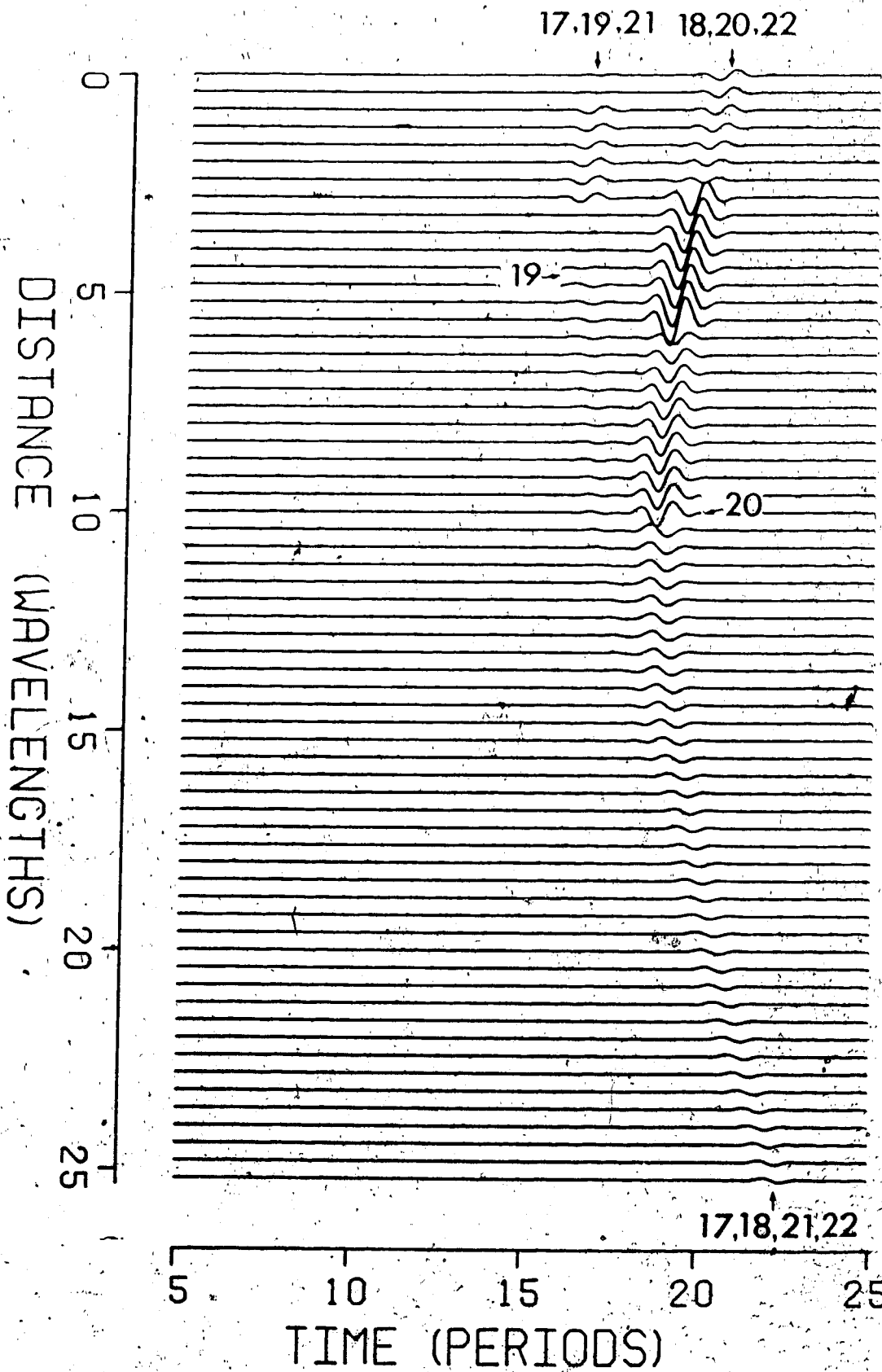
Figure 42 Sum of contributions in group III.

(See Figs. 35 and 41 for comparison).
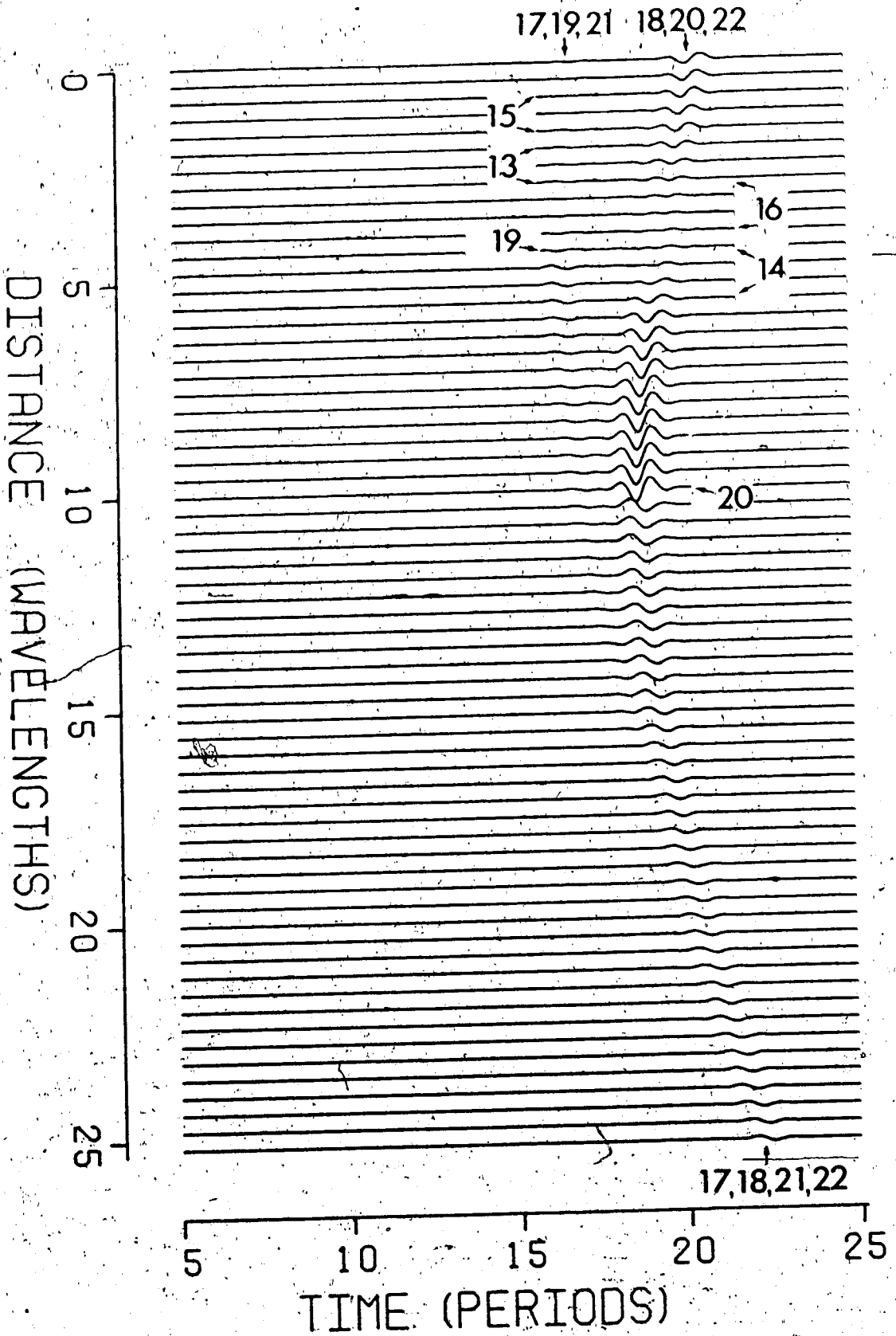
Figure 43 Ray diagram for geometric rays in
group IV.
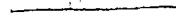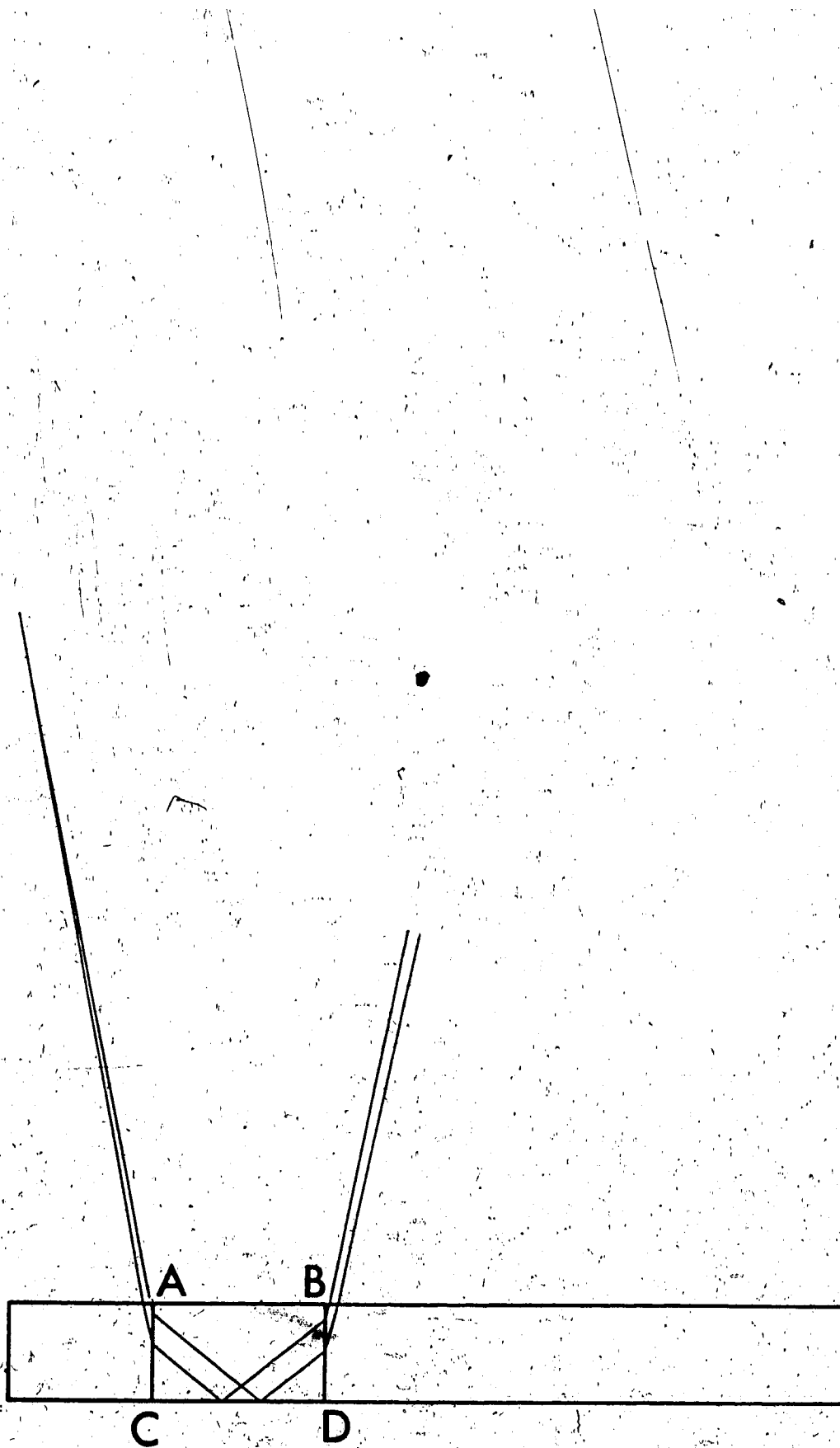
Figure 44 Synthetic seismograms for geometric

rays (see Fig. 43) in group IV.
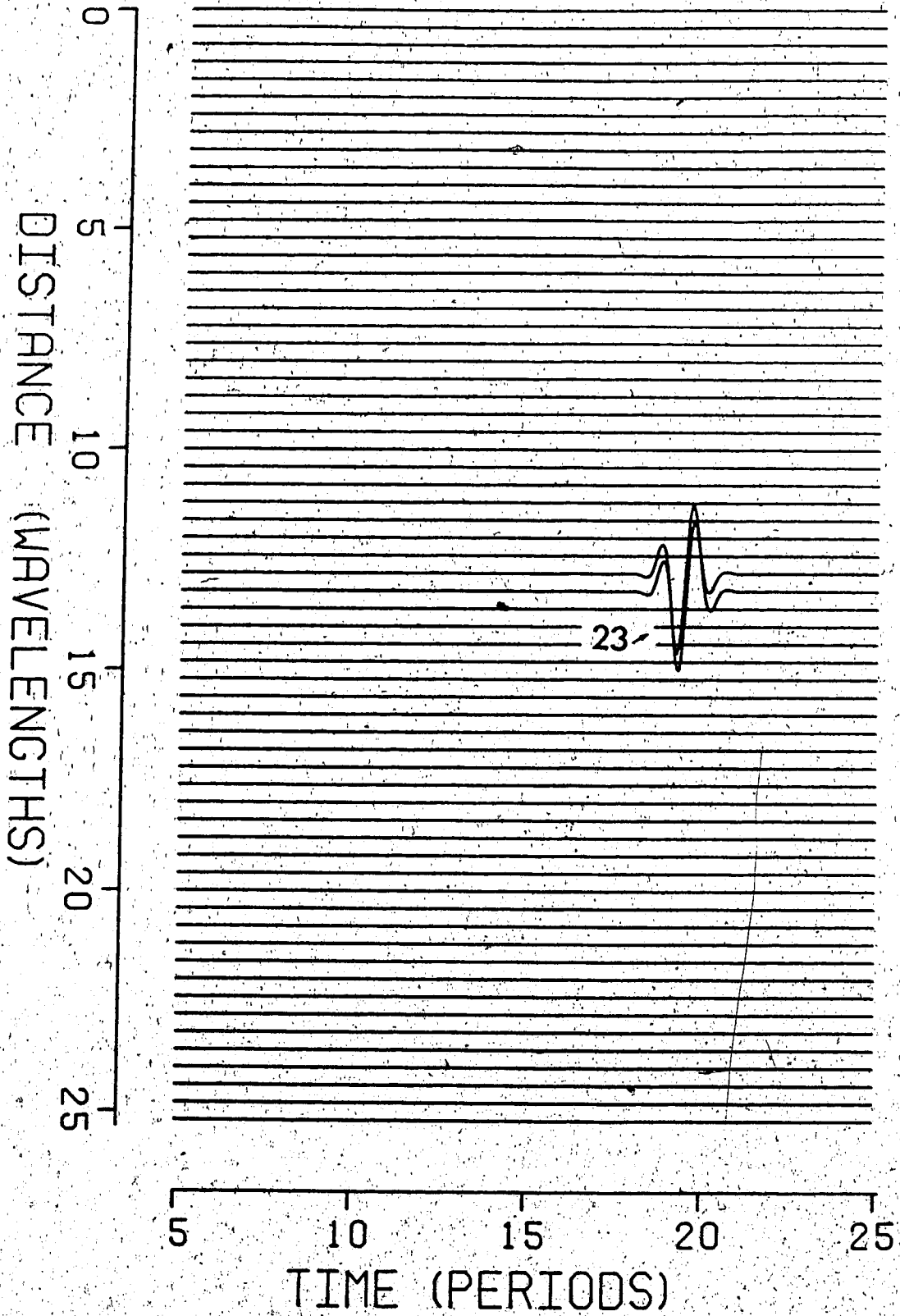
Figure 45 Ray diagram for the first part of

diffracted rays in group IV.

Diffraction occurs at corner B.
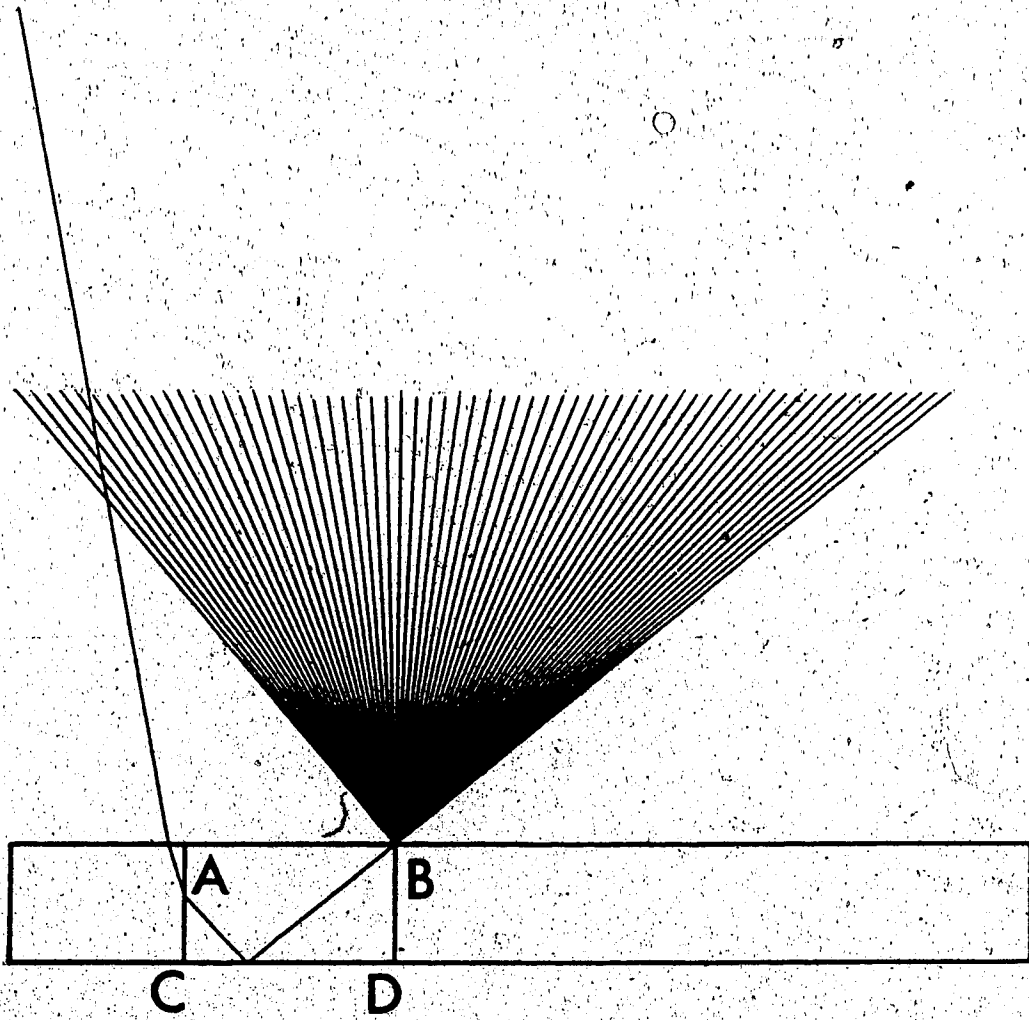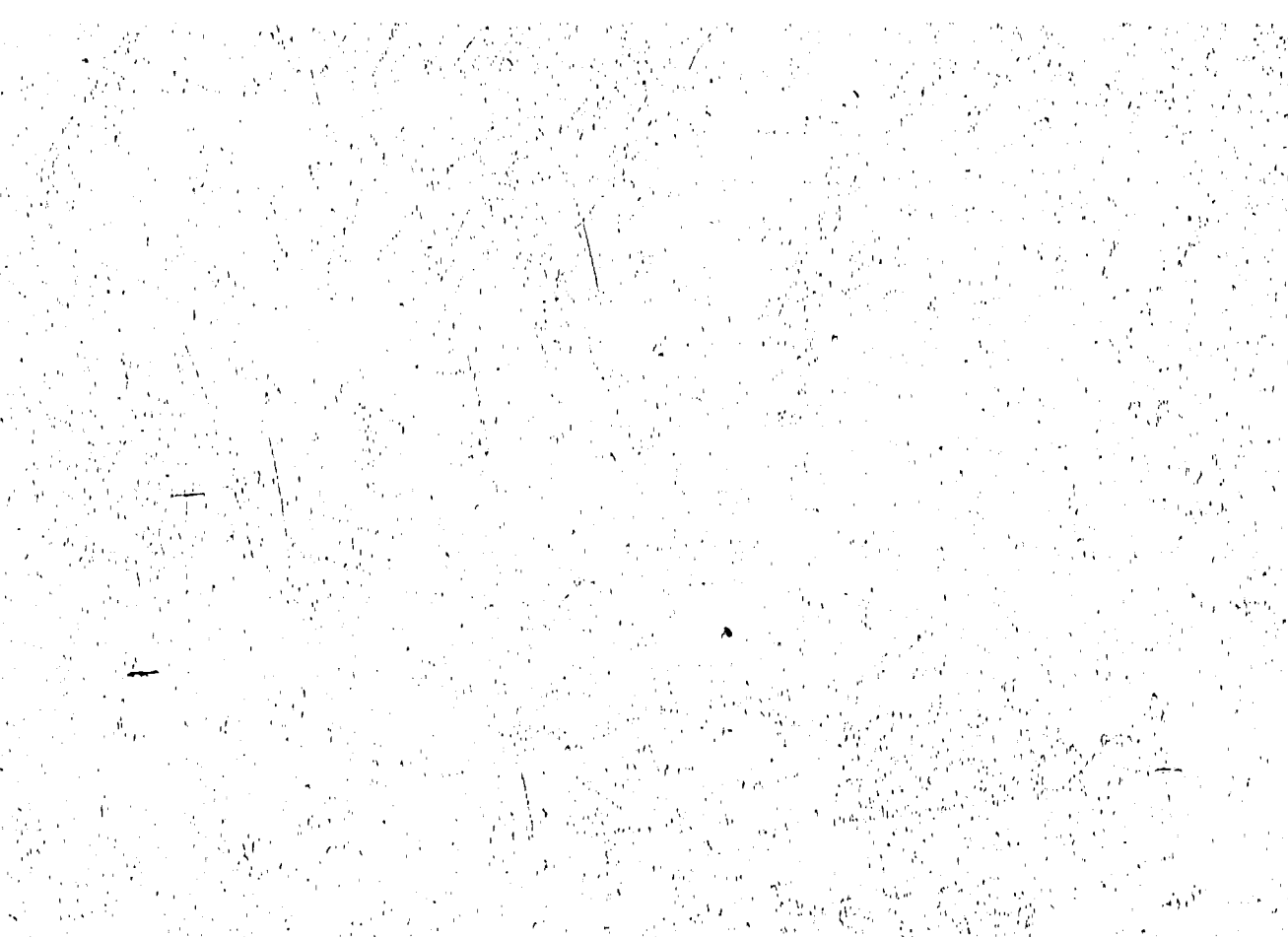
Figure 46 Ray diagram for the second part of
diffracted rays in group IV.
Diffraction occurs at corner A.
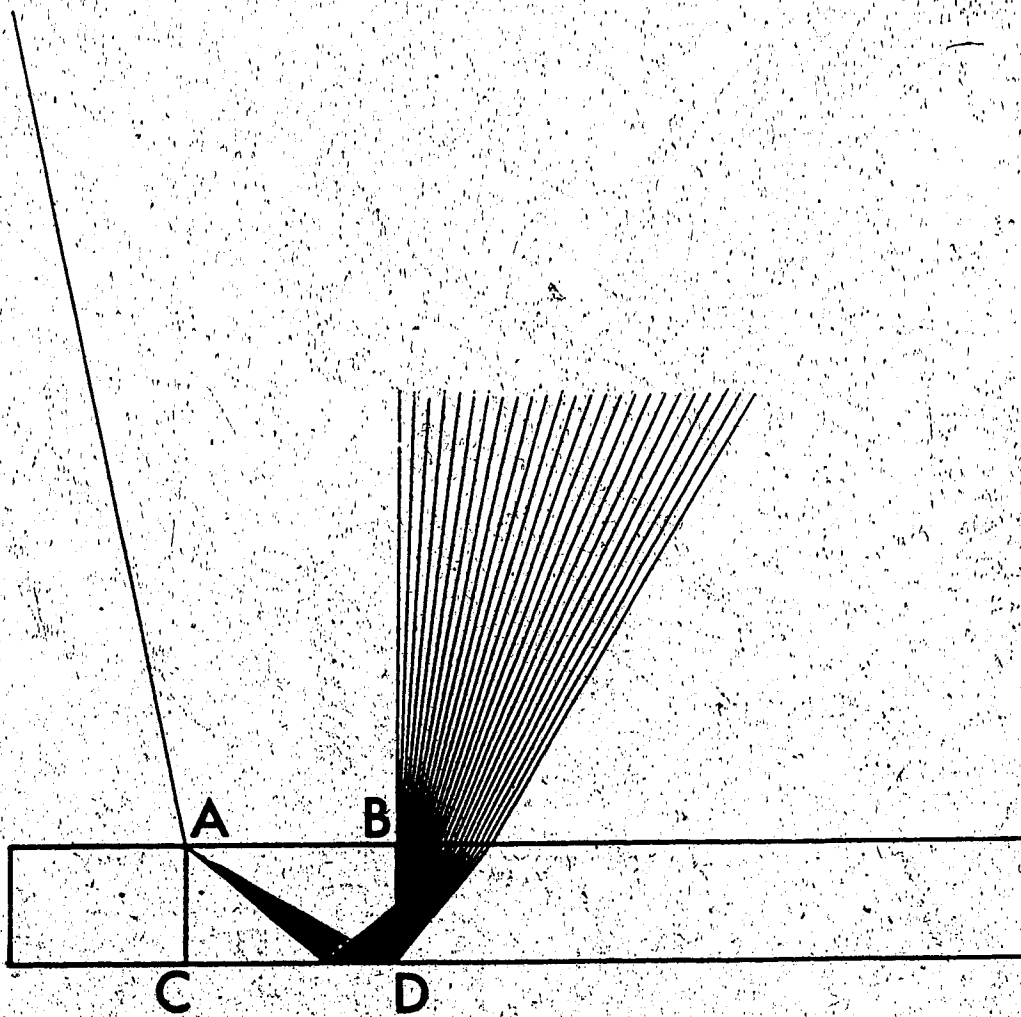
shadow boundaries. In view of the relatively small amplitude received at the distance of approximately 10.0 w there will be not attempt to supplement it. However, the abrupt termination near 20.0 w has to be looked after. The pertinent supplemental signal labelled 26 traces a ray path as follows. After the first diffraction at point A, similar to event 25, it darts towards corner D, where it undergoes a second diffraction before re-entering layer I. The corresponding response, shown in Fig. 50, is by no means negligible. Note that it suffers a discontinuity at the receiver at the distance of around 10.0 w, situating above the corner B. Hence, the future appearance of 26 will be supplemented by an additional contribution, this time a thrice diffracted event, corresponding to rays undergoing subsequent diffraction at corners A, D and B.

As before, all the diffracted signals are added together, resulting the synthetic seismograms in Fig. 51. Complemented by the geometric arrival in the vicinity of label 23, the total contribution of this group appears in Fig. 52. Corners A, B and D are equally responsible in generating signal not predicted by the asymptotic ray theory alone.

Figure 47 (a) Radiation characteristics for
the first part of diffracted rays in group IV,
shown in Fig. 45,
(b) shows the corresponding shadow boundary
at corner B.
(c) Radiation characteristics for
the second part of diffracted rays in group IV,
shown in Fig. 46,
(d) shows the corresponding shadow boundary
at corner A.

10%

10%
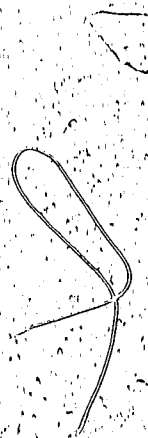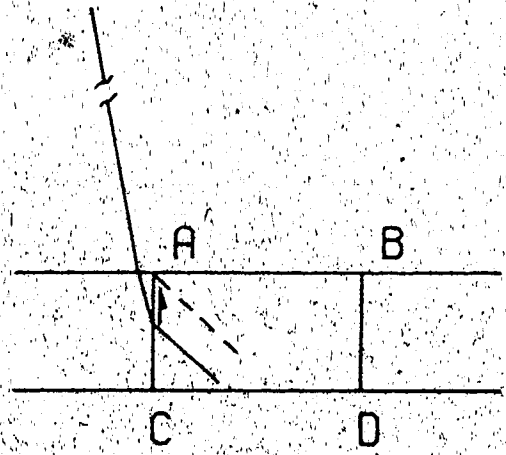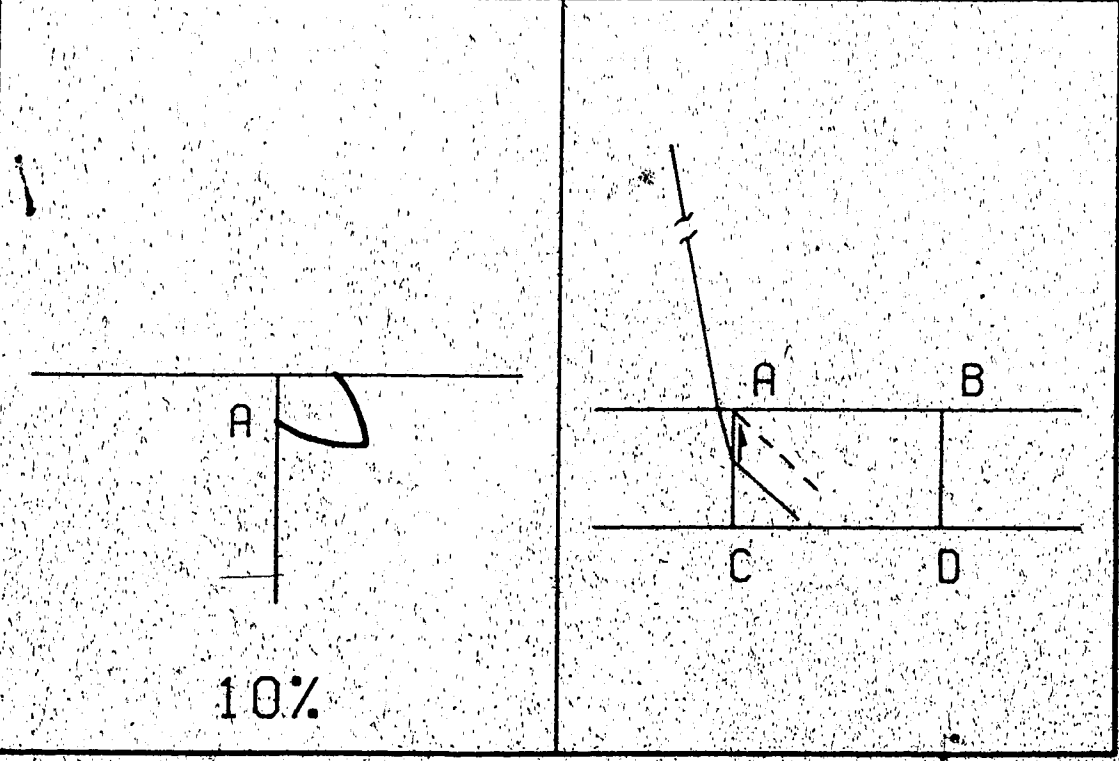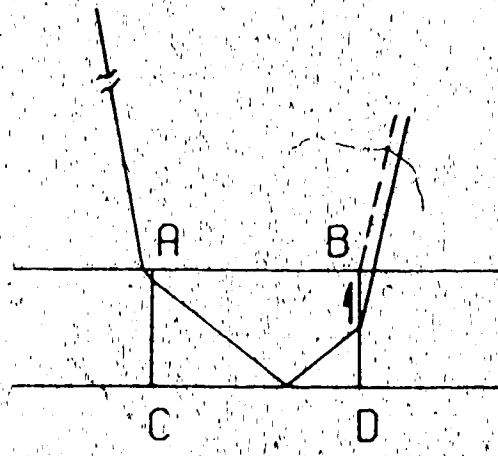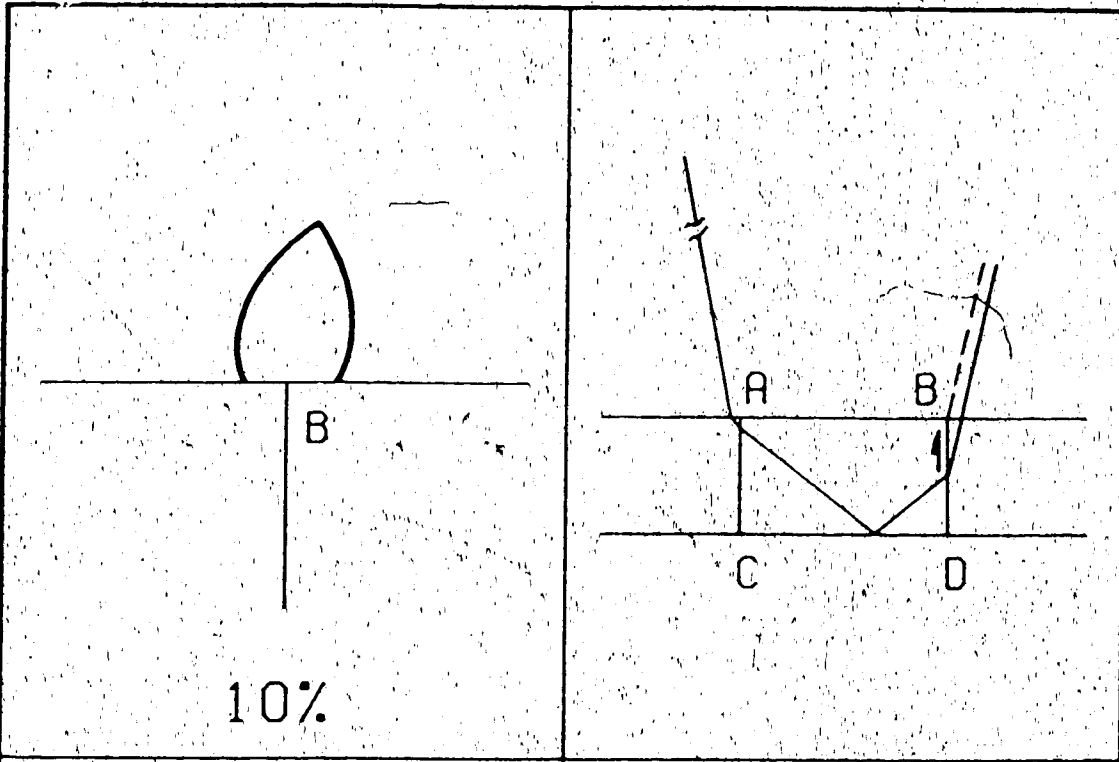
Figure 48 Synthetic seismograms for the first
part of diffracted rays in group IV, see
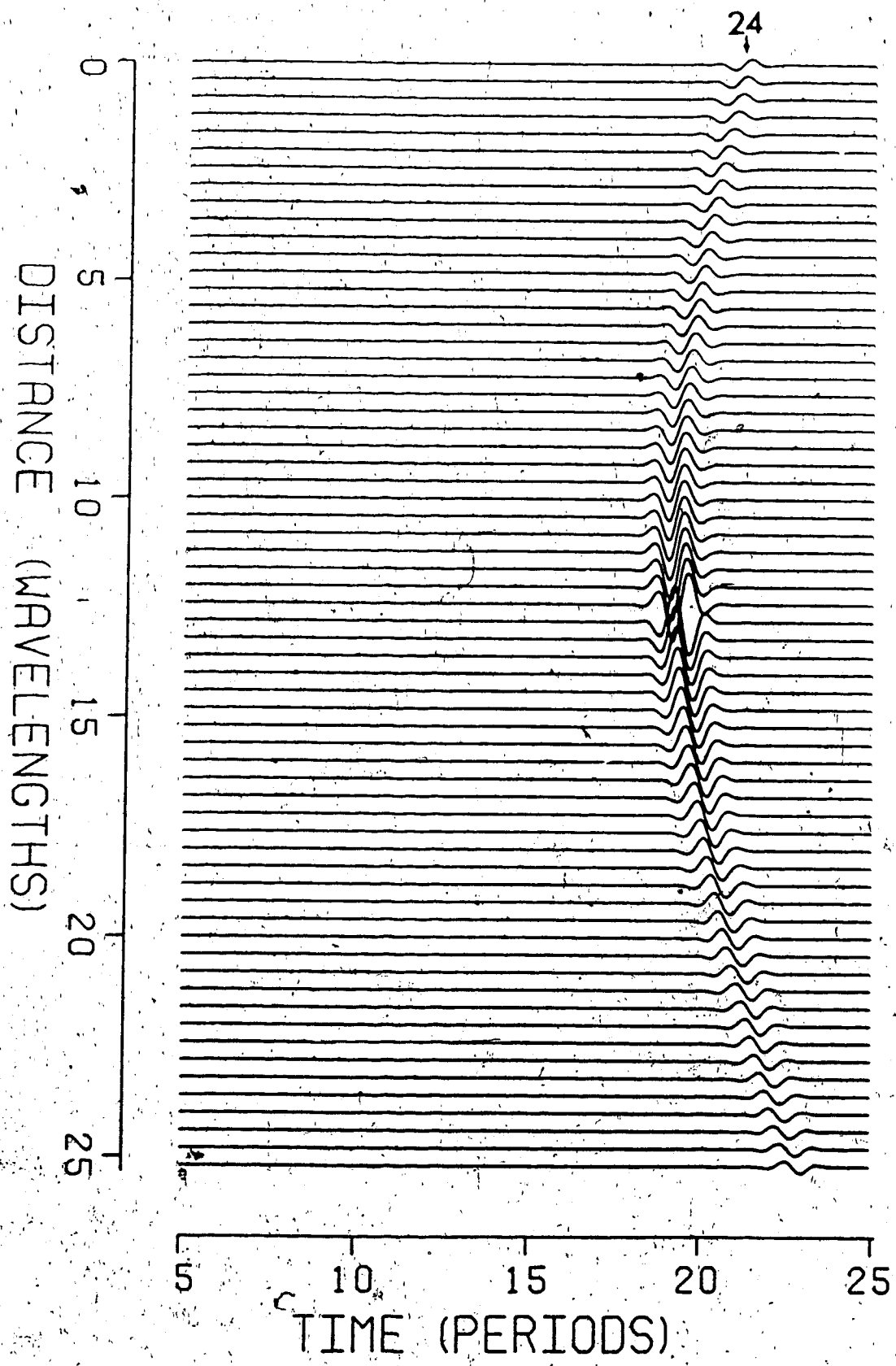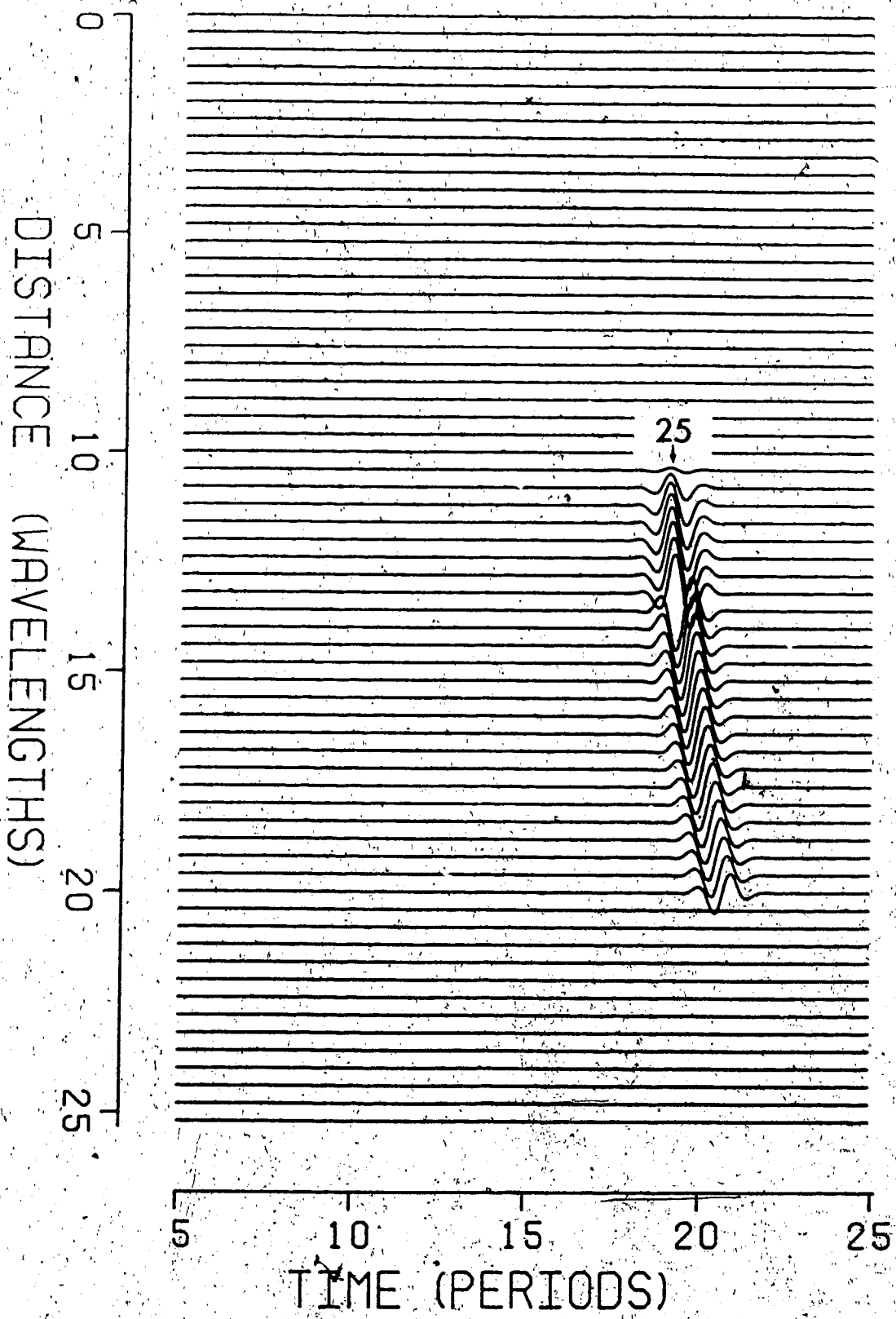Fig. 45.
Point of origination of diffraction - corner B.

Figure 49 Synthetic seismograms for the second

part of diffracted rays in group IV, see

Fig. 46.

point of origination of diffraction - corner A.

Figure 50 Synthetic seismograms supplemental to
event 25, and pertinent to twice diffracted rays
with diffraction points at corners A and D.
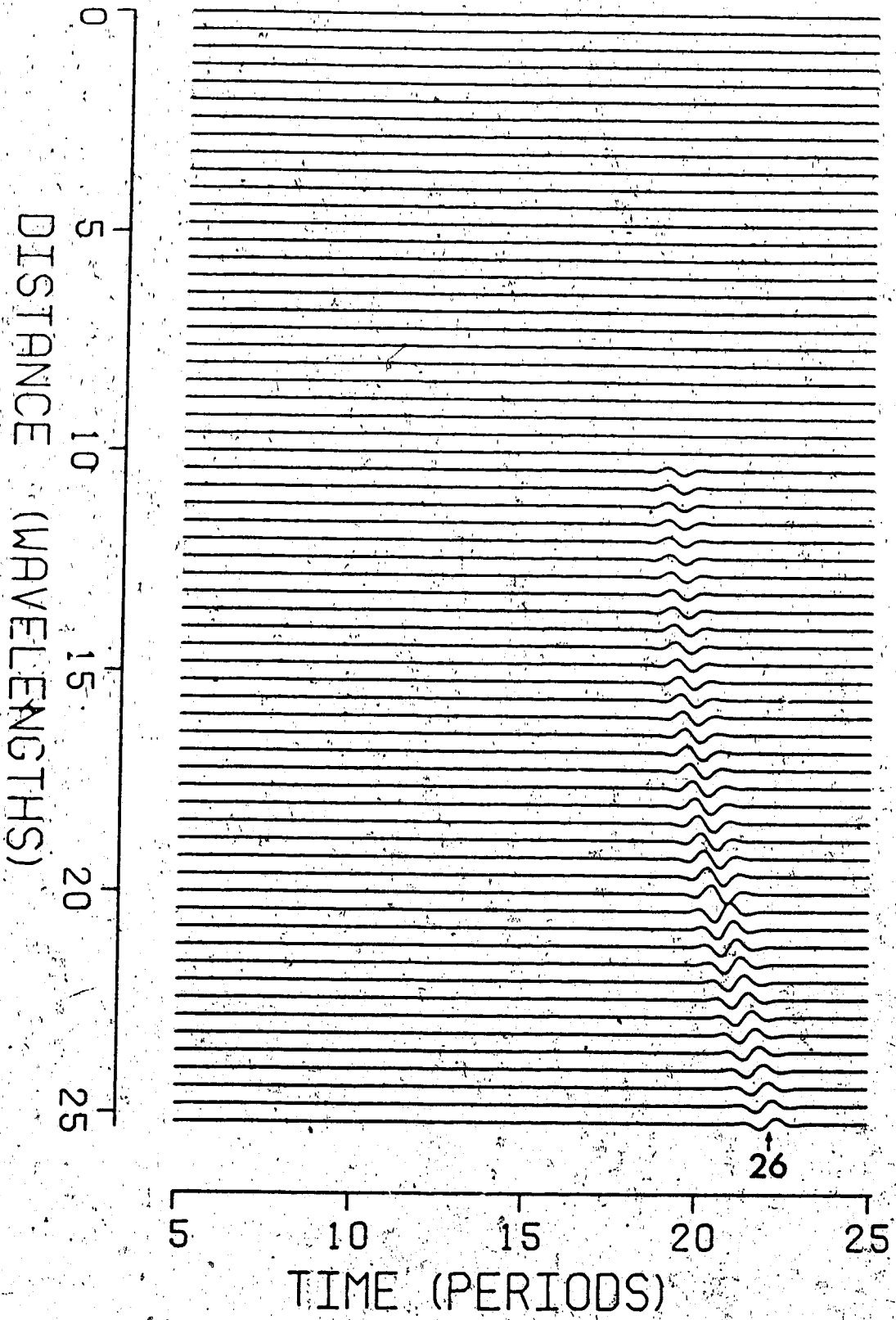
Figure 51 Sum of all diffracted contributions in
group IV.
N.B. contribution 26 here has already been
supplemented in this figure.
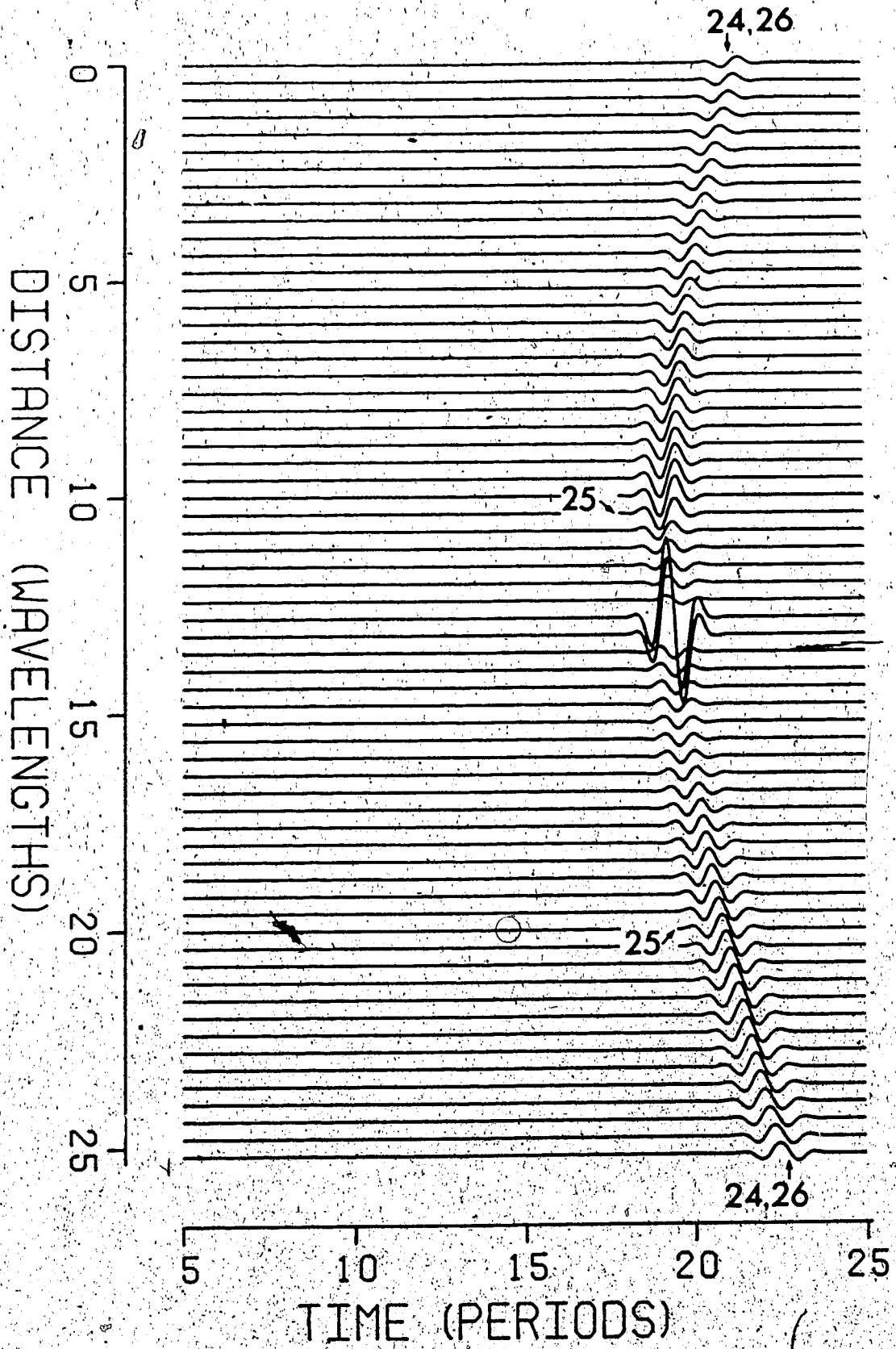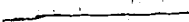
Figure 52 Sum of all contributions in group IV.
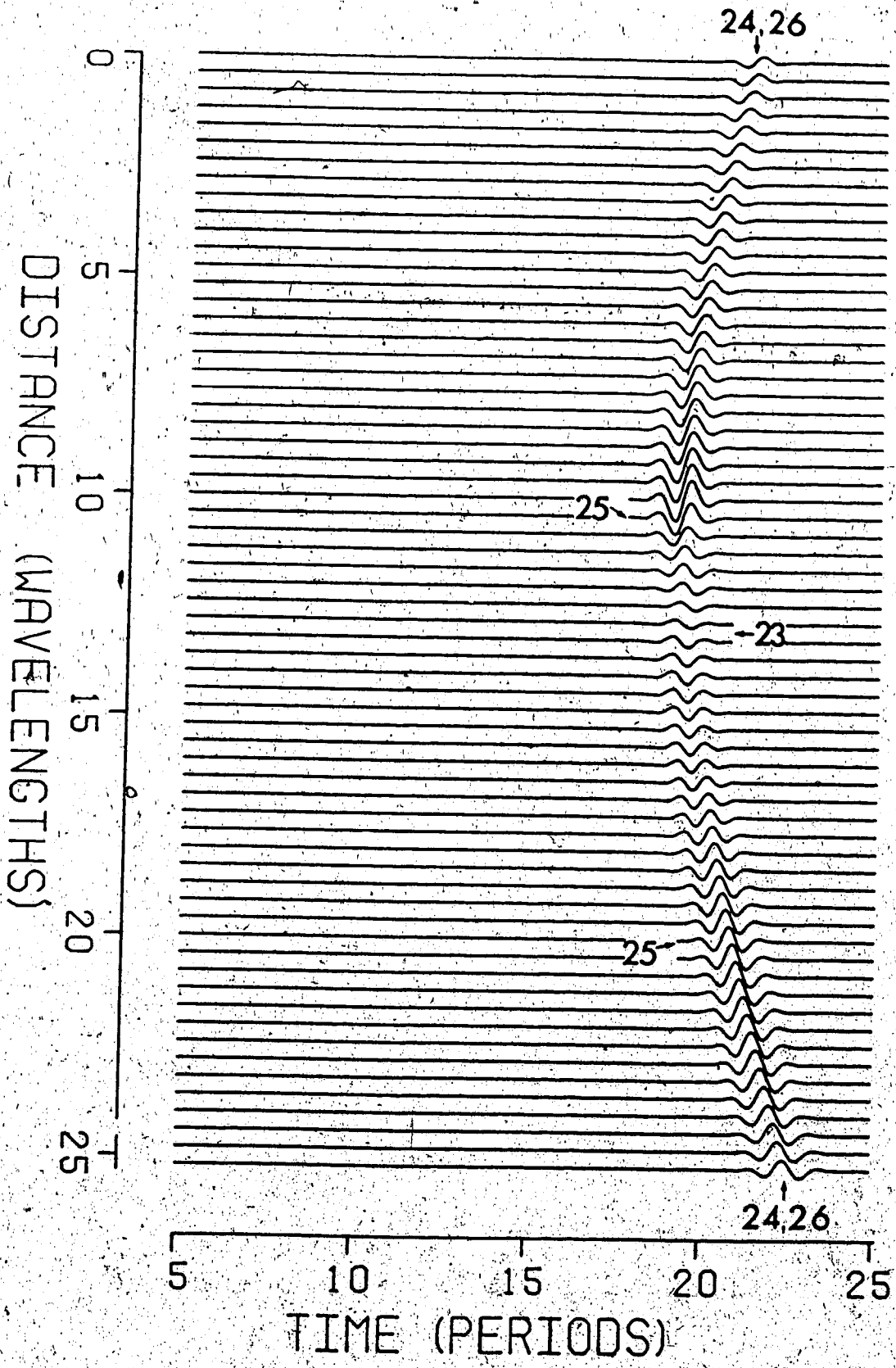
4.8   Group V -- consisting of only diffracted rays

originating at corner C.

One peculiarity in group V is that no geometric rays may arrive at any one of the receivers. In Fig. 53b, the extension of the shadow boundary intersects the boundary BD. Hence, there will be no reflections from $L_2 L_2'$ that can reach boundary AB and escape back into layer I. Notwithstanding the related signals diffracted at C and transmitted through BD and the top interface $L_1 L_1'$ can be registered at the receivers. They are labelled as contribution 27 and shown in Fig.54. The situation in Fig. 53d is different. Although the 4th segment of each geometric ray is transmitted back into layer I, the last segment is bent so close to the boundary AB that no receiver within our range will pick up such signal. Nevertheless, its related signals diffracted at corner C, labelled 29, are shown in Fig. 57. Both types of contribution display abrupt termination due to the existing shadow boundaries similar to those displayed by rays 9, 10 and others. Supplemental fields labelled 28 and 30 are computed for both and shown in Figs. 55 and 58. The smoothed signals of 27+28, and 29+30 are shown in Fig. 56 and 60, respectively. And finally, 27 through 30 are summed to give the group V total field (see Fig. 60). This is the first time when corner C plays an important role in the diffracted field.

Figure 53 (a) Radiation characteristics for the
first part of once diffracted rays in group V
(b) shows the corresponding shadow boundary at
corner C.
(c) Radiation characteristics for the
second part of once diffracted rays in group V
(d) shows the corresponding shadow boundary at
corner C.
N.B. In both cases, a diffracted ray from
corner C will travel in the box before
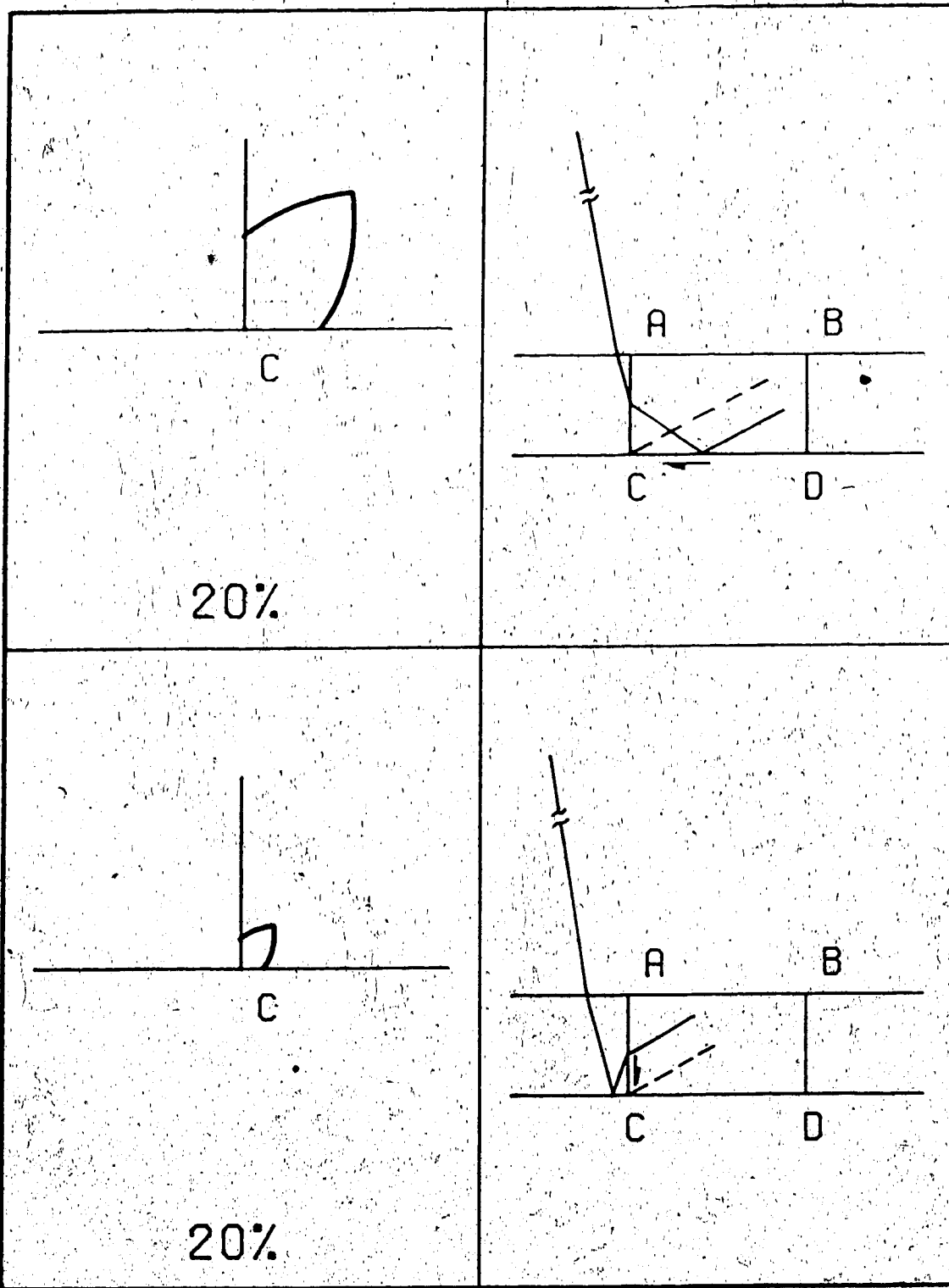being transmitted back into layer I.

20%

20%
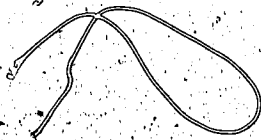
Figure 54 Synthetic seismograms for rays diffracted
at C and described in Fig. 53b.

DISTANCE (WAVELENGTHS)

TIME (PERIODS)
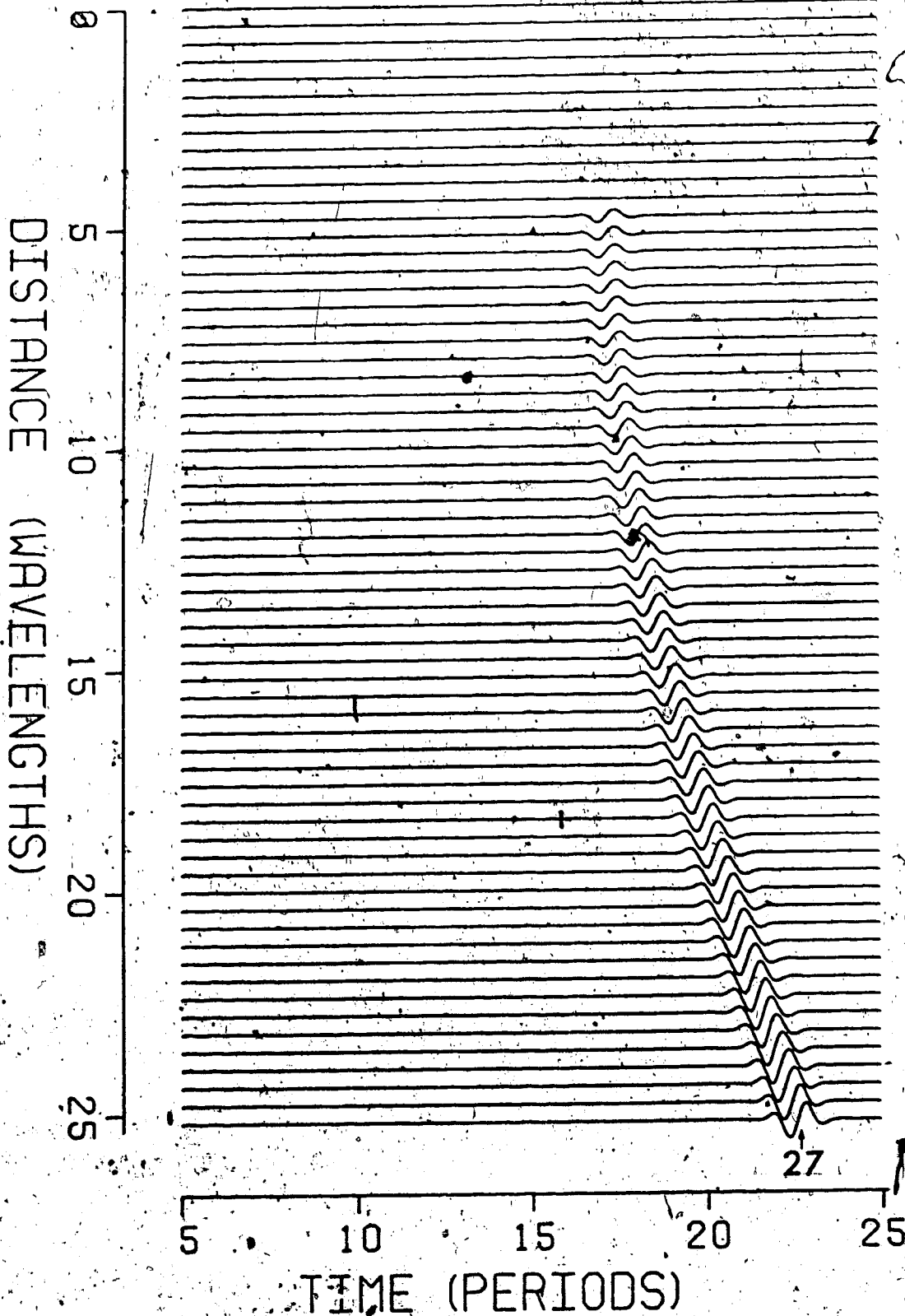
Figure 55 Supplemental signal to contribution 27.

It corresponds to rays twice diffracted corners

C and B.
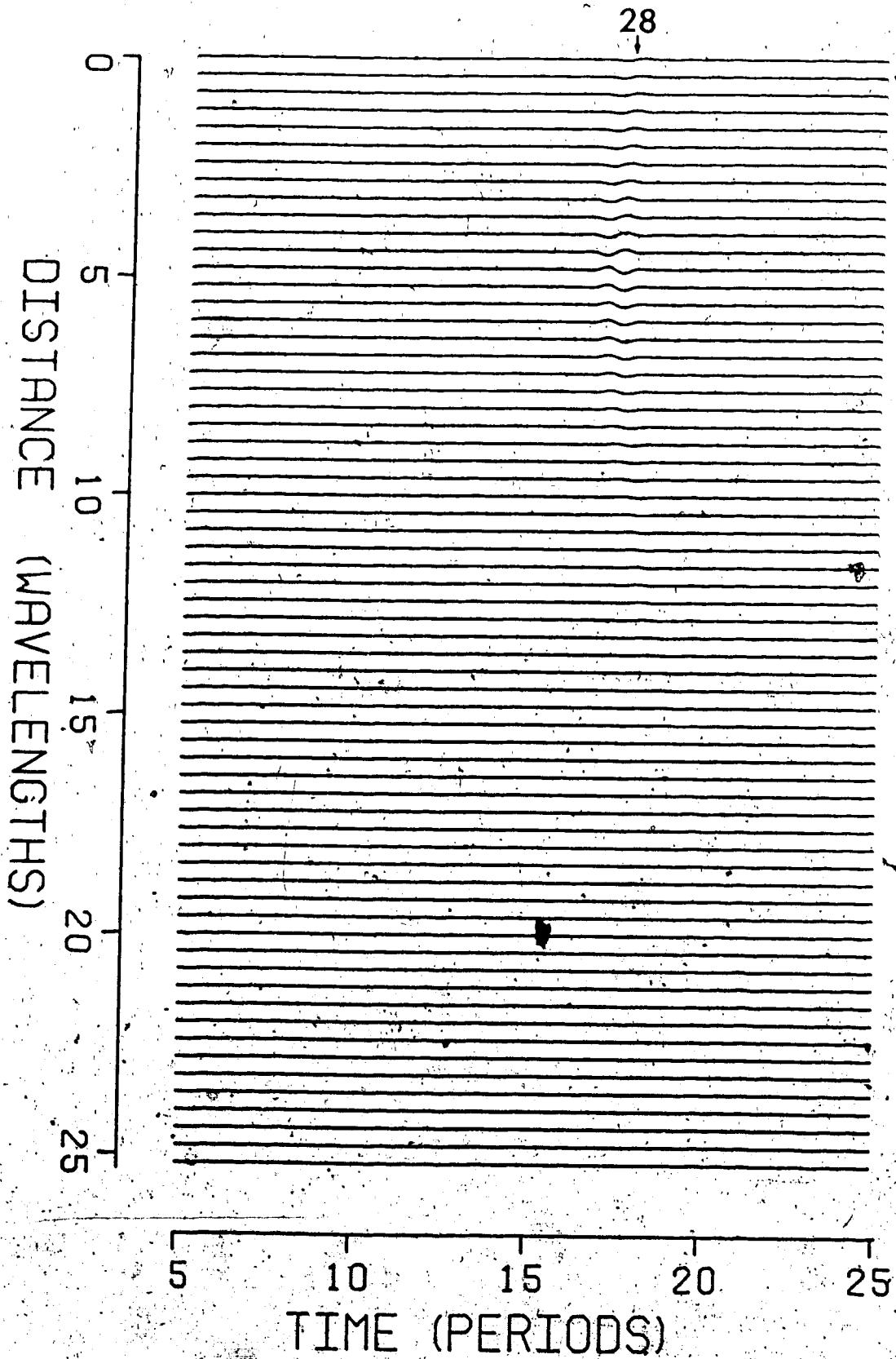
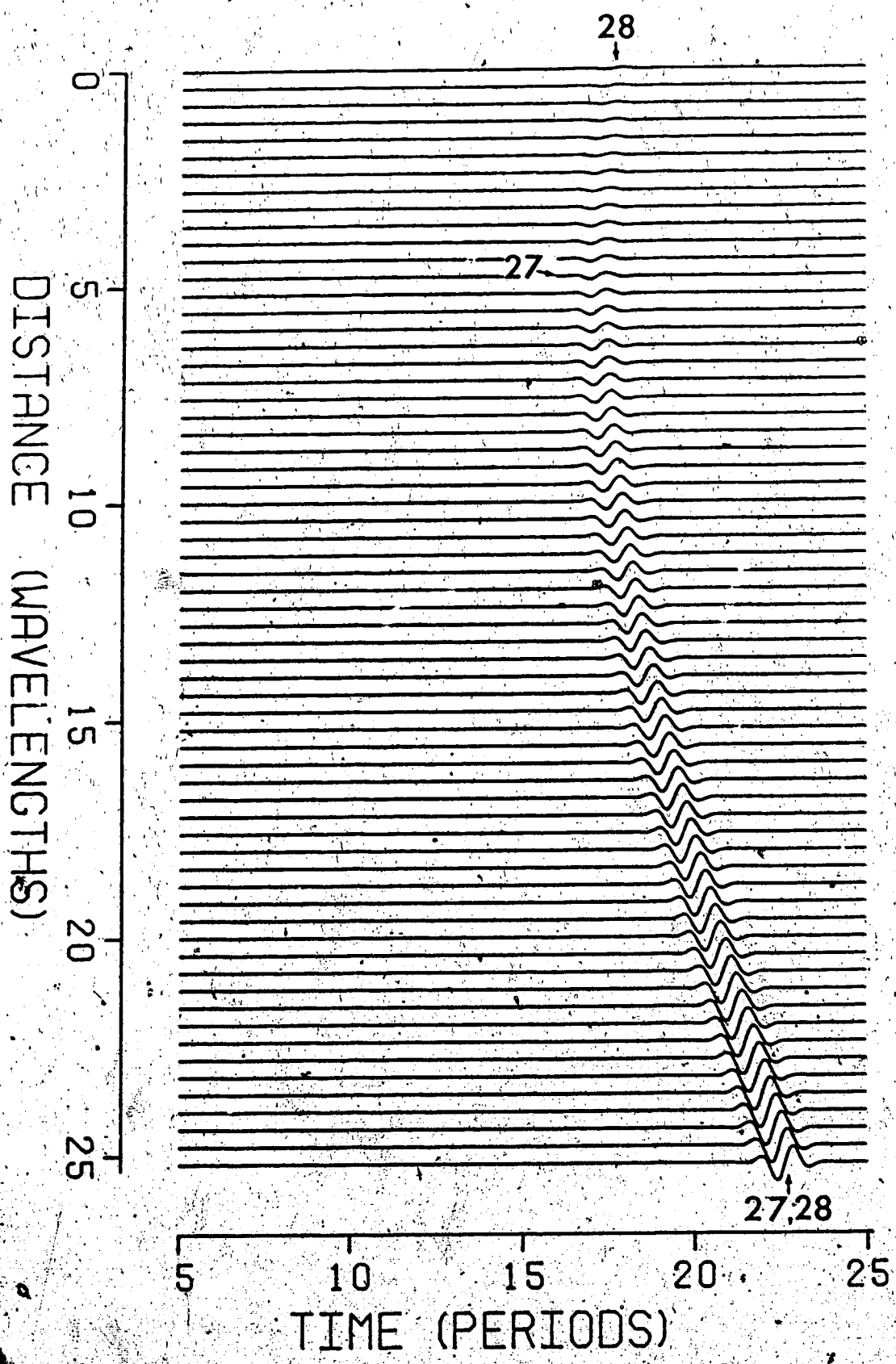Figure 56. Sum of diffracted contributions 27 and 28.

Figure 57. Synthetic seismograms for rays diffracted
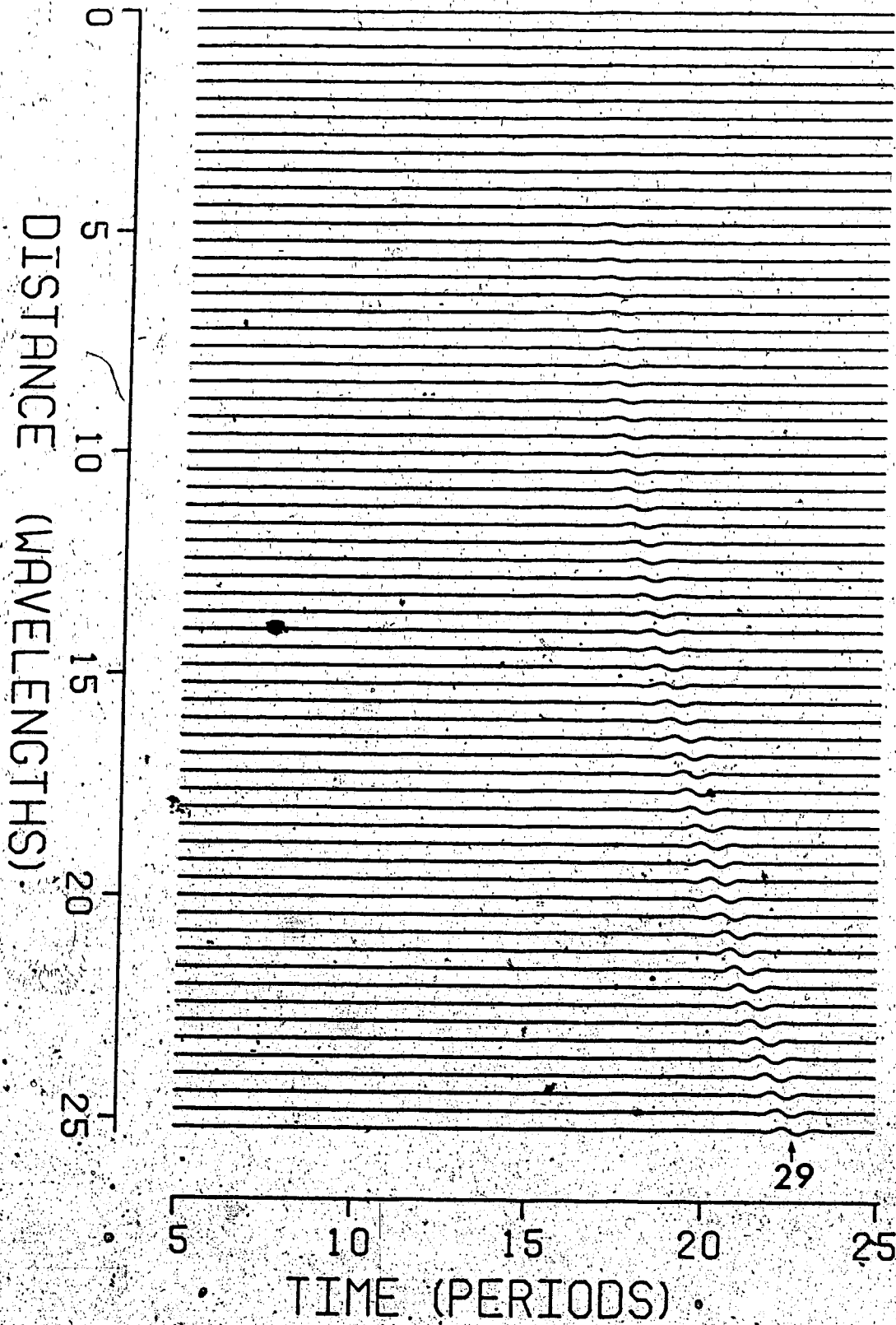at corner C and described in Fig. 53d.

Figure 58 Supplemental signal to contribution 29.
         It corresponds to rays twice diffracted at corners
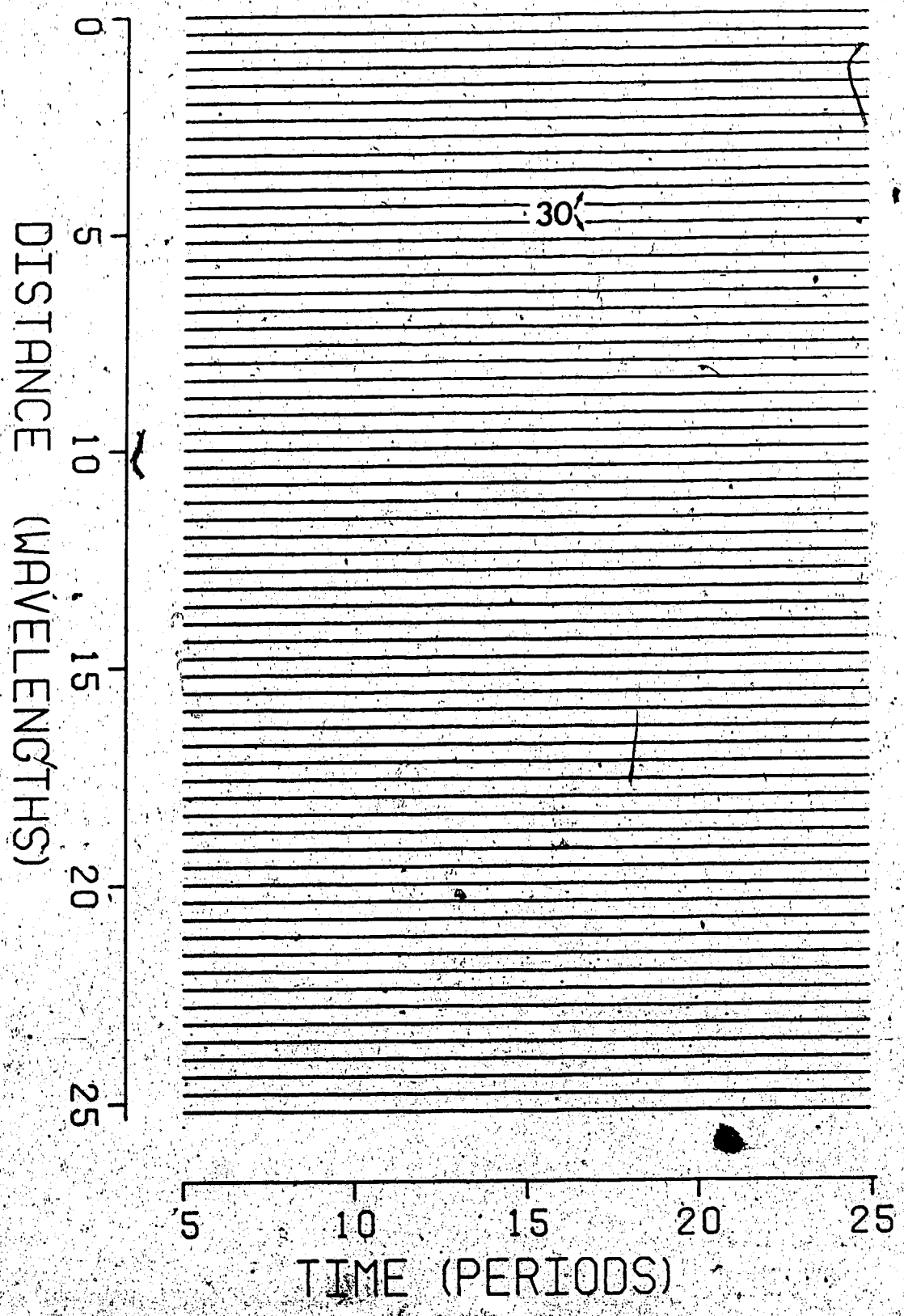   C and B, see Figs. 53d and 57.
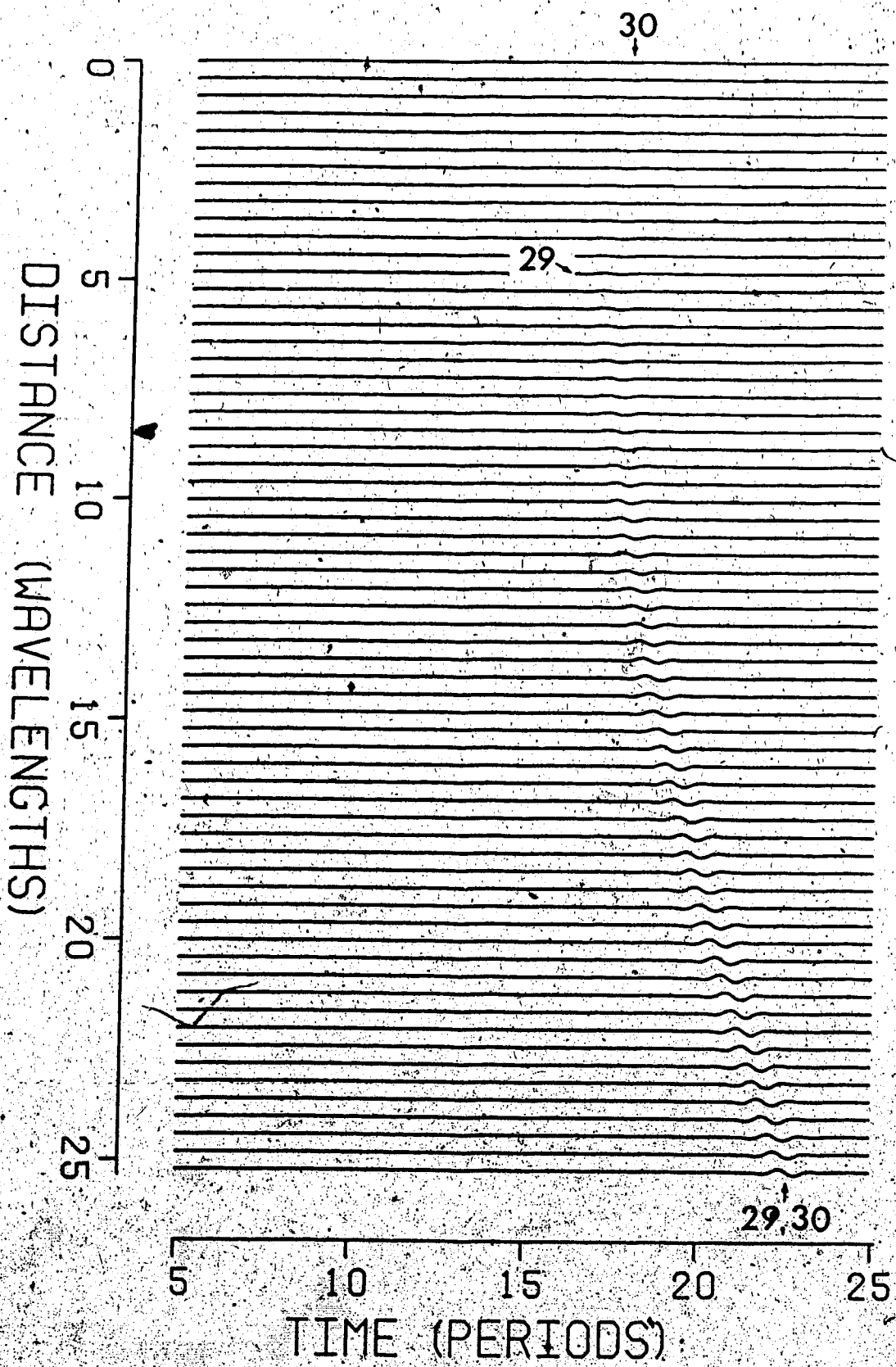
Figure 59 Sum of diffracted contributions 29 and 30.

DISTANCE (WAVELENGTHS)

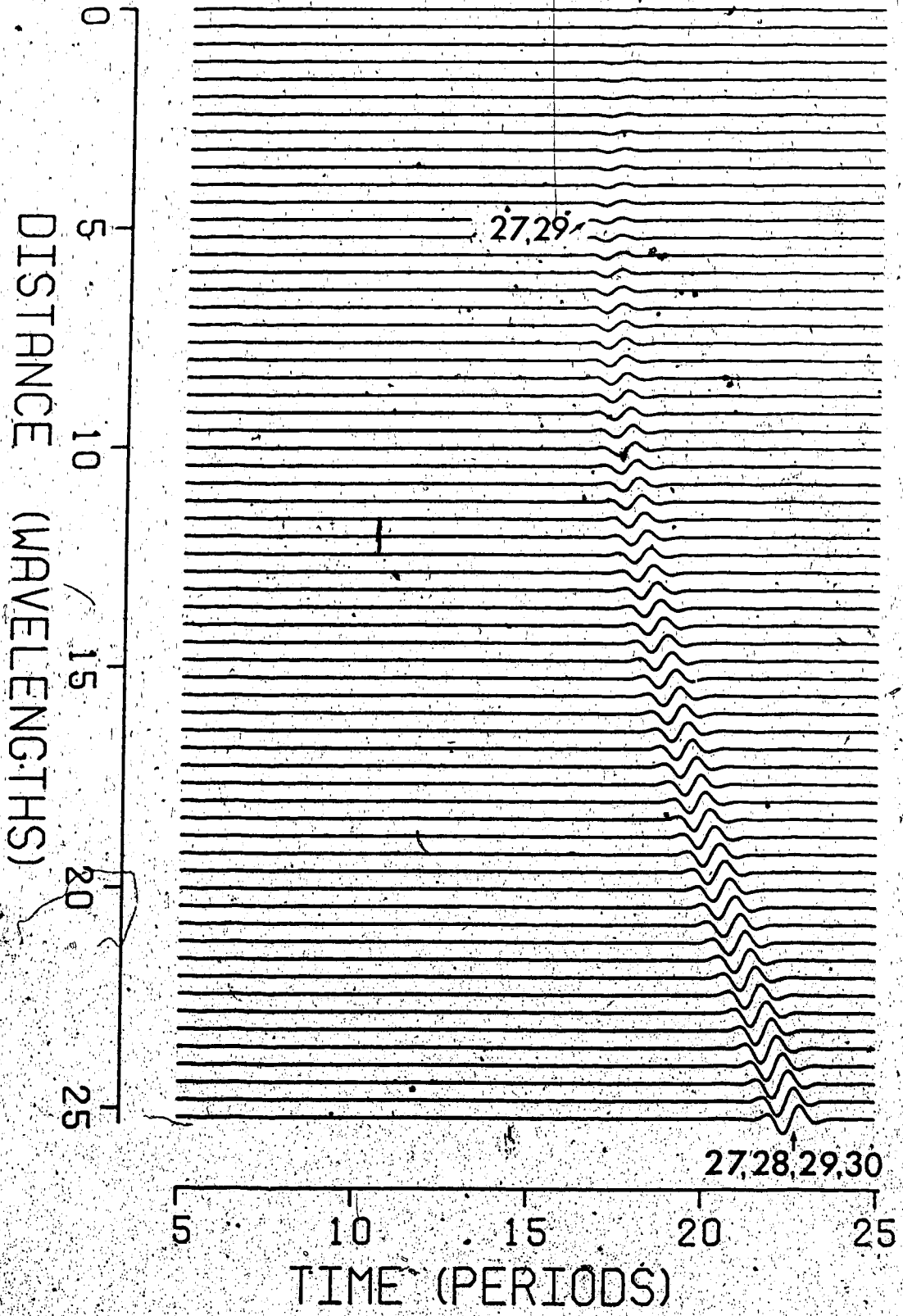TIME (PERIODS)

Figure 60 Sum of all contributions in group V.

4.9   Group VI -- consisting of rays reflected from the
                    bottom of the box and diffracted at B on
                    their way to layer I

Fig. 61 shows the ray paths of a bundle of diffracted
signal. Note that all receivers within the prescribed range
are on the shadow side. See Fig. 62b for the position of the
shadow boundary. The radiation characteristic in Fig. 63a
indicates a small amplitude throughout, except for stations
near point R. The response, coded 31, is shown in Fig. 63.
This is the only and total contribution for group VI.

4.10   Group VII -- consisting of rays diffracted at
                    corner A, reflected from the bottom
                    of the box and directly entering
                    layer I through the top of the box

The description of the ray paths of group VII has to be
traced back to Figs. 46 and 47d of group IV. Instead of
entering the section of layer II to the right of the box,
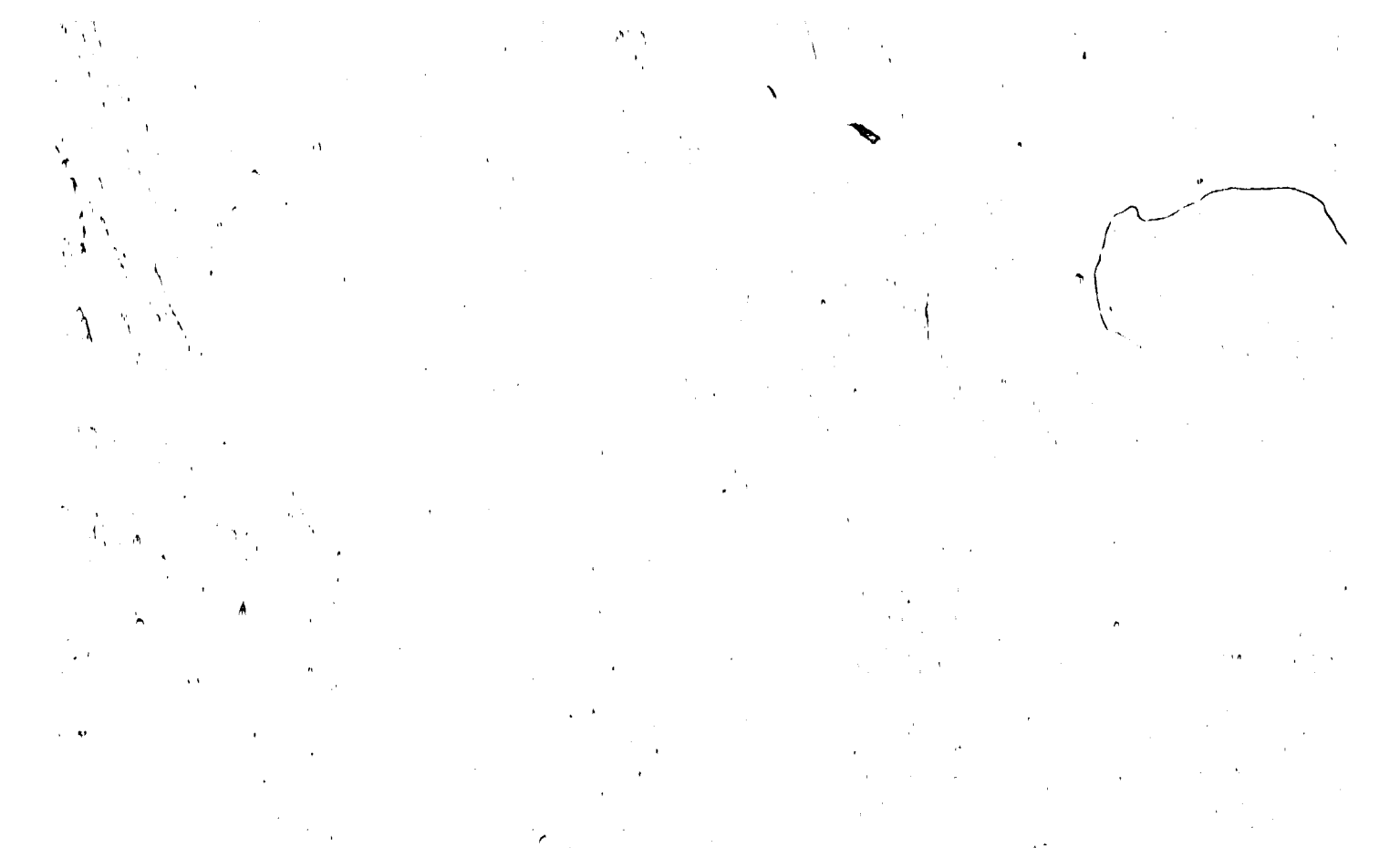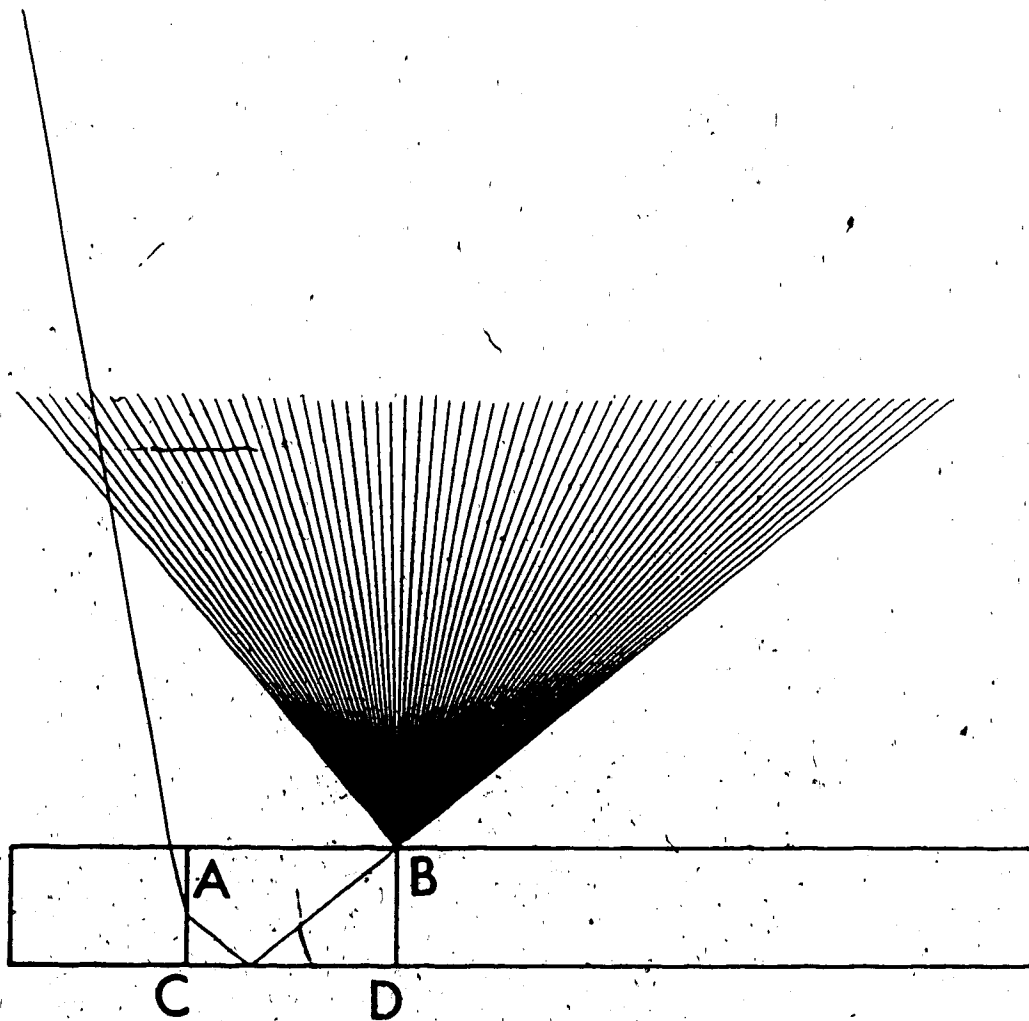the rays diffracted at corner A are reflected from the L_2L_2'

Figure 61 Ray diagram for diffracted rays in
group VI.

Note that all receivers are on the shadow side of
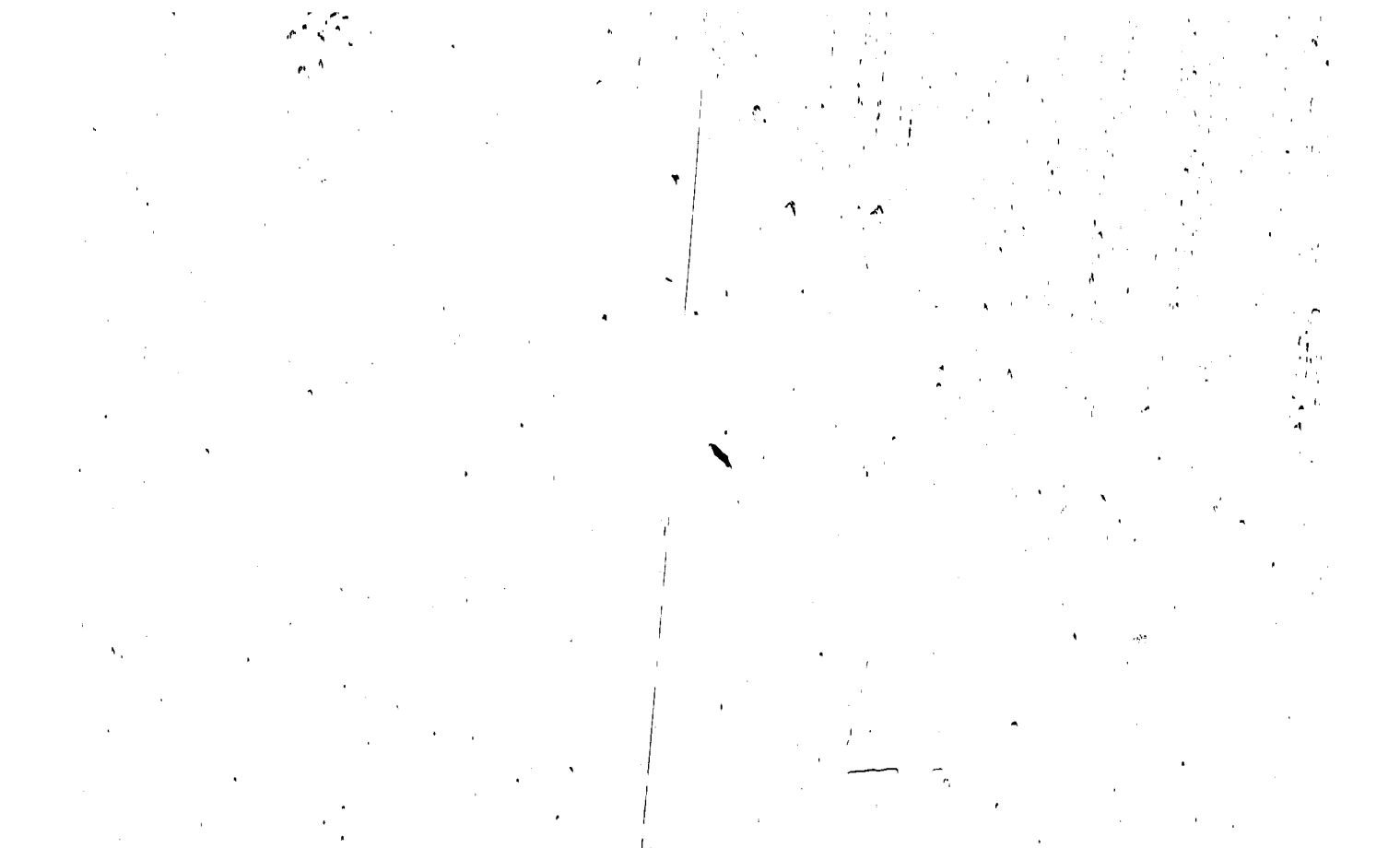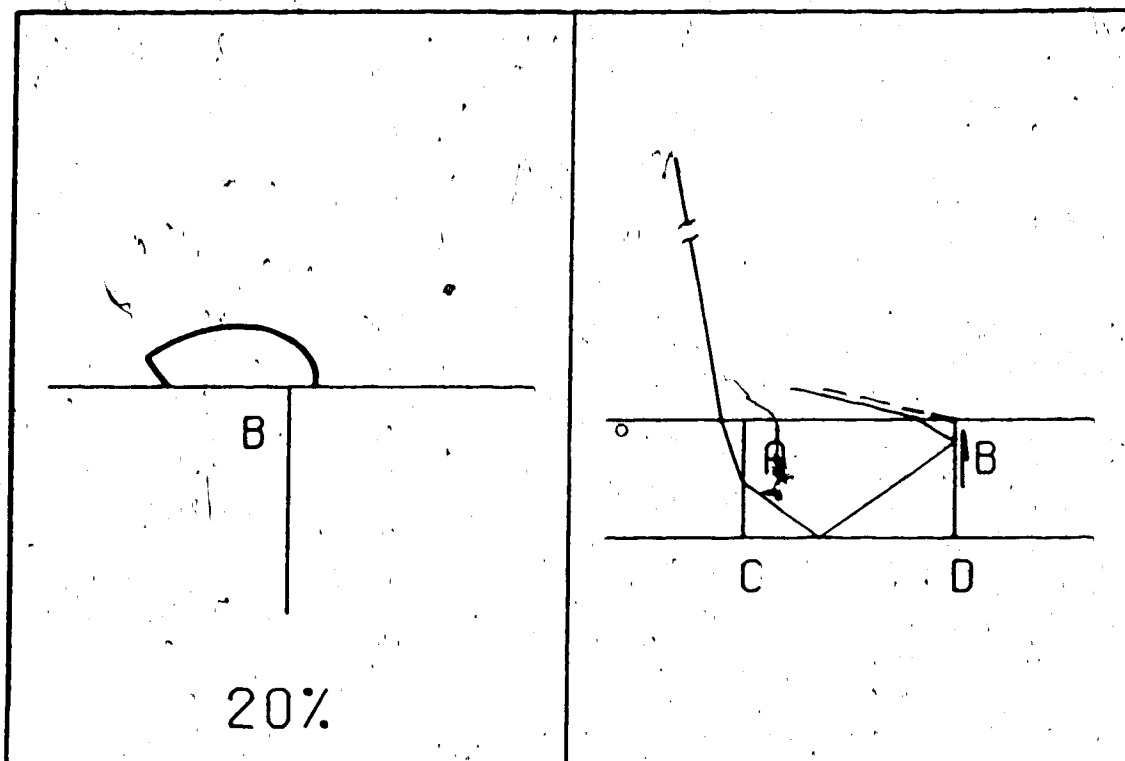the shadow boundary (see Fig. 62b).

Figure 62 (a) Radiation characteristics for the

diffracted rays in group VI.

(b) shows the corresponding shadow boundary at
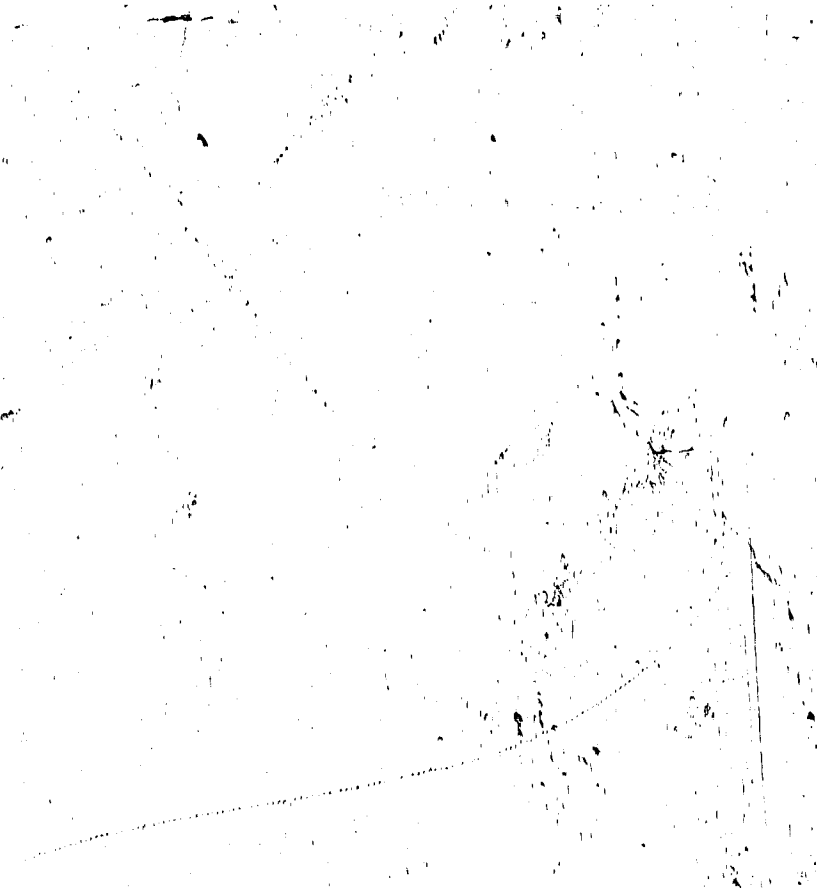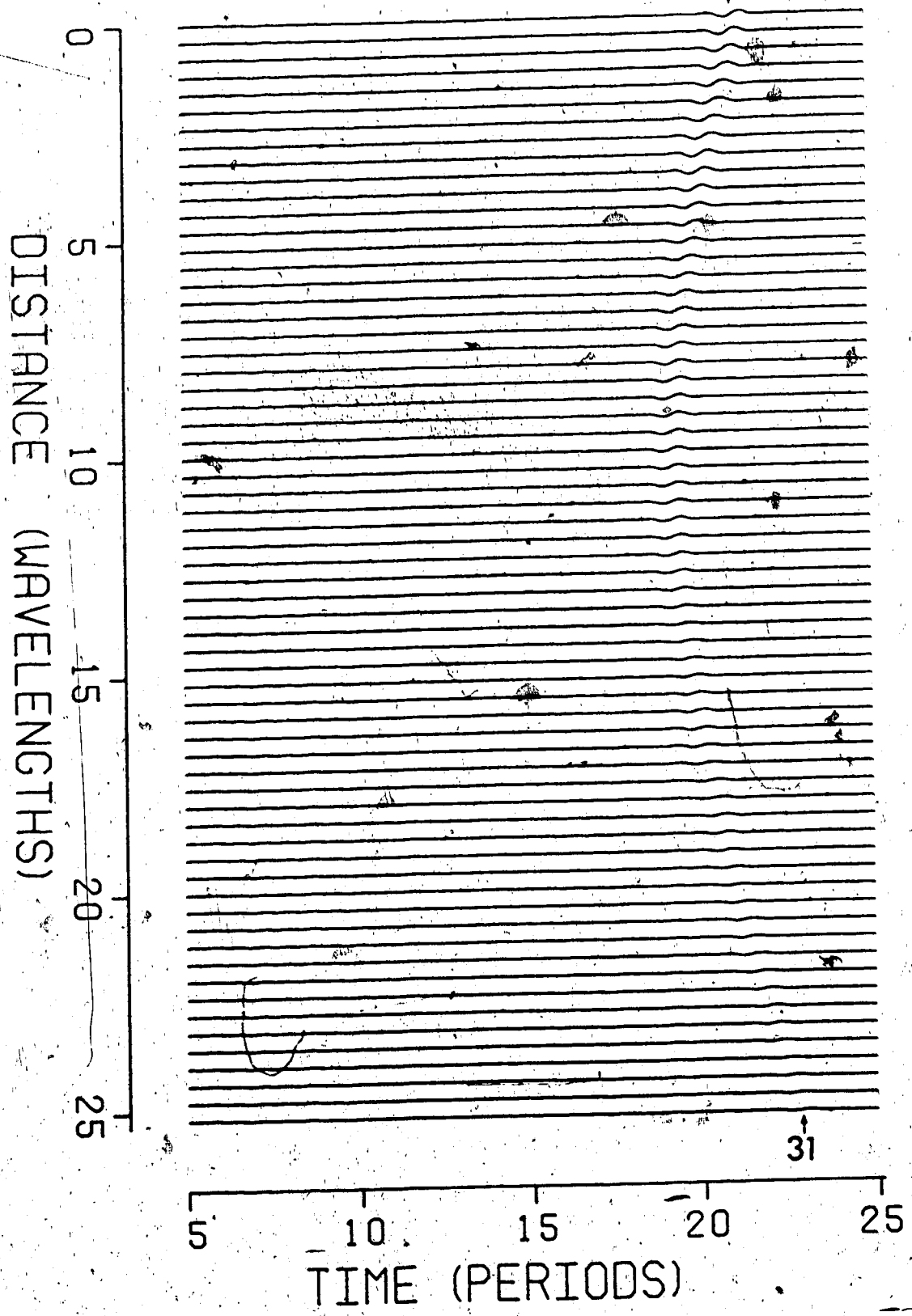
corner B.

20%

B

C   D

Figure 63 Synthetic seismograms for diffracted

arrivals in group VI.

The diffraction point is at corner B.

boundary before re-entering layer I. It is also in some way

similar to events 9 and 10 in group II. The synthetic

seismograms of this event, coded 32, are shown in Fig. 64.

The phase change in the reflection coefficient upon the

reflection at boundary L_2L_2' provides the phase reversal near

the receivers at distance of approximately 15.0 w. This

event shares the same time branch as event 9. In fact, they

have the same apparent ray paths. The only difference being

that event 32 is a 5-segmented ray, while that of 9 is

4-segmented. In Fig. 64, the strong amplitude at receivers

near R' is two to three time larger than those from event 9,

and its significance is immediately noted in the final

composition of the grand total result.

4.11⁄   Group VIII

Fig. 65 shows the ray paths of group VIII diffracted

signals. Similar to group VII diffraction, one has to trace

back to Figs. 53b,d to find the origination of the ray

bundles. The group V events are the diffracted rays at

corner C which return to layer I via sectioned box. Group

VIII will deal with those diffracted rays which transmit

across the boundary BD into layer II before re-entering

layer I. Again, no geometric rays may be traced to any

Figure 64 Synthetic seismograms for diffracted

arrivals in group VII, see Figs. 45 and 46d

for the initial ray path.

Diffraction occurs first at corner A.

The diffracted ray is reflected from the

boundary L_2L_2'. It travels upwards in

the box before being transmitted back into

layer I.

DISTANCE (WAVELENGTHS)

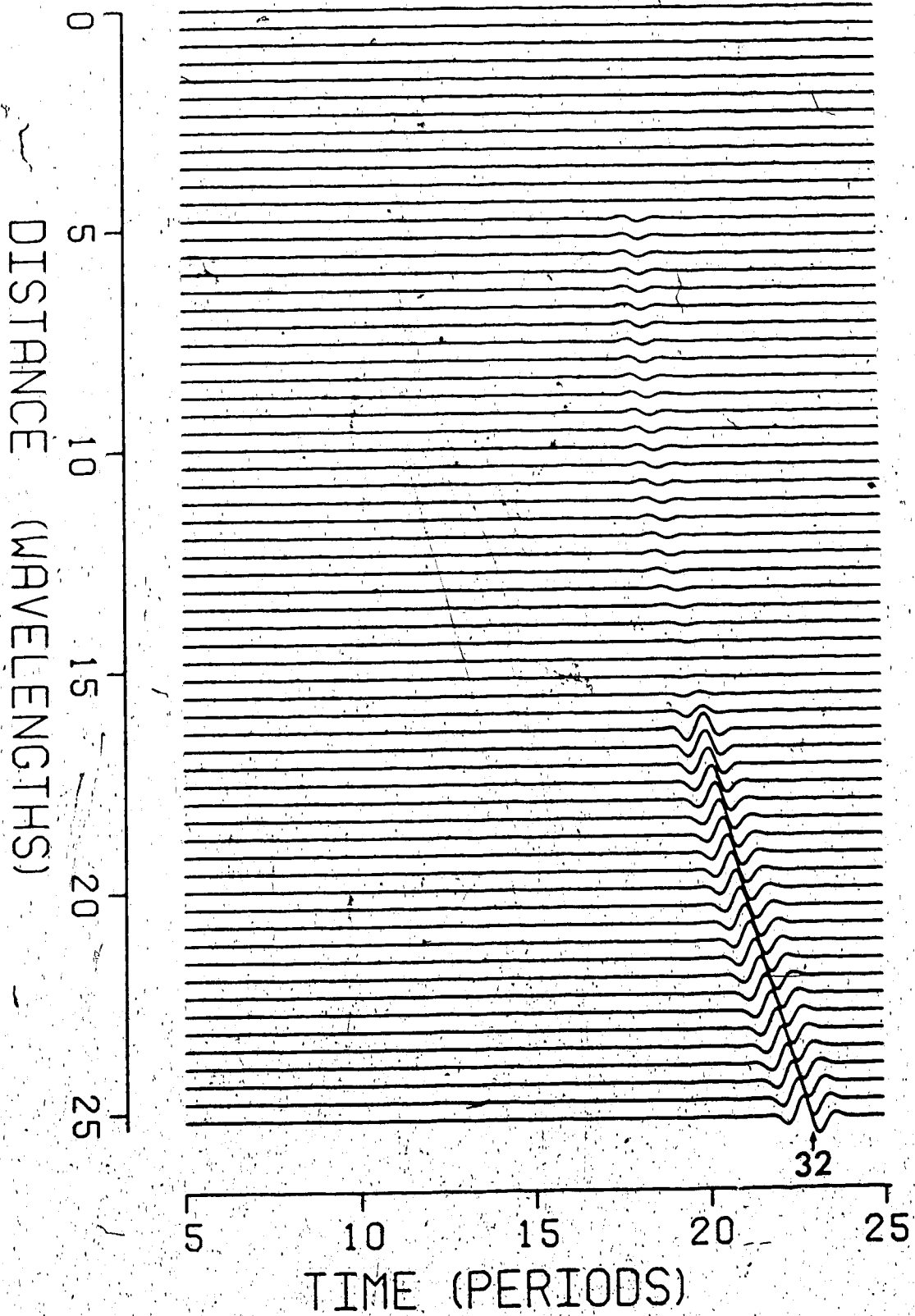TIME (PERIODS)
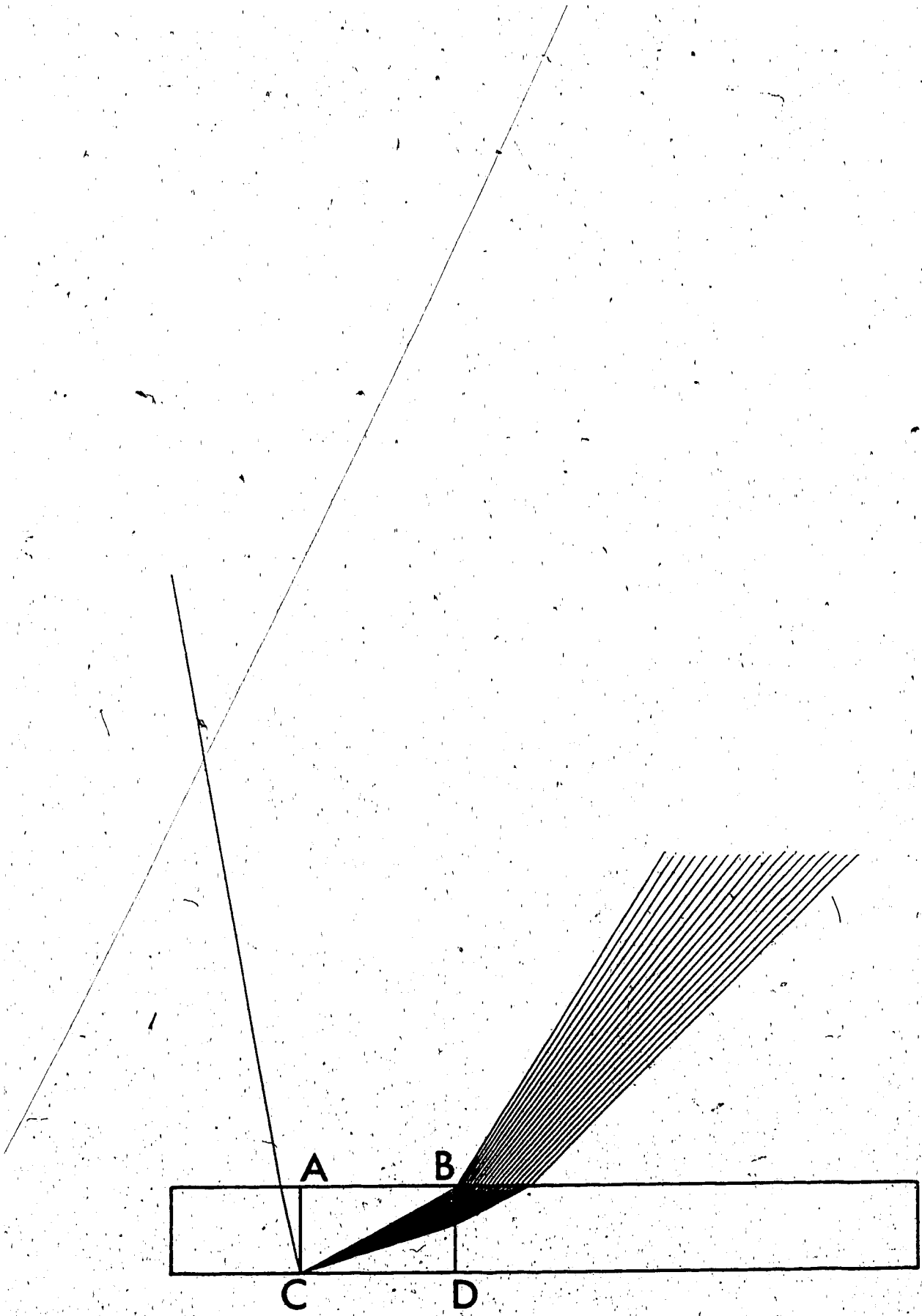
32

Figure 65 Ray diagram for diffracted rays in
          group VIII.
          See Fig. 53 for the initial ray path.
          Note that there are two parts of this diffraction.
          After the diffracton at corner C, a diffracted ray
          in group VIII will hit the boundary BD, transmits
          into layer II and then layer I.

receivers, a situation similar to the argument in section 4.8.

The corresponding synthetic seismograms coded 33 and 35 are shown in Figs. 66 and 69. Both types of contributions suffer discontinuities as described for event 27, 29 and among others. Supplemental fields coded 34 and 36 are computed and shown in Figs. 67 and 70. The smoothed signals of 33+34 and 35+36 are shown in Figs. 68 and 71. And finally, event 33 through 35 are summed (see Fig. 72), to give the group VIII total response. The different move out patterns between groups V and VIII will produce a series of destructive, constructive and destructive interferences along the receiver line RR'. The net result will be discussed upon the completion of the final picture.

4.12   Total response

The above eight groups of selected rays by no means represent the total response. But, they accounted for all the signals strong enough to be identified in the previously mentioned seismic profiles provided by the Alekseev-Mikhailenko method (AMM), shown in Fig. 11.

Sections 4.4 to 4.11 discuss in detail the composition

Figure 66 Synthetic seismograms for the first part

of diffracted rays in group VIII - see

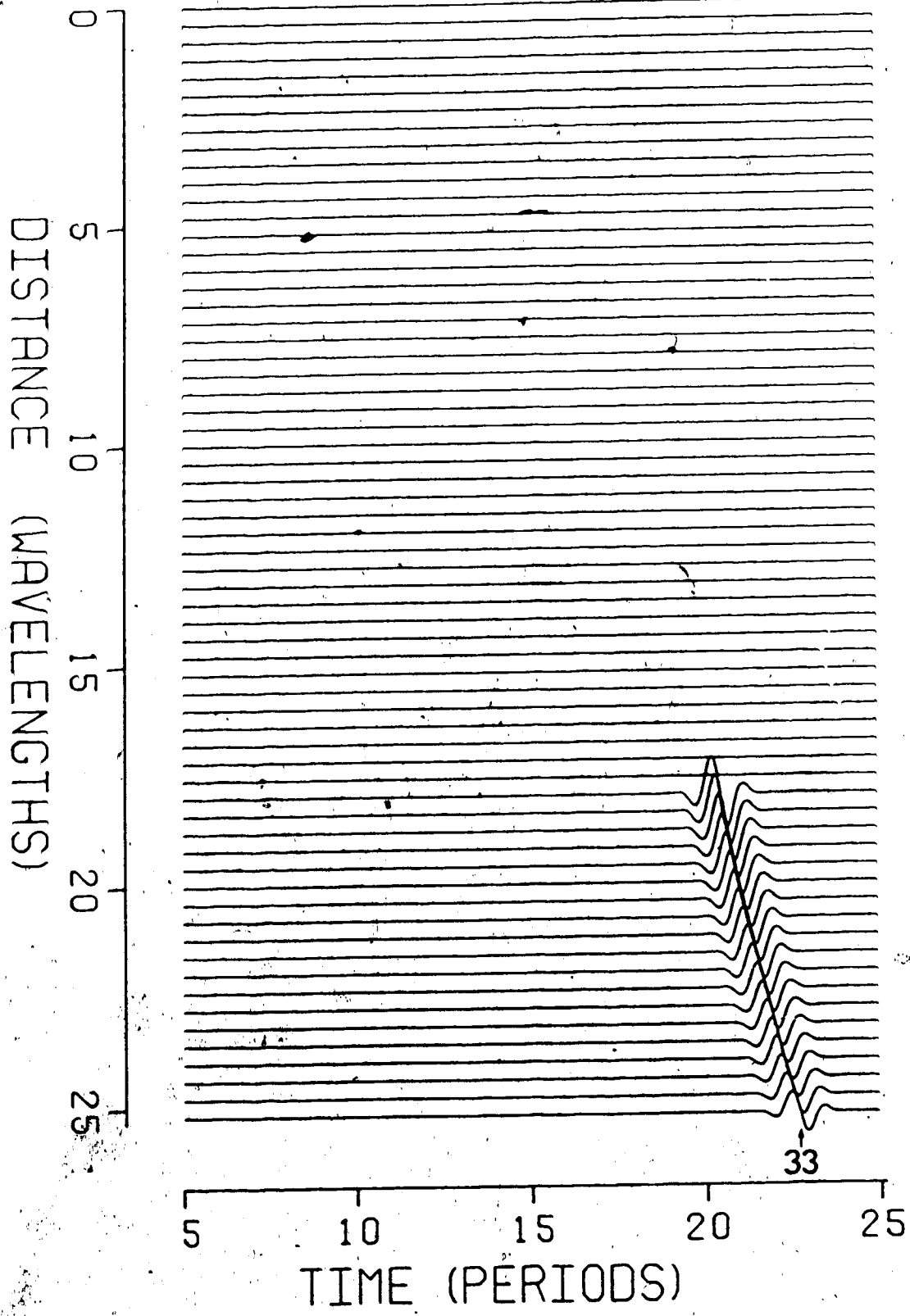also Fig. 53b.

Note that the first reflection occurs in the box.

Figure 67 Supplemental to contribution 33.

It corresponds to twice diffracted rays at
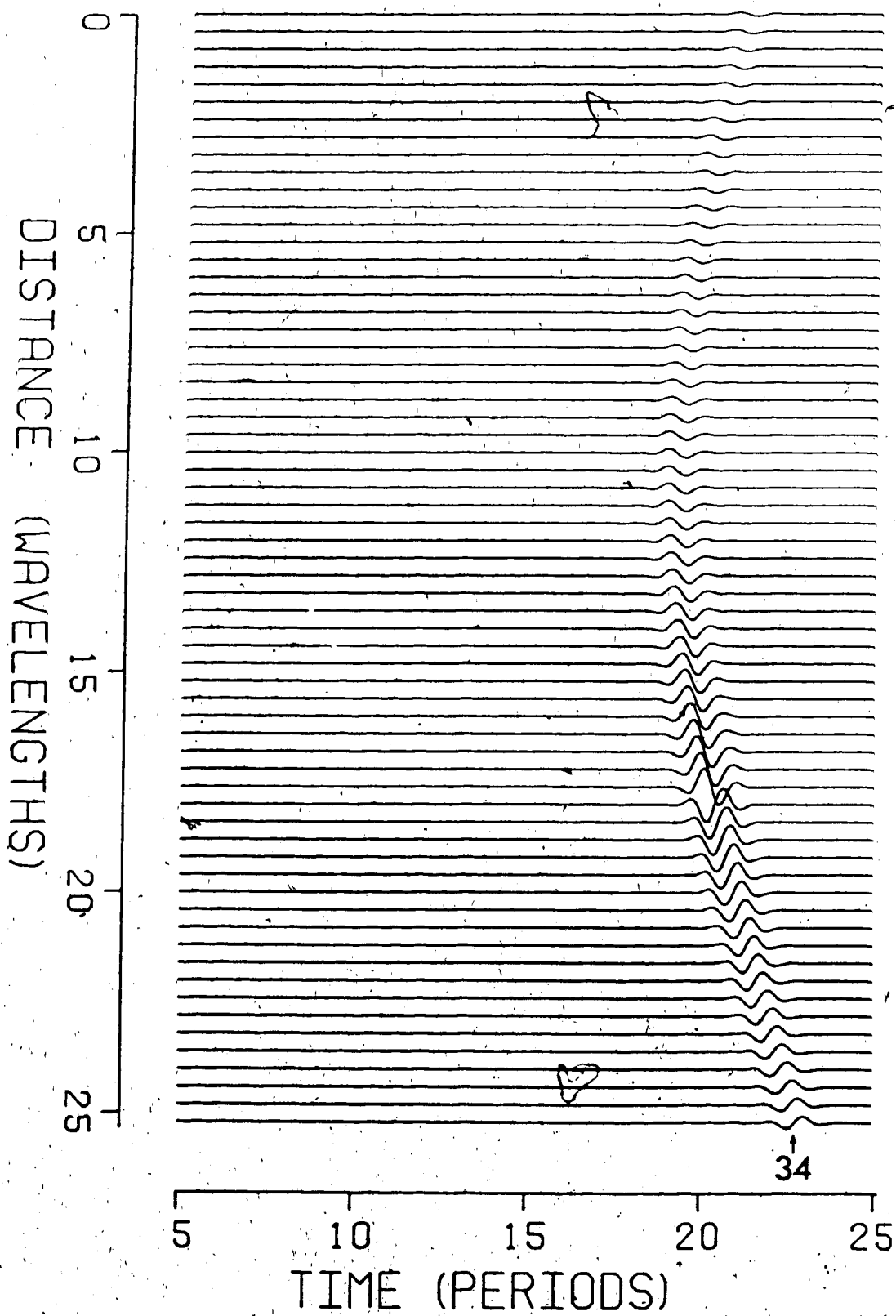
corner C and B.

DISTANCE (WAVELENGTHS)

TIME (PERIODS)

34

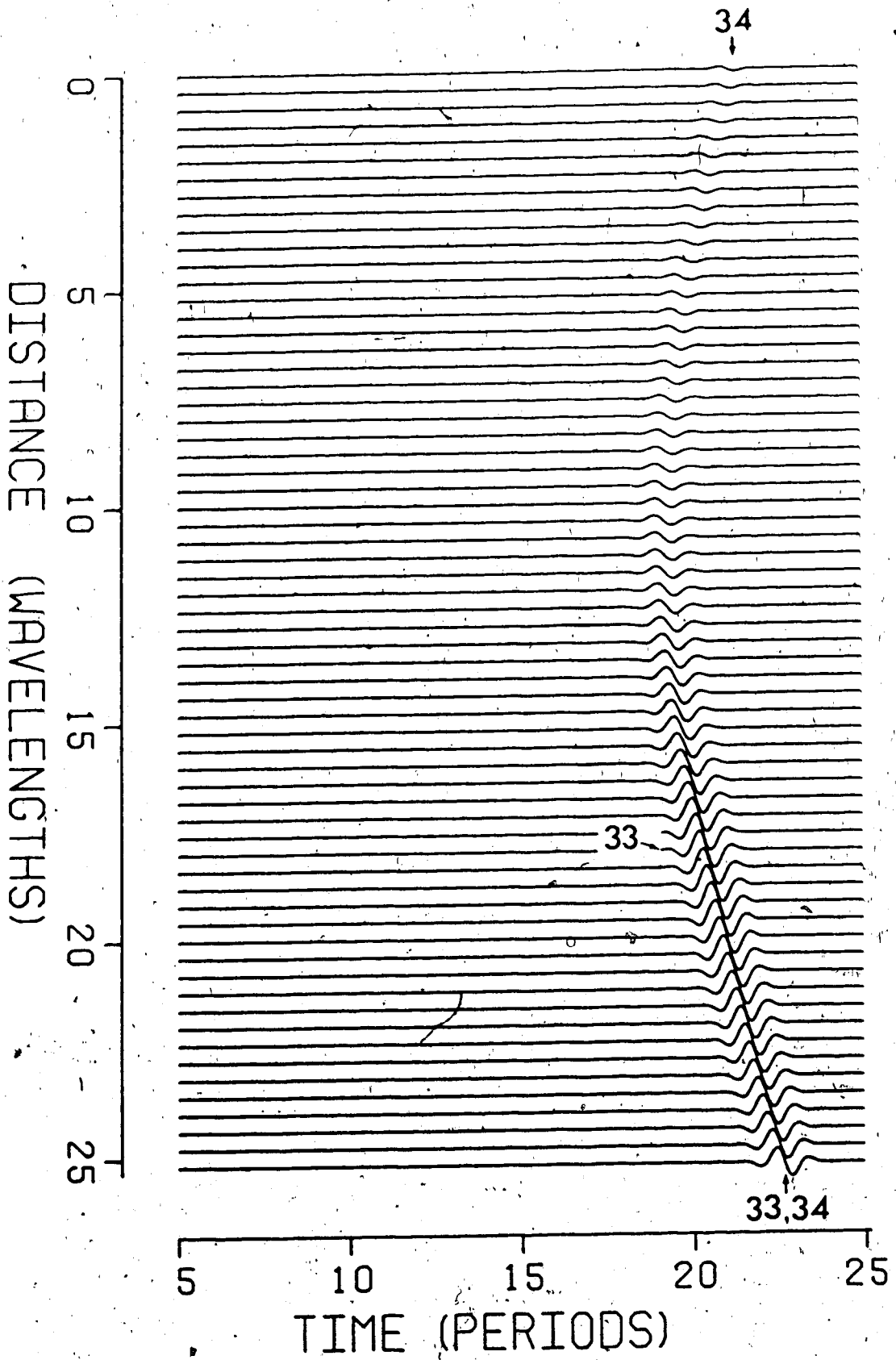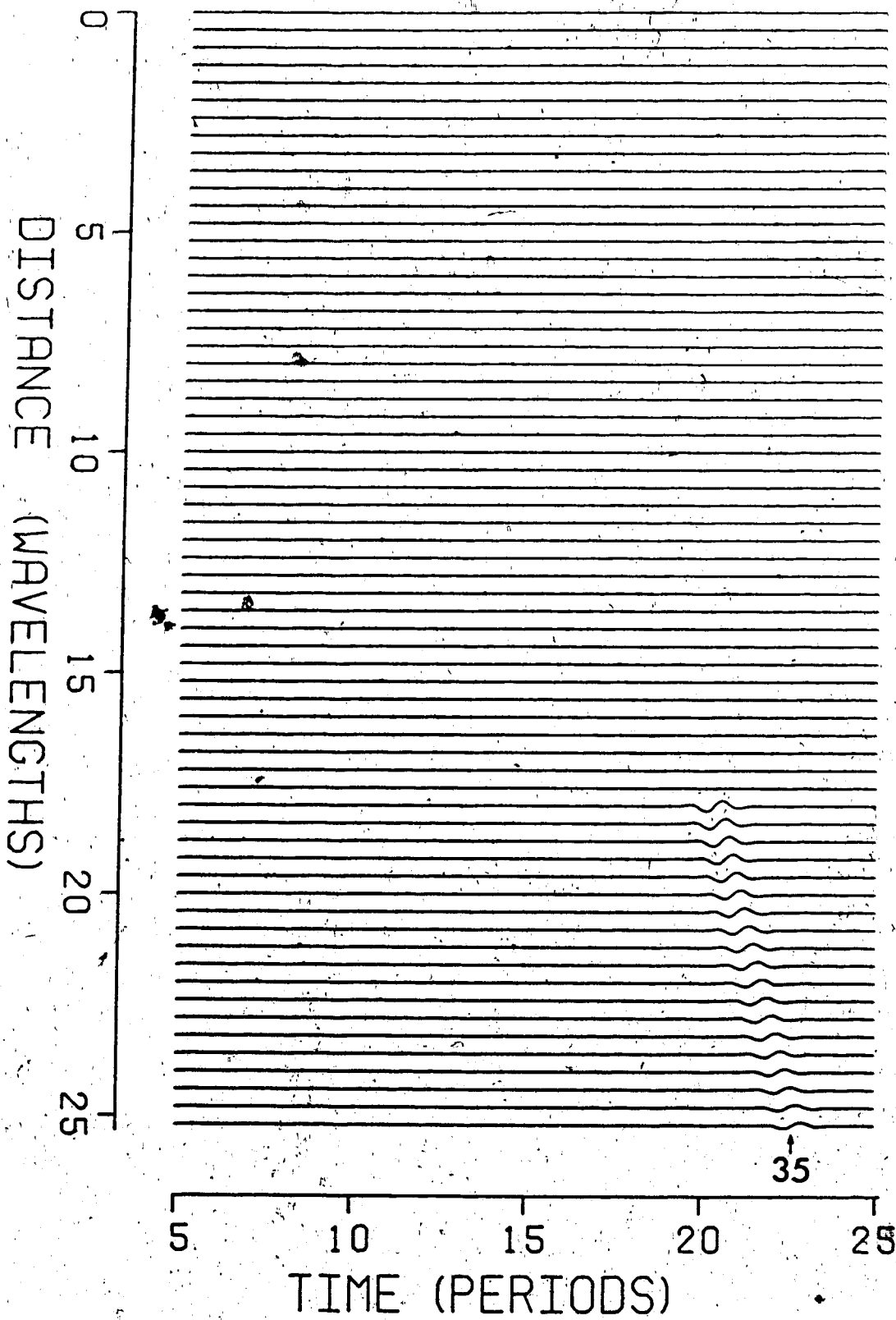Figure 68 Sum of contributions 33 and 34.

Figure 69 Synthetic seismograms for the second

part of diffracted rays in group VIII see

also Fig. 53d.

Note that the first reflection occurs in layer II,
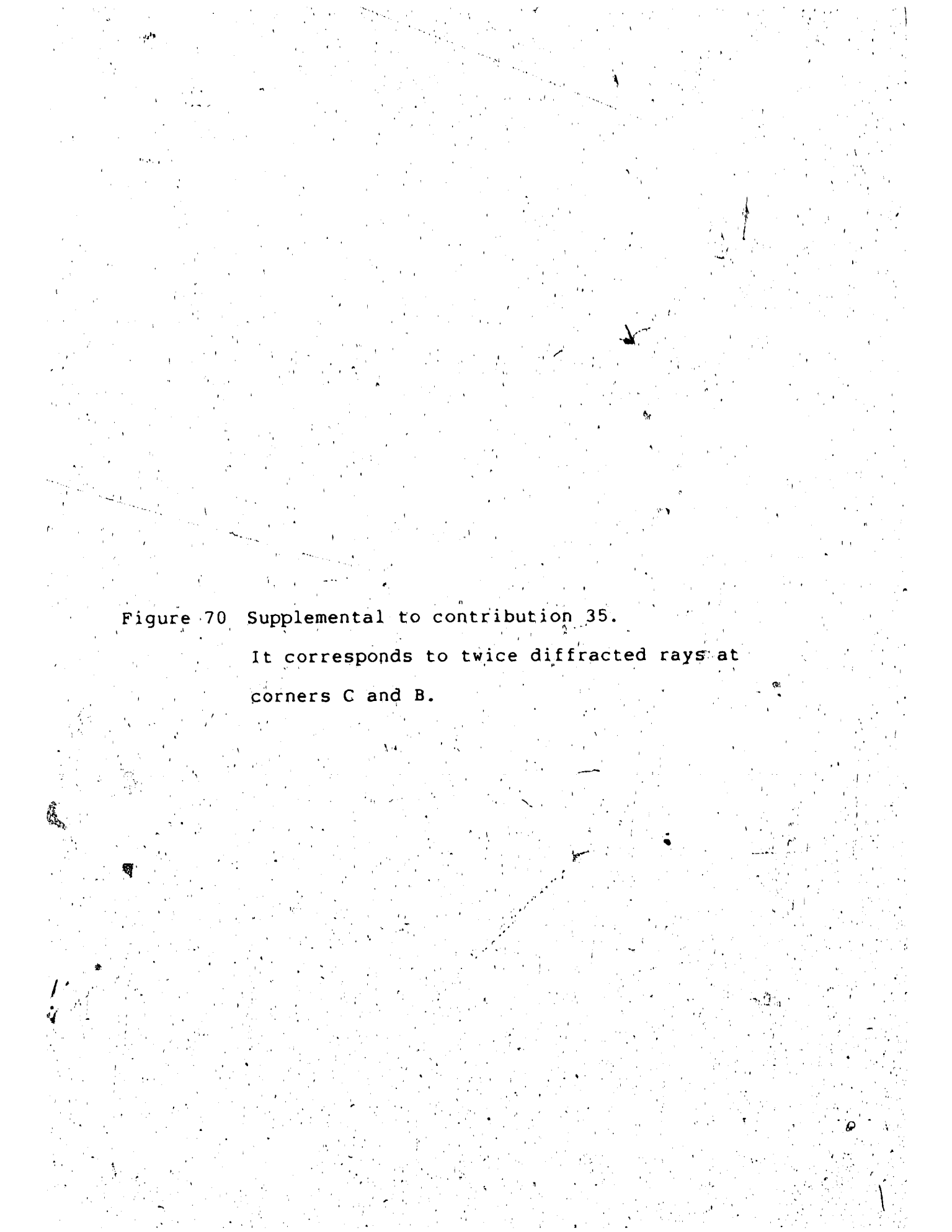
to the left of the side AC.

DISTANCE (WAVELENGTHS)

TIME (PERIODS)

35

Figure 70 Supplemental to contribution 35.

It corresponds to twice diffracted rays at

corners C and B.

DISTANCE (WAVELENGTHS)

TIME (PERIODS)

Figure 71 Sum of contributions 35 and 36.

DISTANCE (WAVELENGTHS)

TIME (PERIODS)
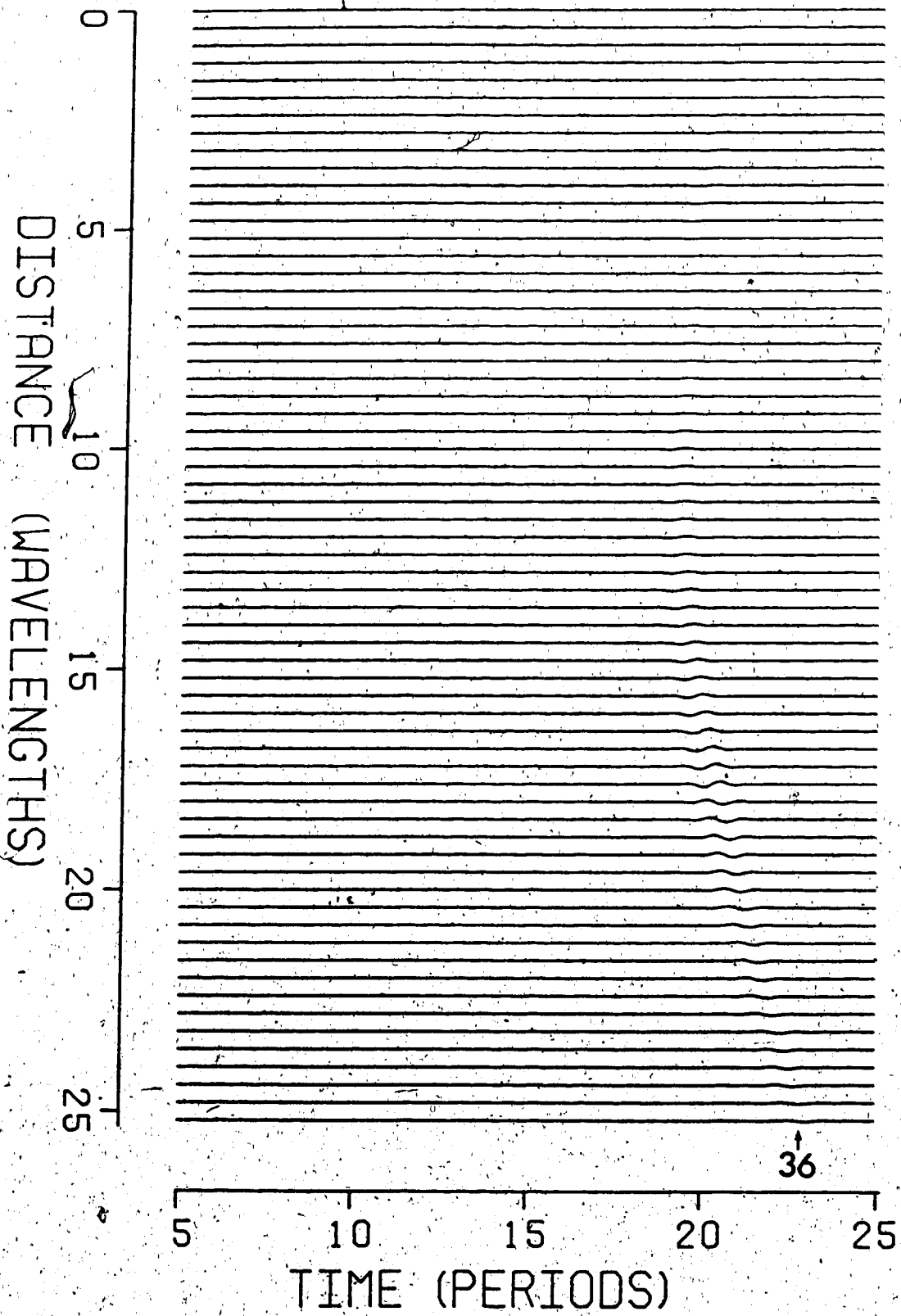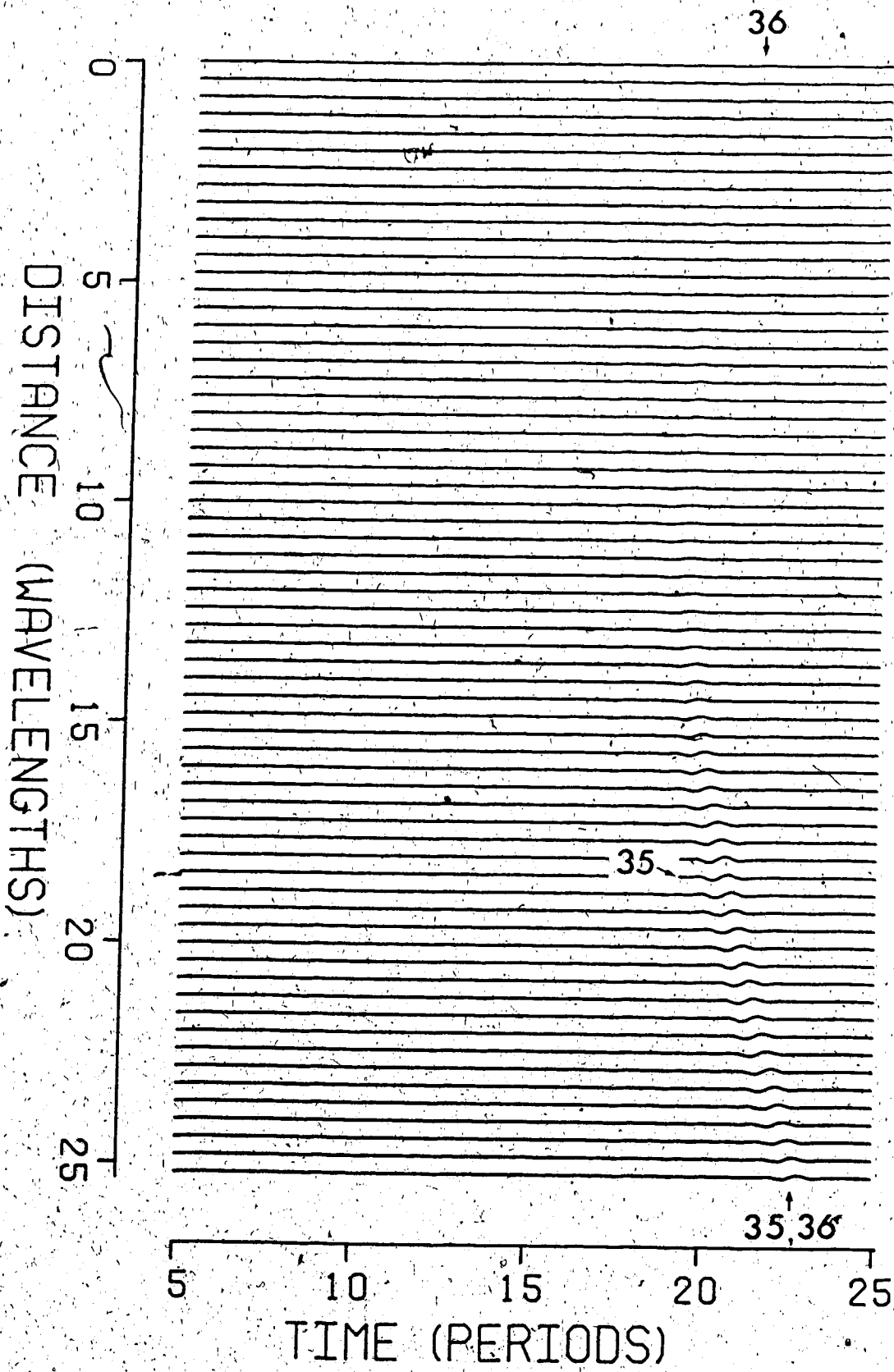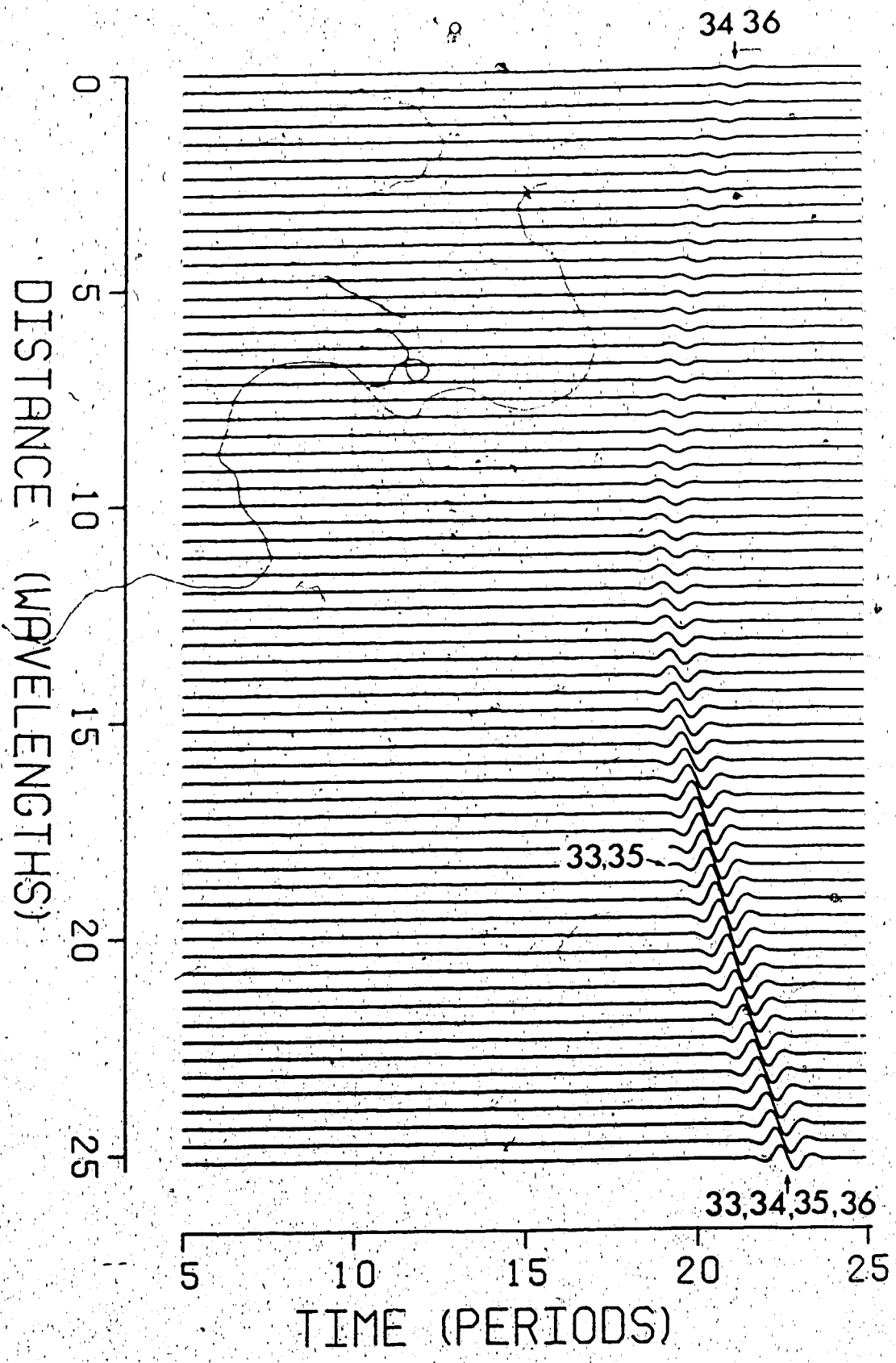
Figure 72 Sum of all contributions in group VIII.

of each group through geometric and diffracted ray diagrams,
the positions of the shadow boundaries and the radiation
characteristics of the elementary ray bundles. The
contributions are systematically summed up to give the total
field response of a particular group.

We will now proceed to build the final (approximate)
response by adding groups I through VIII sequentially. The
intermediate and final results are shown in Figs. 73-80.
These will be commented along with the help of the result by
the synthetic seismograms produced by the AMM in Fig. 11.
The process of this gradual build-up of our ray
representation of the seismic field is accompanied by a
short summary of each stage given below.

Fig. 18 of group I is shown here again as Fig. 73. The
shorter arrival time than any other subsequent groups means
that it will not be affected by later arrivals, except at
the tail end of event 3 near the point R'. The features of
polarity reversals and destructive interferences at
distances of 7.0 w and 16.0 w have already mentioned
previously.

Fig. 74 has group II added. The only interaction with
group I occurs at tail end of the receiver line. The
supplemental event 11, not contaminated by other arrivals

Figure 73 Group I contribution.

This is a repeat of Fig. 18.

Figure 74 Groups I and II contributions.

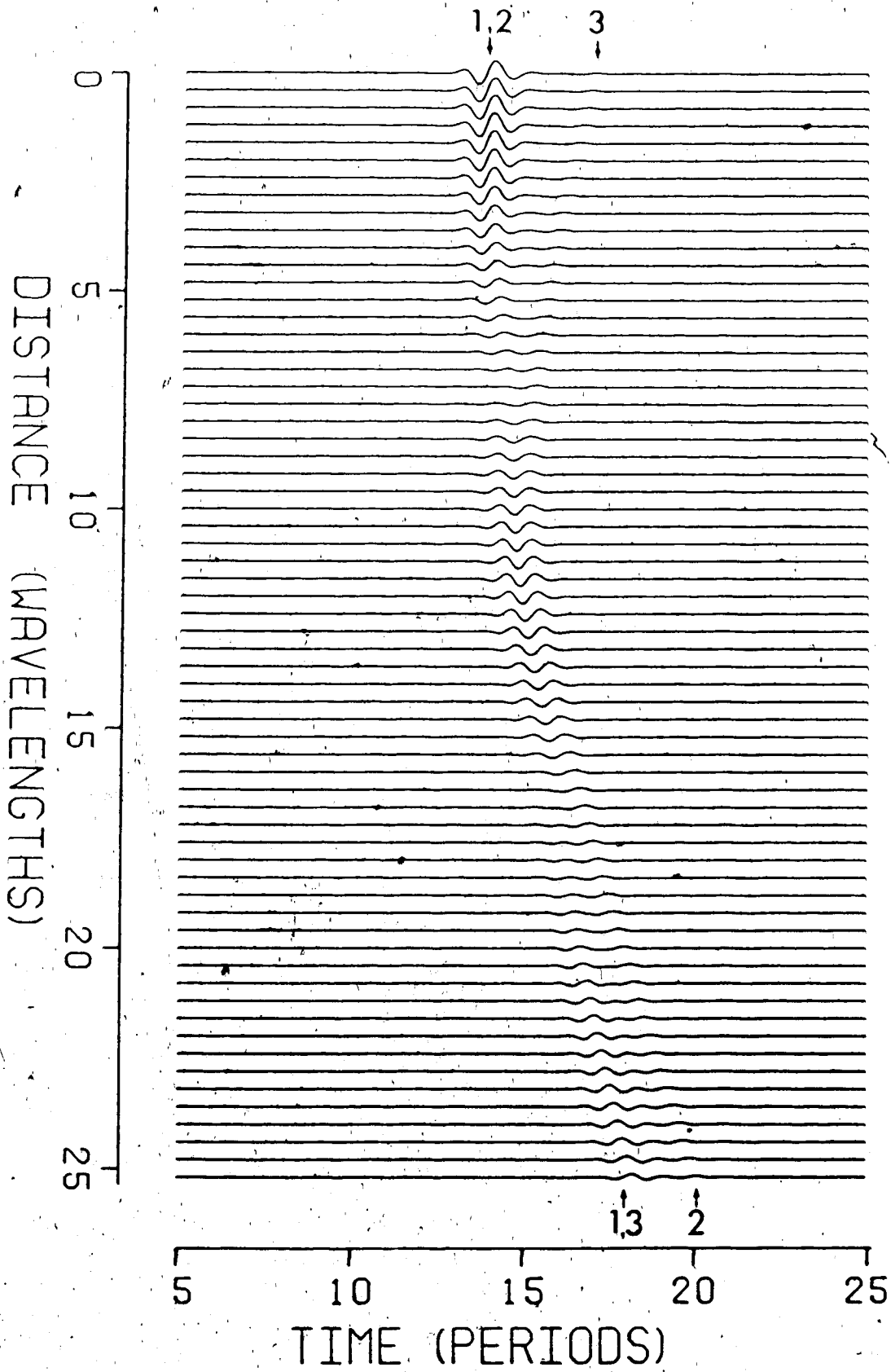Figure 75 Groups I through III contributions.

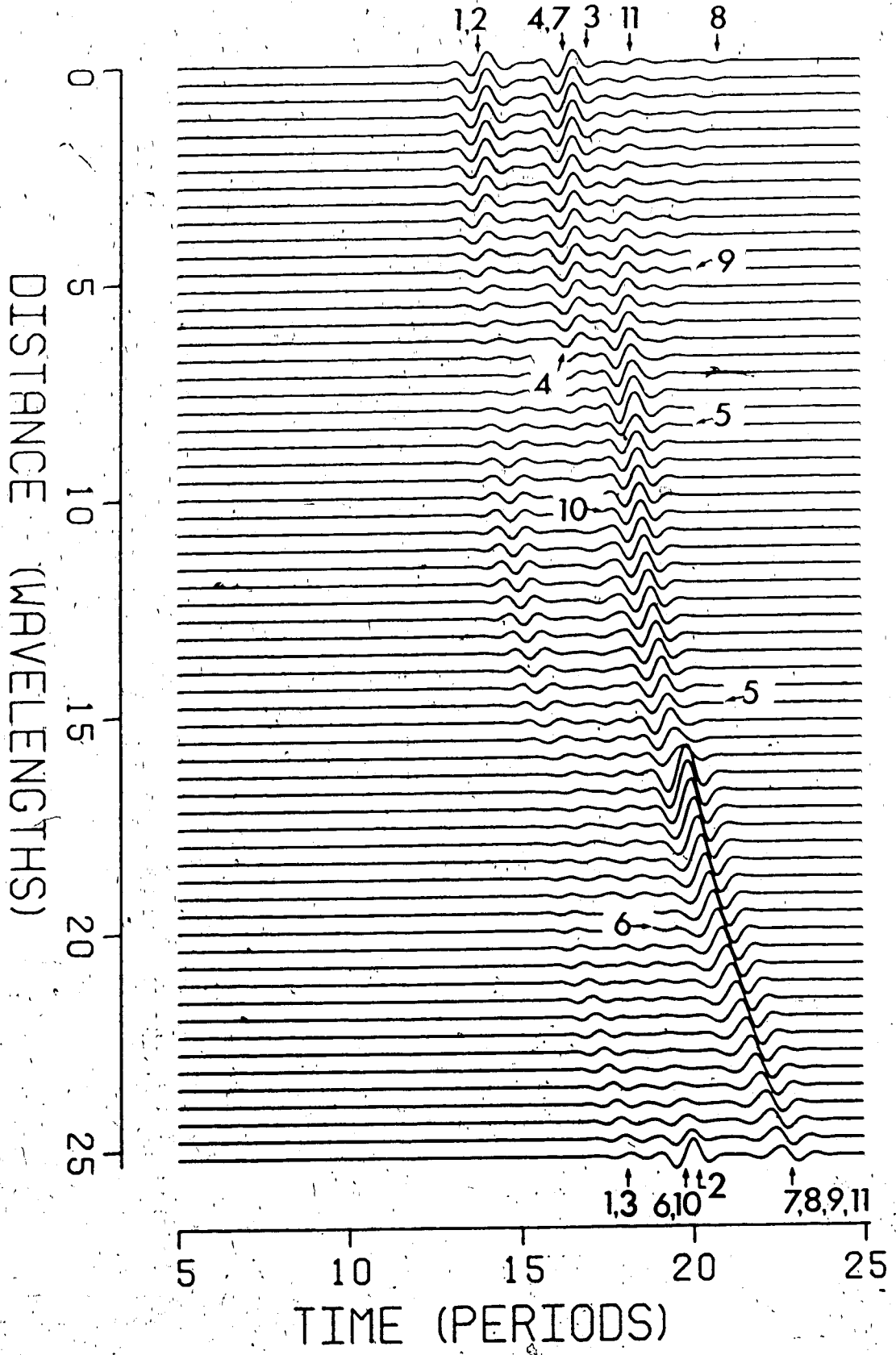Figure 76 Groups I through IV contributions.

Figure 77 Groups I through V contributions.

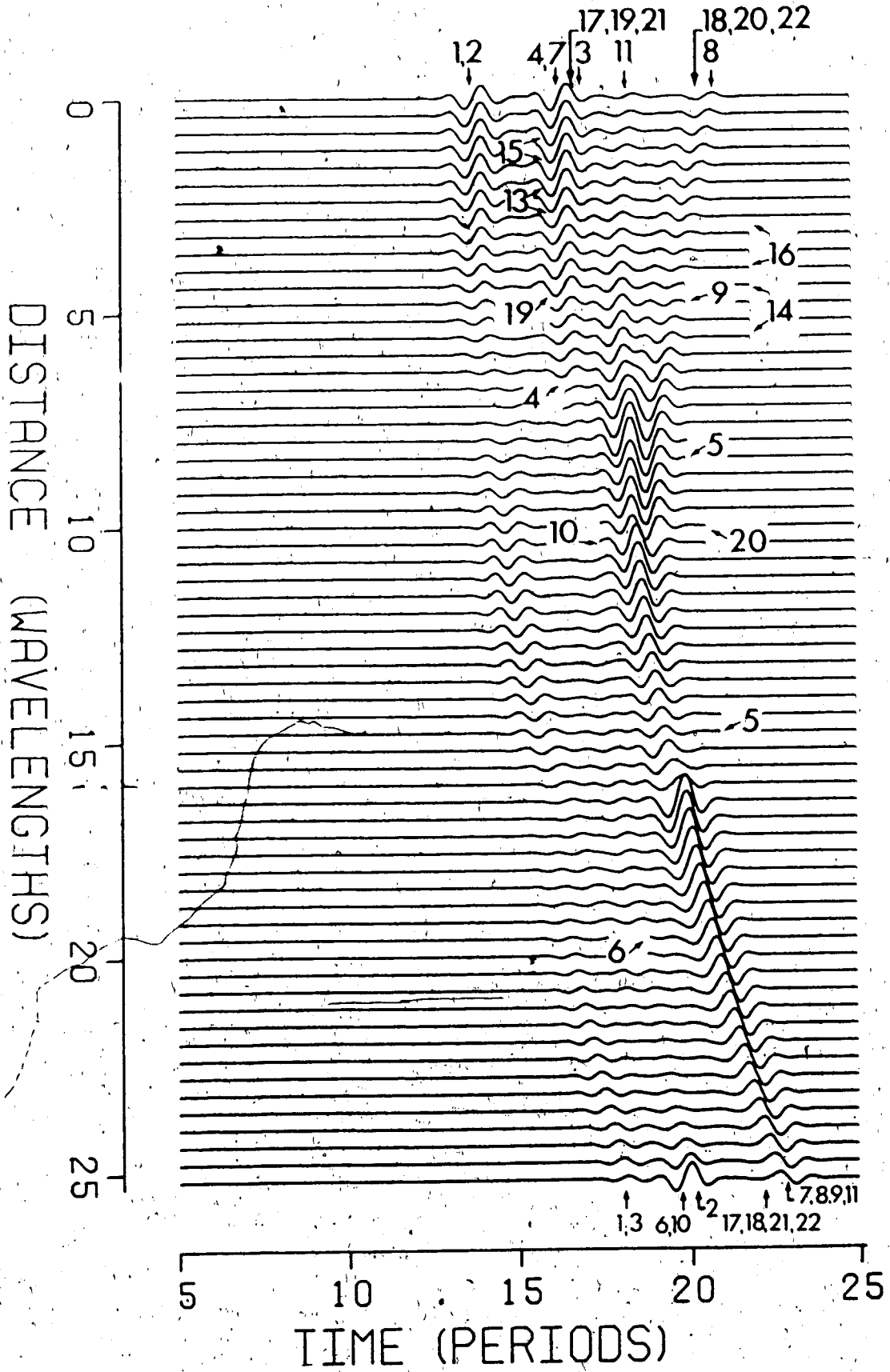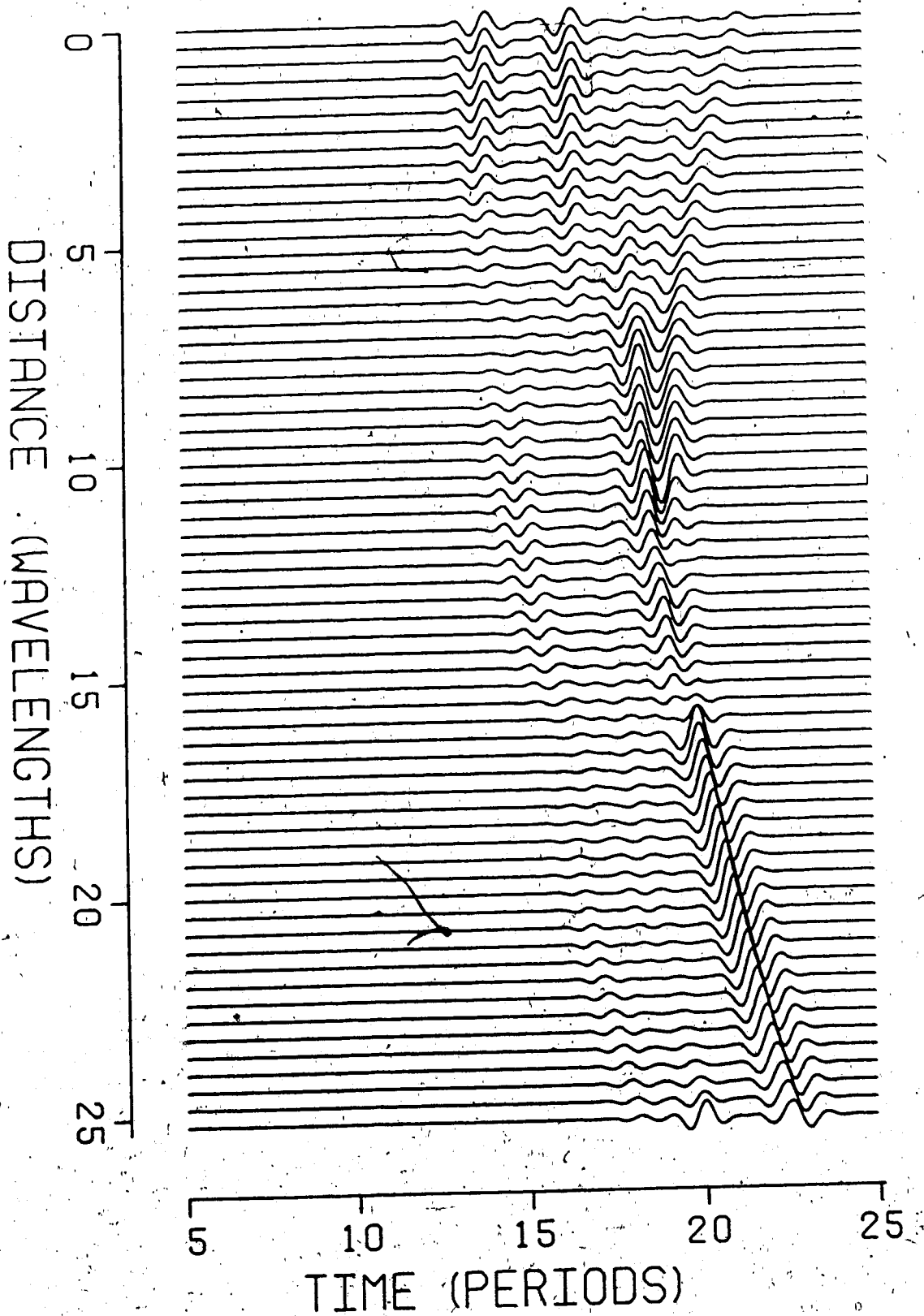Figure 78 Groups I through VI contributions.

Figure 79 Groups I through VII contributions.

Figure 80 Groups I through VIII contributions.

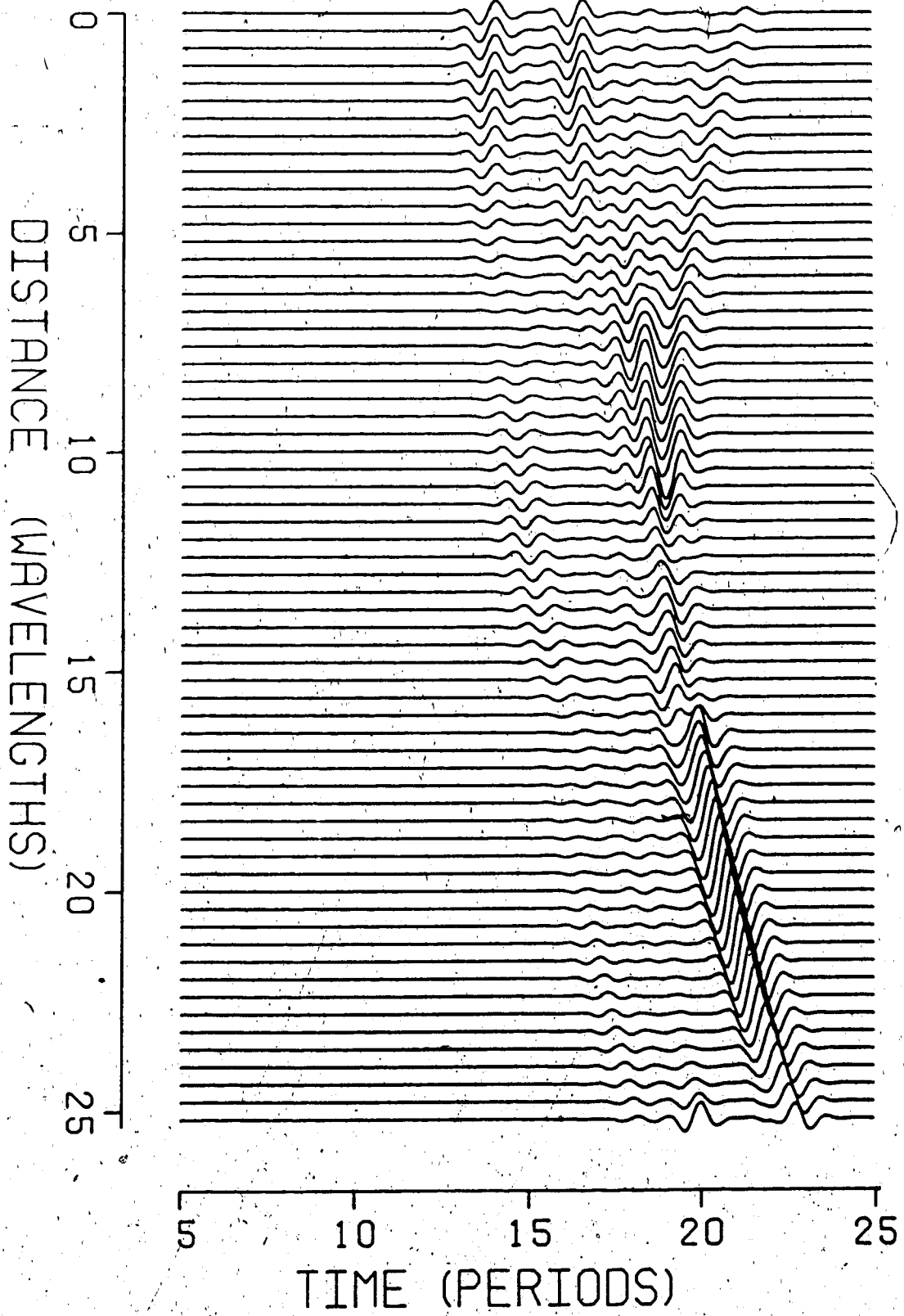DISTANCE (WAVELENGTHS)

TIME (PERIODS)

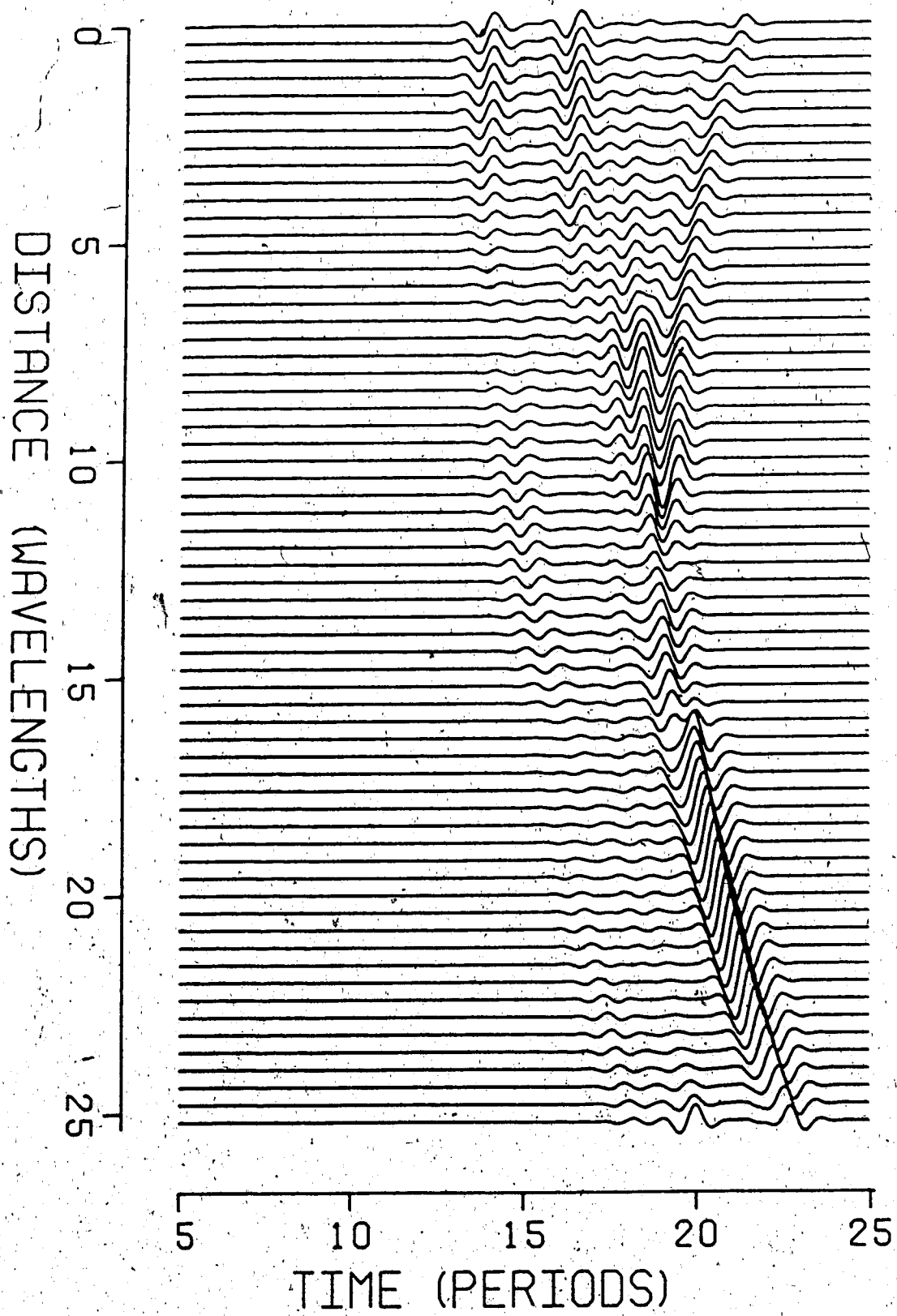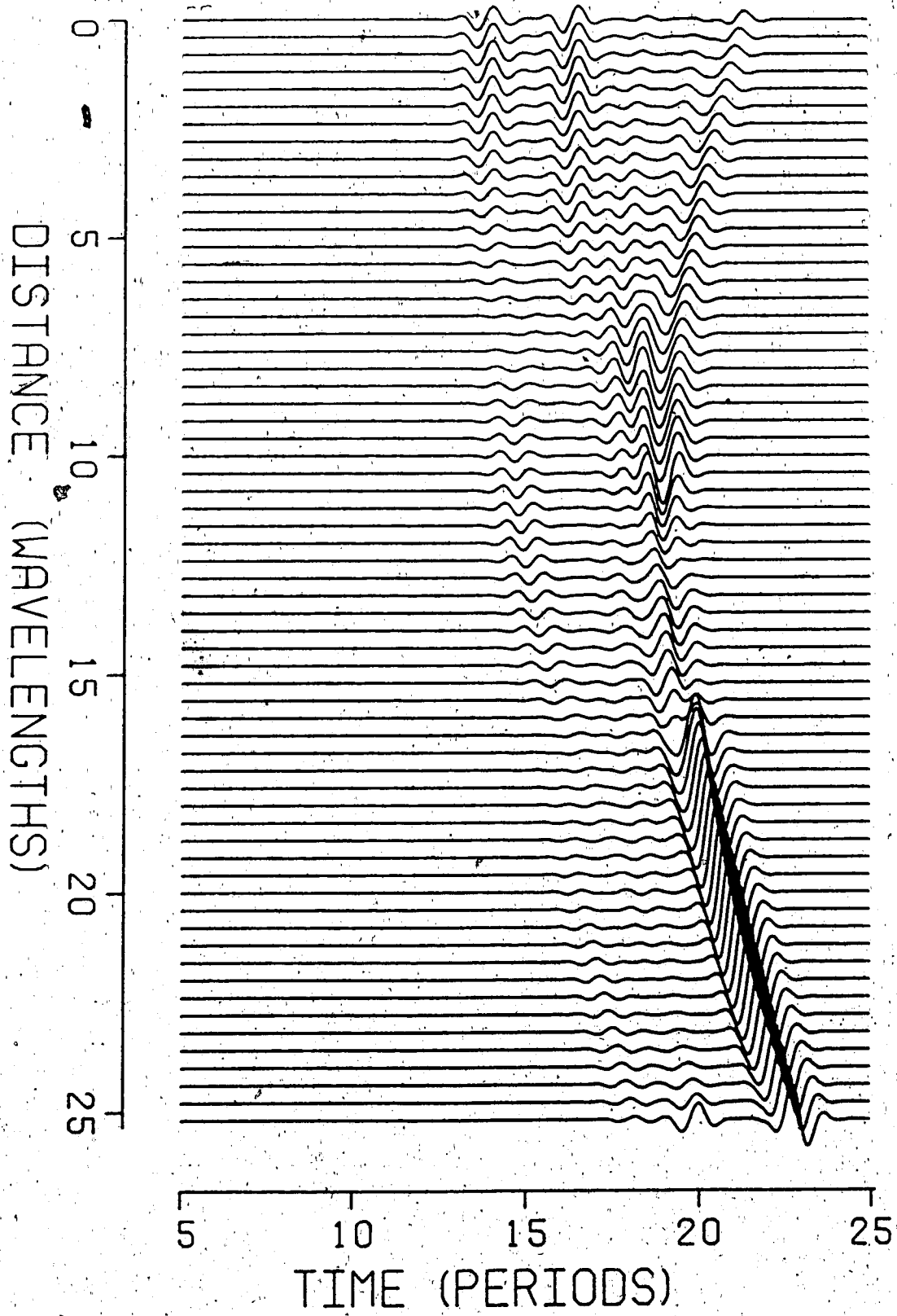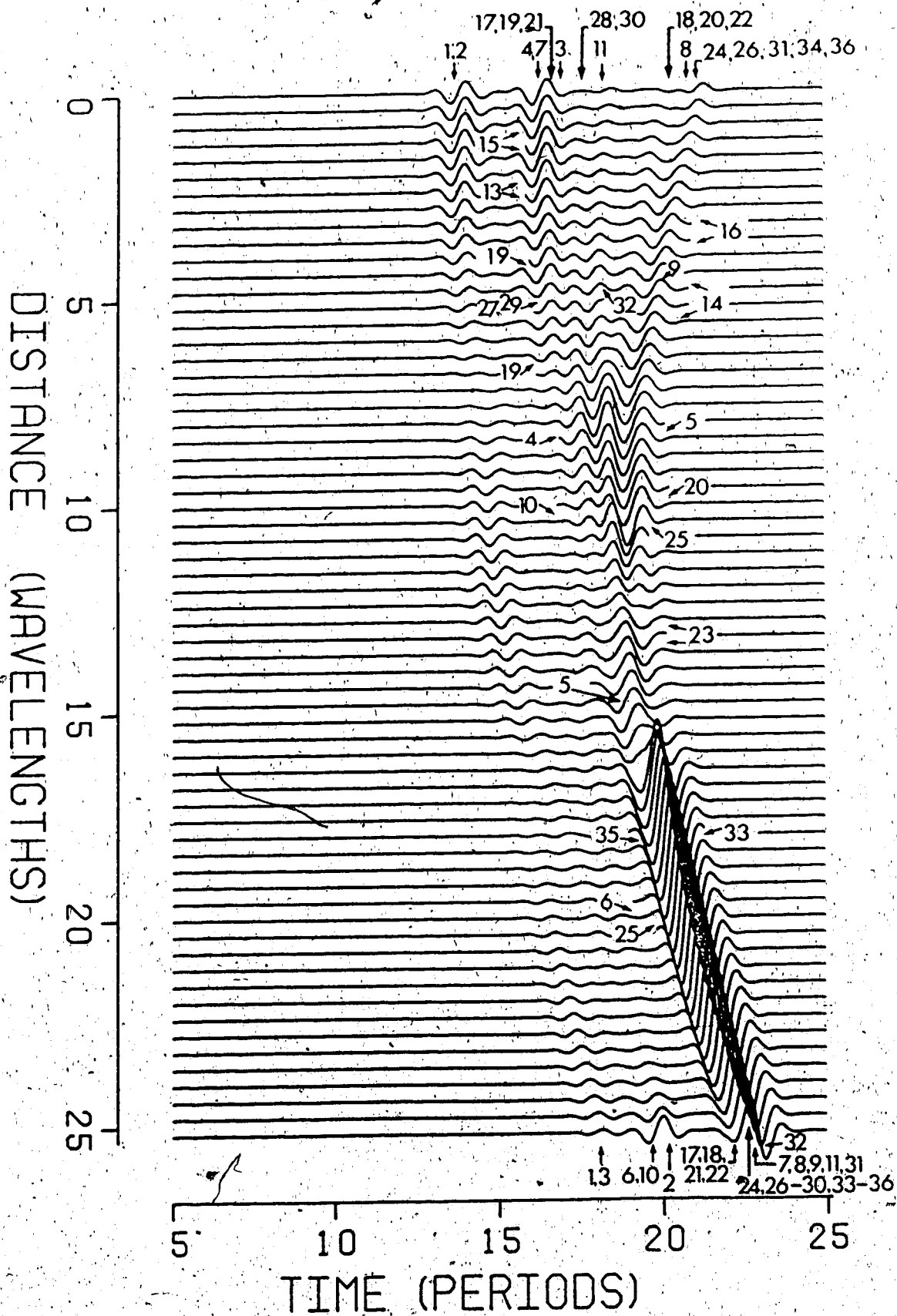DISTANCE (WAVELENGTHS)

TIME (PERIODS)

for receivers near 0.0 w turns out to be a significance ripple as observed also in Fig. 11. Subsequent diagrams will show that most other parts of group II signals will be interfered.

Fig. 75 shows the result of the addition of group III contributions to those in Fig. 74. Although there are still five more groups need be added, this diagram does serve as a reasonable approximation of Fig. 11. There is no particular reason, other than following the group numbers, in the order of addition for the subsequent groups. Quite often, many events have similar arrival times and thereby interfering together. So, it serves no purpose in investigating the intermediate result of addition from Fig. 76 to Fig. 79. We will instead concentrate on the final picture Fig. 80 and Fig. 11, and draw references from the individual group when needed.

To discuss Fig. 80, a different kind of grouping of events is warranted. Whereas the previous classification looks at the physical nature of the ray bundles, given by their ray diagrams, we are now more interested in dissecting each synthetic seismogram with respect to the arrival time. Thus, events 4 and 7 of group II mildly interact with events 17, 19 and 21 of group III. The effect is not at all significant. Events 24 and 26 of group IV interact with

group VI and events 34 and 36 of group VIII. Diffractions from corners A,B and C are involved, though all having a similar phase.

But, the biggest event occurs at time between 20 to 24 periods at recorders stationed between 15.0 w and 25.0 w. There are more than a dozen of events crowded within a small time window. The lesser components are events 7, 8 and 11 of group II, 24 of group IV, 29 of group V, 31 of group VI, and 34, 35 and 36 of group VIII. This still leaves us with events 9 of group II, 26 of group IV, 27 of group V, 32 of group VII and 33 of group VIII, with diffractions occurring at corners A and C. In particular, both events 27 and 33, (resulted in diffraction at corner C) carry a large amplitude, albiet are out of phase upon arrival at the receivers near the tail end. Similar interaction happened among the diffracted arrivals from corner A. The different move out patterns and phase variation works out to give stations around the distance of 20.0 w to have the highest amplitude.

In rectrospect, it would be interesting to show the geometrical arrivals (Fig. 81) by itself, and examine the changes brought about by the smoothing ability of the diffracted contribution.
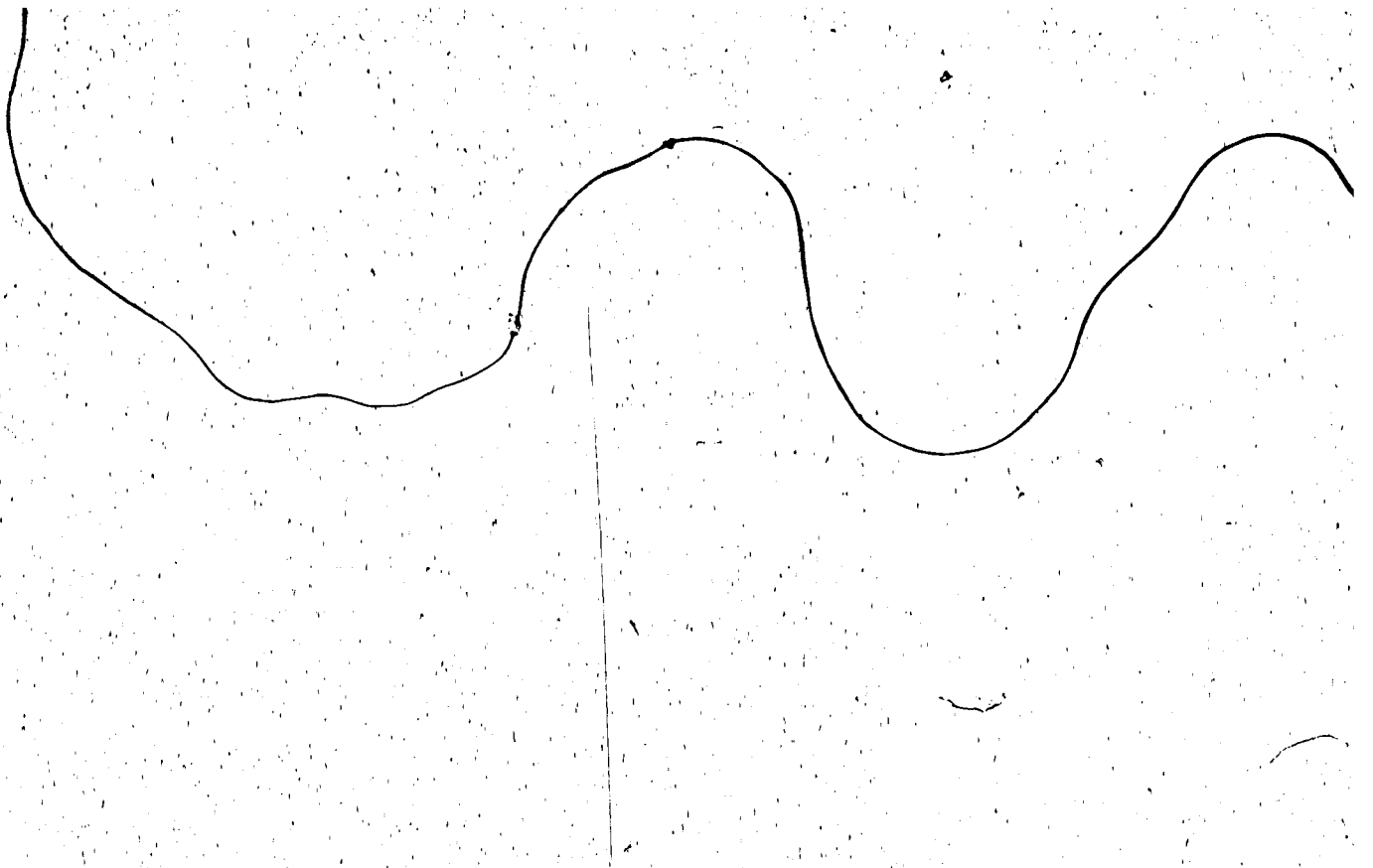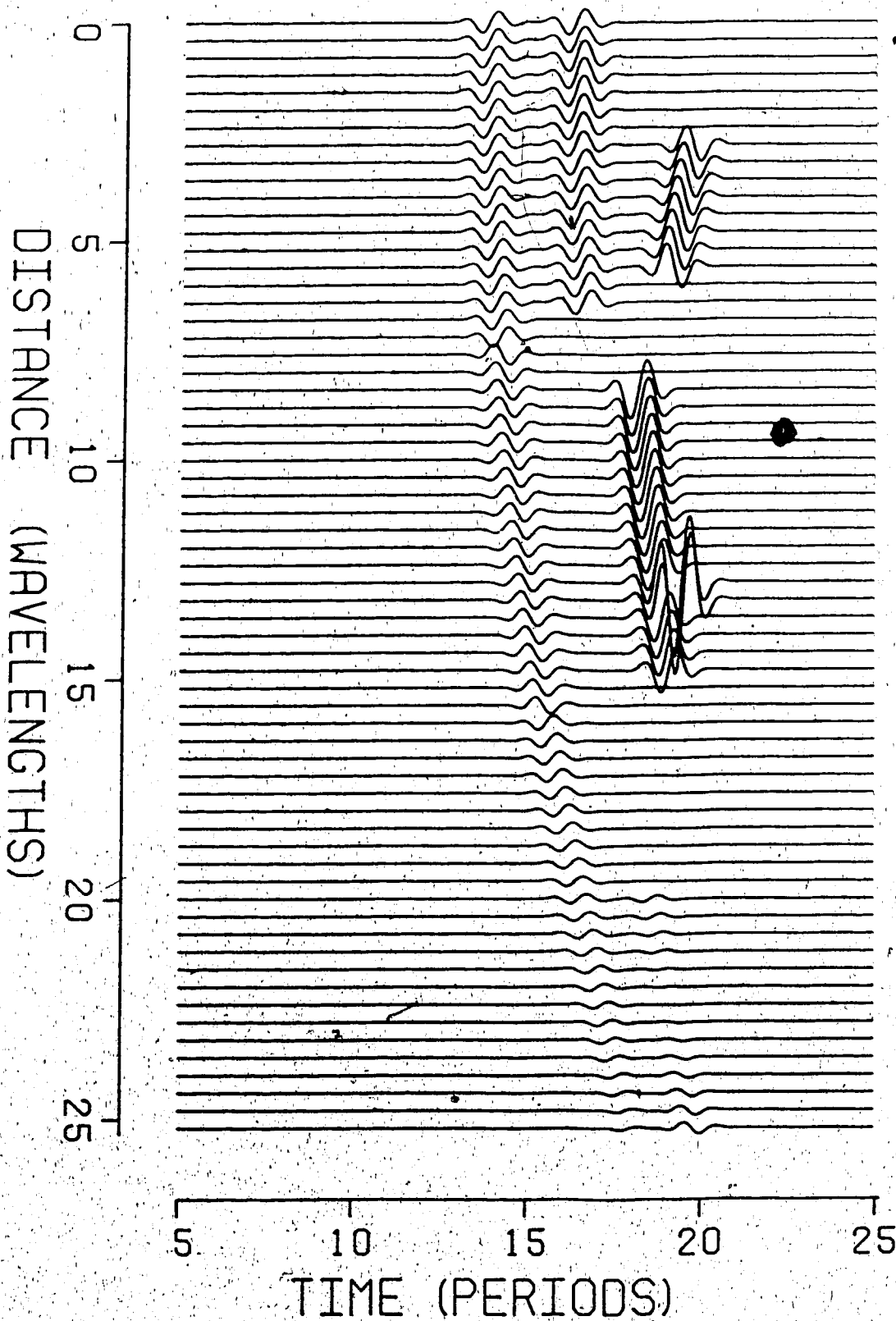
Figure 81 Synthetic seismograms for the
geometrical arrivals only.

GEOMETRICAL ARRIVALS ONLY

The above gives a sample of what may be used to aid interpreting a synthetic seismograms through model simulation. The Aleksecv-Mikhailenko method gives the result of a full solution, but is time consuming computation-wise. A second shortcoming is the difficulty in the separation of and identifying the origin of each individual event.

The present method, at the least, will serve well in the capacity of an inexpensive yet sufficiently accurate preliminary investigation. The simplicity in calculation also eliminates many a mistakes in setting up of the computation scheme, such as in the finite difference method used by the AMM. Fig. 82 shows a sketch of a simple valley model used by Mikhailenko (1984) for study of wave propagation in laterally inhomogeneous media. The SH response turned out to be out of phase by π when compared to result by the present method, see Fig. 83. The computational error has since been corrected.

As a final note, this method can be extended into the case for P-SV wave in laterally inhomogeneous media. Another feature is the freedom in placement of receivers. Hence, a promising application in VSP in depth migration methods.

Figure 82 The valley model

S -- source point.

Receiver number 1 is 2.5 unit from point R,

while adjacent receivers are 0.5 units apart.

The line ABCDEF outlines the boundary of

the 'valley'.

S

25.15

R r_1 r_8 r_9 R'

2.5

0.5

LINE OF RECEIVERS

5.85

9.0

A B E F

1.5

0 C D

11.5 8.5 2.5
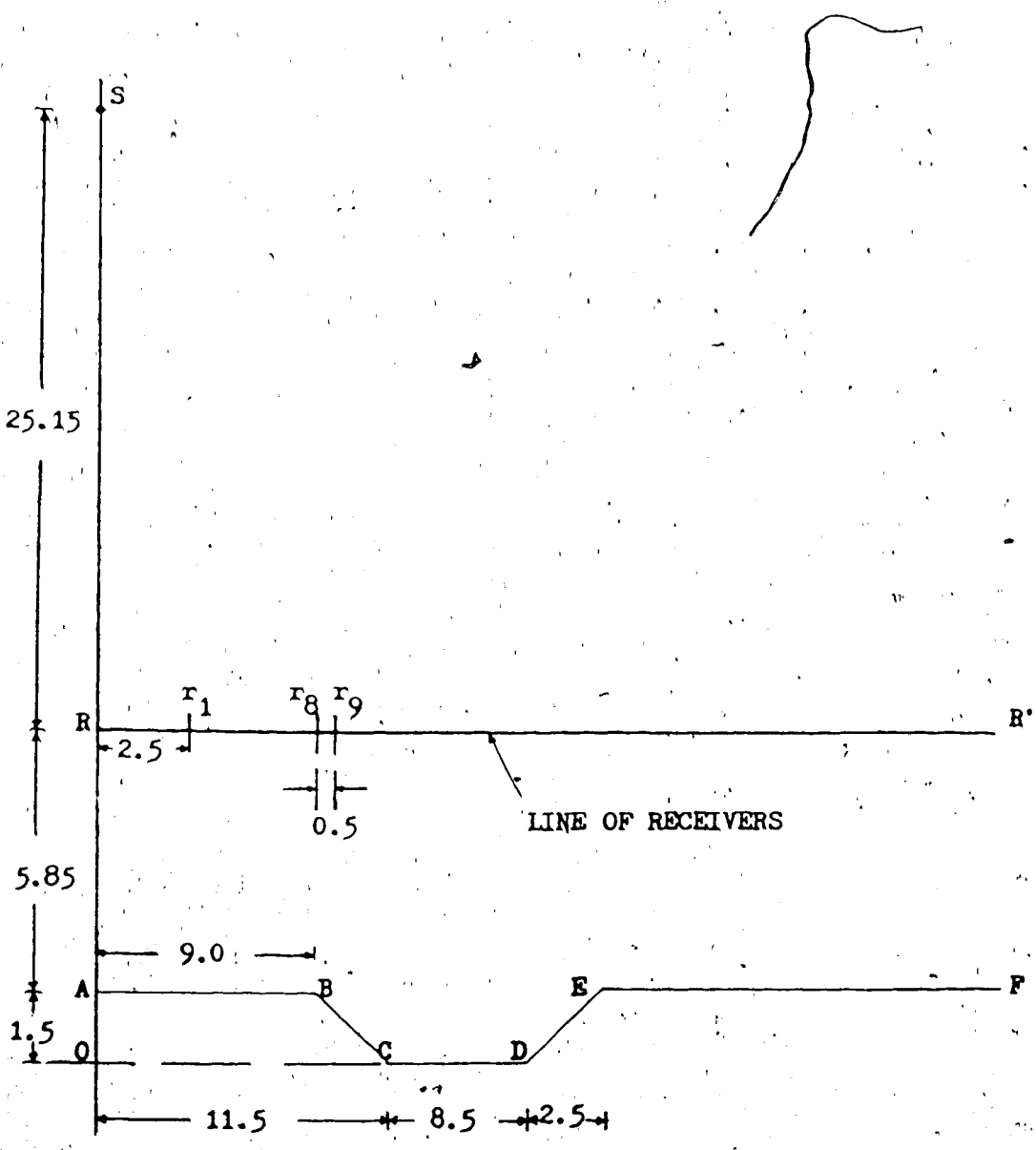
Figure 83 Synthetic seismograms for the

valley model. (SH mode)

S_1 - direct arrival

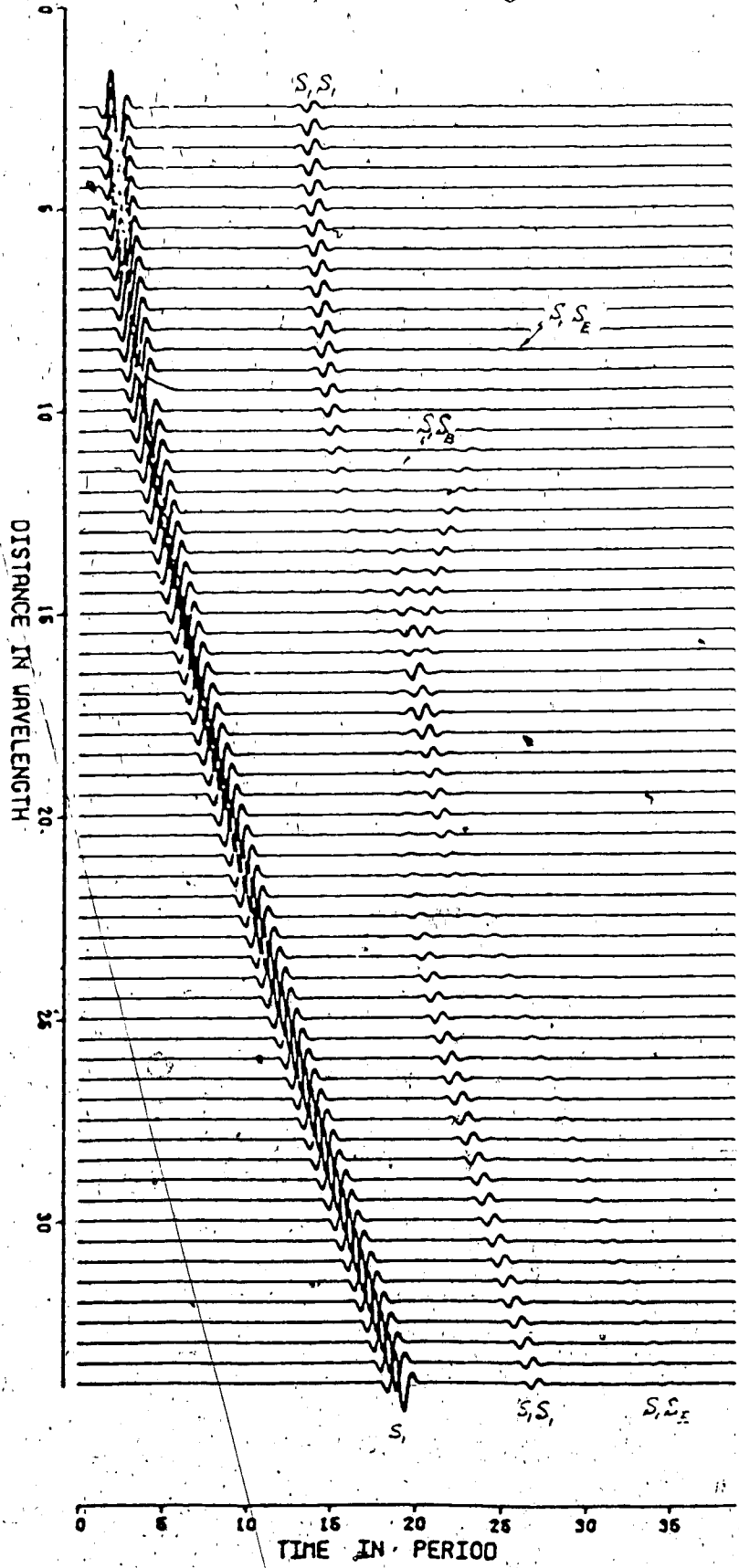S_1S_1 - first primary reflection

S_1S_B - diffraction from corner B

S_1S_E - diffraction from corner E

BIBLIOGRAPHY

Alekseev, A.S. and Mikhailenko, B.G., 1980. Solution of dynamic problems of elastic wave propagation in inhomogeneous media by a combination of partial separation of variables and finite difference method, J.Geophys., 48, 161-172.

Alford, R.M., Kelly, K.R., and Boore, D.M., 1974. Accuracy of finite-difference modelling of the acoustic wave equation, Geophysics 39, 834-842.

Born, M and Wolf, E., 1968. *Principles of Optics*, pergamon Press, Oxford.

Bowman, J.J. and Senior, T.B.A., 1969. The wedge, in *Electromagnetic and Acoustic Scattering by Simple Shapes*, Ch.6, J.J. Bowman, T.B.A. Senior, and P.L. Uslenghi, Editors, Wiley, New York.

Cerveny, V., Molotkov, I.A. and Psencik, I. 1977. *Ray Method in Seismology*, Charles University Press, Prague.

Cerveny, V. and Ravindra, R., 1971. *Theory of Seismic Head Waves*, University of Toronto Press.

Cerveny, V. and Psencik, I., 1972. Rays and travel time curves in inhomogeneous anisotropic media, Z. Geophysik 38, 565-577.

Claerbout, J.F., 1976. *Fundamentals of Geophysical Data Processing*, MaGraw-Hill, New York.

Fertig, J. and Muller, G., 1979. Approximate diffraction theory for transparent half-planes with application to seismic-wave diffraction at coal seams. J. Geophys., 46, 349-367.

Fock, V.A., 1965. *Electromagnetic Diffraction and Propagation Problems*, Pergamon Press, New York.

Forristal, G.Z. and Ingram, J.D., 1971. Elastodynamics
    of a wedge, Bull. Seism. Soc. Am. 61, 275-287.

Hilterman, F.J., 1982. Interpretative lessons from
    three-dimensional modelling, Geophysics, 47, 784-808.

Hudson, J.A., 1963. SH-waves in a wedge-shaped medium,
    Geophys. J. R. astr. Soc., 7, 517-546.

Hron, F. and Kanasewich, E.R., 1971. Synthetic seismogram
    for deep seismic sounding studies using asymptotic
    ray theory, Bull. Seism. Soc. Am., 61, 1169-1200.

Karal, F.C., Jr. and Keller, J.B., 1959. Elastic wave
    propagation in homogeneous and inhomogeneous media,
    J. Acoust. Soc. Am. 31, 694-705.

Kline, M., 1951. An asymptotic solution of Maxwell's
    equations, Commun. Pure Appl. Math. 4, 225-263.

Knopoff, L., 1969. Elastic wave propagation in a wedge,
    a Wave Propagation in Solids, J. Miklowitz, Editor,
    ASME Winter Annual Meeting, Los Angeles, California.

Lebedev, N.A., 1972. Special Functions and Their
    Application, Rev. English ed., translated and
    edited by R.A. Silverman, Dover Publication.

Markushevich, A.I., 1962. Complex Numbers and Conformal
    Mappings, translated by D.E. Brown, Engl. translation
    editor, I.N. Sneddon, Pergamon Press, Oxford.

Malyuzhinetz, G.D. 1958. Inverse transform for Sommerfeld
    integral, Doklady Academy of Science USSR, 118, No.6,
    1099-1102.

Mikhailenko, B.G., 1984. Synthetic seismograms for complex
    3-dimensional geometries using an analytical-numerical
    algorithm, Geophys. J. R. astr. Soc., 79:3, 963-986.

Pao, Y.H. and Ziegler, F., 1982. Transient SH-waves

in a wedge-shaped layer, Geophys. J. R. astr. Soc.,
71, 57-77.

Sommerfeld, A., 1896. Mathematische theorie der
diffraction, Math. Ann., S. 317.

Trorey, A.W., 1977. Diffraction for arbitrary source
receiver locations, Geophysics, 42, 1177-1182.

Zemell, S.H. 1975. Diffraction of elastic waves by a
rigid-smooth wedge, SIAM J. Appl. Math., 29, 582-596.

Ziegler, F. and Pao, Y.H., 1984. Transient elastic
waves in a wedge-shaped layer, Acta Mechanica, 52
133-163.

Appendix A

For a function $F(r)$, such that

(i) $|F(r)| < M\ |r|^{a-1}\ e^{b|r|}$

with M, a & b all greater than 1, and

(ii) $F(r)$ is analytic and regular in the whole region
of

$$0 < |r| < \infty,$$

then one may write

(A.1) $F(r) = \dfrac{1}{2\pi i} \displaystyle\int_{\Gamma_0} e^{i\kappa r \cos\alpha} f(\alpha)\ d\alpha$

where Γ_0 is shown in Fig. 2.

If $f(\alpha)$ is regular Γ_0 and satisfies

$$|f(\alpha)| < M_1\ e^{(1-a)|Im\alpha|},$$

then the inverse representation of $f(\alpha)$ in terms of $F(r)$ may
be found as follows.

Let $f(\alpha)$ be an odd function, then the integration of

$f(\alpha)$ along the two branches of Γ_0 may be reduced to along only one of the branches, say γ, in the following fashion

$$(A.2) \qquad F(r) = \frac{1}{\pi i} \int_{\gamma} e^{-i\kappa r \cos\alpha} f(\alpha) \, d\alpha$$

Now, let

$$(A.3) \qquad g(\omega) = - \frac{2if(\alpha)}{\sin\alpha},$$

where $\omega = -i\cos\alpha$, then

$$(A.4) \qquad f(\alpha)d\alpha = \frac{1}{2} i\sin\alpha \; g(\omega) \frac{d\omega}{i \sin\alpha}$$

$$= \frac{1}{2} g(\omega) \, d\omega,$$

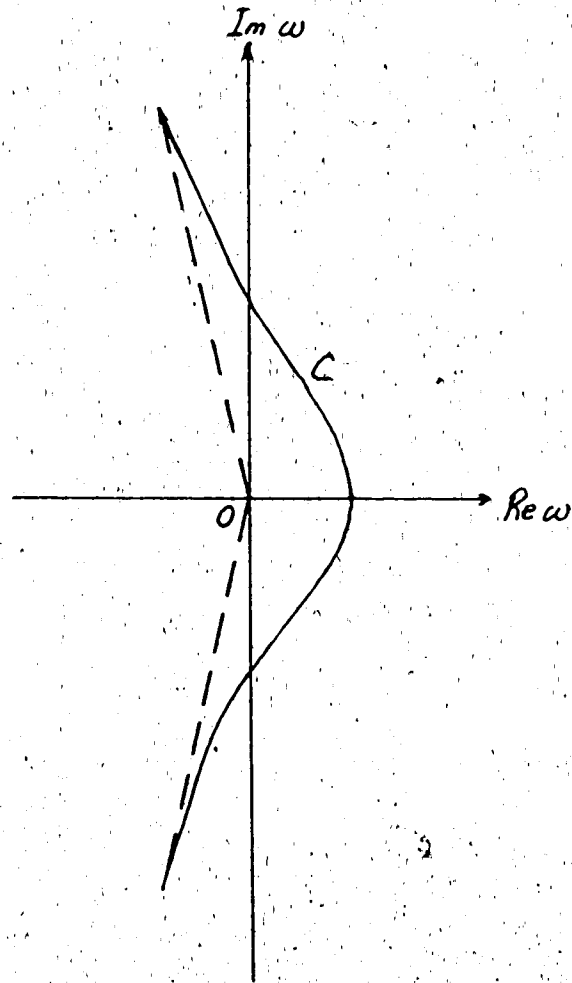and equation (A.2) becomes

$$(A.5) \qquad F(r) = \frac{1}{2\pi i} \int_{C} e^{\kappa r \omega} g(\omega) \, d\omega$$

where C is the contour of integration in the ω-plane as shown in Fig. A1 The interior of γ is mapped to the right hand side of C.

Now, consider the integral

$$(A.6) \qquad S = \int_{0}^{\infty} F(r) \, e^{-\kappa r \omega} \, dr.$$

Figure A1 Contour of integration C.

Substitution for $F(r)$ from (A.5) into (A.6) yields

$$(A.7) \qquad S = \int_0^\infty \{ \frac{1}{2\pi i} \int_C e^{\kappa r \omega_1} g(\omega_1) \, d\omega_1 \} e^{-\kappa r \omega} \, dr.$$

If $g(\omega)$ is regular, to the right of contour C, it enables us to change the order of integration and (A.7) becomes

$$(A.8) \qquad S = \frac{1}{2\pi i} \int_C g(\omega_1) \, d\omega_1 \{ \int_0^\infty e^{\kappa r (\omega_1 - \omega)} \, dr \}$$

$$= \frac{1}{2\pi i} \int_C g(\omega_1) \, d\omega_1 [\frac{1}{\kappa(\omega_1 - \omega)} e^{\kappa r (\omega_1 - \omega)}]_0^\infty$$

$$= - \frac{1}{2\pi i \kappa} \int_C [g(\omega_1)/(\omega_1 - \omega)] \, d\omega_1$$

$$= - \frac{1}{2\pi i \kappa} 2\pi i \text{ (residue at pole } \omega_1 = \omega)$$

$$= - \frac{1}{\kappa} [-g(\omega)]$$

$$(A.9) \qquad S = g(\omega)/\kappa.$$

The second minus sign in (A.8) arises from the fact that $g(\omega)$ is regular to the right of contour C and a close path has to be taken in the clockwise direction.

Now, substitute for $g(\omega)$ from (A.3) into (A.9), then

$$(A.10) \qquad S = \int_0^\infty F(r) e^{-\kappa r \omega} \, dr$$

$$= \frac{q\omega}{\kappa}$$

$$= -\frac{2if(\alpha)}{\kappa \sin\alpha}.$$

Or

(A.11) $f(\alpha) = \frac{i\kappa\sin\alpha}{2} \int_0^\infty F(r)\, e^{i\kappa r\cos\alpha}\, dr.$

Writing the original definition of $F(r)$ from (A.1) again

$$F(r) = \frac{1}{2\pi i} \int_{\Gamma_0} e^{i\kappa r\cos\alpha}\, f(\alpha)\, d\alpha,$$

we have our desired transform pair.

User: ROGE
Project no: PSGD

```
****  Obtained at      21:57:32    Mon Nov 03/86
****  Released at      21:59:06    Mon Nov 03/86
****  Lines printed    18-15
****  Images printed   154
****  Pages printed    77
```